Chapter 4

Seismic Signals and Noise

(Version June 2013. DOI: 10.2312/GFZ.NMSOP-2_ch4)

Peter Bormann[1)] and Erhard Wielandt[2)]

[1)] Formerly GFZ German Research Centre for Geosciences, Department 2: Physics of the Earth, Telegrafenberg, 14473 Potsdam, Germany; Now: E-mail: pb65@gmx.net

[2)] Formerly Institute of Geophysics, University of Stuttgart; Now: Cranachweg 14/1, D-73230 Kirchheim unter Teck, Germany; E-mail: e.wielandt@t-online.de

4.1 Introduction

4.1.1 About this chapter

Seismic signals are usually transient waveforms radiated from a localized natural or man-made seismic source. They can be used to locate the source, to analyze source processes, and to study the structure of the medium of propagation. In contrast, the term "seismic noise" designates undesired components of ground motion that do not fit in our conceptual model of the signal under investigation. What we identify and treat as seismic noise depends on the available data, on the aim of our study and on the method of analysis. Accordingly, data treated as noise in one context may be considered as useful signals in other applications. For example, short-period seismic noise can be used for microzonation studies in urban areas (see Chapter 14), and long-period noise for surface-wave tomography (Yanovskaya, 2012).

Seismic noise in a wider sense may comprise:

- Ambient vibrations due to natural sources (like ocean microseisms, wind, etc);
- Man-made vibrations (from industry, traffic, etc);
- Secondary signals resulting from wave propagation in an inhomogeneous medium (scattering);
- Effects of gravity (like Newtonian attraction of atmosphere, horizontal accelerations due to surface tilt);
- Signals resulting from the sensitivity of seismometers to ambient conditions (like temperature, air pressure, magnetic field, etc);
- Signals due to technical imperfections or deterioration of the sensor (corrosion, leakage currents, defective semiconductors, etc);
- Intrinsic self-noise of the seismograph (like Brownian noise, electronic and quantization noise);
- Artifacts from data processing.

The study of earthquakes or the imaging of the Earth with seismic wave arrivals requires their detection above background noise. Levels of natural ambient noise may vary by 60 dB (a factor of 1000 in amplitude) depending on location, season, time of day, and weather conditions (see Fig. 4.30). This corresponds to differences in detection thresholds for seismic arrivals by about three magnitude units. Therefore, prior investigation of noise levels at potential recording sites is of utmost importance.

In the following we will look into

- different mathematical representations of seismic noise and signals;
- origins of natural and man-made ambient seismic noise;
- basic features of signals and noise in the wide frequency range of interest, from local micro-earthquake to normal mode recordings (0.2 mHz < f < 100 Hz);
- influence of sensor-recorder-filter responses and of the installation environment on the appearance of signals and noise in seismic recordings;
- task-dependent procedures for SNR improvement of earthquake and explosion records;
- global detectability thresholds for short-period and long-period signals.

For an overview of such procedures with emphasis on seismic exploration we refer to Kumar and Ahmed (2011).

4.1.2 Nature and mathematical representation of signals and noise

As illustrated in Fig. 1.1, one of the key problems in seismology is to solve the inverse problem, i.e., to derive from the analysis of seismic records information on the structure and physical properties of the Earth through which the seismic waves propagate (see Chapter 2), as well as on the geometry, kinematics and dynamics of the seismic source process (see Chapter 3). The study of source processes is complicated by the fact that the seismic signals are weakened and distorted by geometric spreading and attenuation and due to reflection, diffraction, mode conversion and interference during their travel through the Earth. They are also distorted by the seismograph. While the Earth acts as a low-pass filter by attenuating higher frequencies most effectively, a mechanical seismograph is a second-order high-pass filter with a roll-off of –12 dB (a factor of 4) per octave for periods larger than its eigenperiod (see Chapter 5).

Additionally, seismograms contain noise and the desired signals are sometimes completely masked by it. Therefore, one of the main issues in applied seismology is to ensure a good signal-to-noise ratio (SNR) both by selecting recording sites with low ambient noise and by data processing. The success of the latter largely depends on our understanding of the ways in which seismic signals and noise differ. The basic mathematical tool for this purpose is the harmonic or Fourier analysis, that is, the decomposition of a signal into sinewaves. Depending on the type of signal (transient or stationary, continuous or sampled) different mathematical formulations must be used.

The Fourier integral transformation (section 4.2.1) can only be applied to transient signals (signals that disappear or decay after some time so that they have a finite energy). For other signals, the integral may diverge. The discrete transformation (section 4.2.2) requires a sampled signal of finite duration. Signals whose (mean) amplitude does not vary much within the

interval of time over which we typically analyze earthquake signals are mathematically treated as stationary signals, that is, signals whose statistical properties do not change with time. Such signals require a different mathematical treatment. Of course, this is a mathematical idealization whose appropriateness depends on the time scale. Over longer intervals of time, almost all signals will change their statistical properties. For example, marine microseisms can normally be treated as stationary within the time frame of a seismogram but often change their amplitude and predominant period within a few days according to meteorological conditions over the oceans.

A Fourier transformation in the strict sense does not exist for stationary signals. This is not a practical problem because we can Fourier analyze such signals over finite time intervals of any desired length. A practically more important difference is that we are normally not interested in the detailed waveform of such signals because we want to remove them from the record, not to interpret them. (There are, however, interesting exceptions as mentioned in the introduction.) In most cases we only want to know how strong they are in different parts of the frequency spectrum. This information is contained in a quantity named ***Power Spectral Density*** that is explained in section 4.2.3.

Transient signals such as earthquake seismograms may have a complicated waveform, but this waveform is determined by the earthquake source, the structure of the Earth, and the properties of the seismograph. The amplitudes and phases of the harmonic components of the signal are not random numbers but follow certain mathematical relationships. They are, in principle, smooth functions of frequency, often smoother and simpler than the signal appears in time domain. For example, the waveform of a train of surface waves is essentially determined by a much simpler dispersion curve. Such waveforms or spectra are sometimes called deterministic, in contrast to the "stochastic" or "random" waveform of seismic noise. Strictly speaking, however, seismic noise is also deterministic. The difference is that we don't know its sources and propagation paths well enough to predict or interpret the waveform, don't want to care about them, and therefore assume that the spectral amplitudes and phases are random numbers. Again, this is a mathematical simplification that may or may not be appropriate.

4.2 Different mathematical formulations of spectral analysis

4.2.1 Fourier transformation of continuous transient signals

The signal radiated from a seismic source, be it an explosion or a shear rupture, is usually a more or less complicated displacement step function or velocity impulse of finite duration from milliseconds up to a few minutes at the most (see Chapter 2, Fig. 2.5 and Chapter 3, Figs. 3.4 and 3.9). According to the ***Fourier theorem*** any arbitrary ***transient function*** $f(t)$ in the *time domain* can be represented by an equivalent function $\boldsymbol{F(\omega)}$ in the ***frequency domain***. The mathematical relationship between the two domains is defined by the ***Fourier integral transformation***:

$$f(t) = (2\pi)^{-1} \int_{-\infty}^{\infty} F(\omega) \exp(i\omega t)\, d\omega \tag{4.1}$$

(4.2) $$F(\omega) = \left|F(\omega)\right| \exp(i\phi(\omega)) = \int_{-\infty}^{\infty} f(t) \exp(-i\omega t) dt$$

Other sign conventions may be used, e.g. exp(-$i\omega$ t) in Eq. (4.1) and exp($i\omega$ t) in Eq. (4.2) in wave propagation studies in order to assure that the wave-number vector is positive in the direction of wave propagation. The normalization factor $(2\pi)^{-1}$ may be applied in the backward or in the forward transformation, or its square root in both. $f(t)$ needs not be a continuous function in a mathematical sense but it must be defined at every instant of time, with the possible exception of isolated points where a step may occur.

$F(\omega)$ is the ***complex Fourier transform*** of the continuous signal $f(t)$, usually written as a function of the angular frequency ω which is 2π times the common frequency (the number of cycles per second). The absolute value of the Fourier transform, $|F(\omega)|$, is called the ***amplitude spectrum***, and its phase $\phi(\omega)$ the ***phase spectrum***. Fig. 4.1 gives an example. The phase may practically be measured in radians, cycles (2π radians), or degrees, although only radians are used in mathematical formulas. Since the integral in Eq. (4.1) is equivalent to a sum, the Fourier transformation implies that an arbitrary transient signal, even an impulsive one, can be represented as a sum of time-harmonic functions (sinewaves). Fig. 4.2 illustrates how a sum of harmonic terms can equal an arbitrary function.

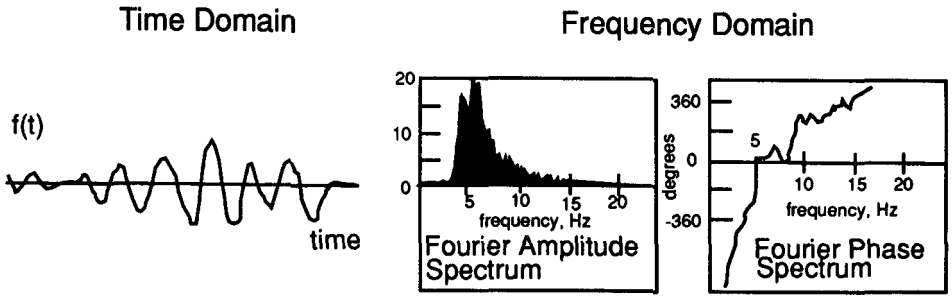

Fig. 4.1 A signal recorded as a function of time (left) can be represented equivalently in the frequency domain by its complex Fourier spectrum. The amplitude (middle) and phase spectrum (right) are both needed to calculate the complete time series (reproduced from Lay and Wallace, 1995, Figure 5.B1.1, p. 176; with permission of Elsevier Science, USA).

The concept of frequency filtering (for example, high-, low- or band-pass filtration) has its roots in analog signal processing and is therefore intimately connected to the Fourier Integral Transformation while practical procedures on a computer do not use integrals and are often only approximations to the corresponding analog procedures. Frequency filtering reduces the amplitudes of harmonic components of a signal in part of the frequency spectrum, usually in order to suppress noise. Examples will be given in paragraph 4.7.1 below. Filtering may also modify the phases. It will, in general, change the amplitude of the desired signal in time domain. Therefore, magnitudes of seismic events determined from amplitude and period readings of seismic phases are comparable only when determined from analog seismic records with identical standard frequency responses or digital records filtered accordingly (see IASPEI standards for magnitude measurement in IS 3.3). Systematic differences between various magnitude scales as well as saturation effects are the consequence of filtering the input signals with different responses in

different and often band-limited frequency ranges (see Chapter 3, Tab. 3.1 and Figs. 3.5, 3.20 and 3.47).

4.2.2 Fourier transformation of sampled signals

A mathematically simpler and more computer-adequate formulation of the harmonic analysis is the *Discrete Fourier Transformation*:

$$a_k = \frac{1}{M} \sum_{l=-M/2}^{M/2-1} c_l e^{2\pi jkl/M} \tag{4.3}$$

$$c_l = \sum_{k=0}^{M-1} a_k e^{-2\pi jkl/M} \tag{4.4}$$

where a_k is a *time series* (a series of equidistant samples of a continuous signal $f(t)$) and c_l are complex *Fourier coefficients*, each of which can again be decomposed into an amplitude and a phase factor. The index l represents the frequency. To obtain the frequency in physical units we replace k/M in the exponent by $k\Delta t/M\Delta t$ where Δt is the sampling interval. Then $k\Delta t$ is the time of sample a_k and $l/M\Delta t$ is the frequency of the phase factor after c_l. $T = M\Delta t$ is the length of the signal in time. Both series, a_k and c_l, are periodic outside their original interval of definition. So other conventions with respect to the index ranges of the summation are possible; all sums over M consecutive samples are equivalent. Supplementary information on different aspects of the Fourier transformation is found in Chapter 5, section 5.2.3 ff.

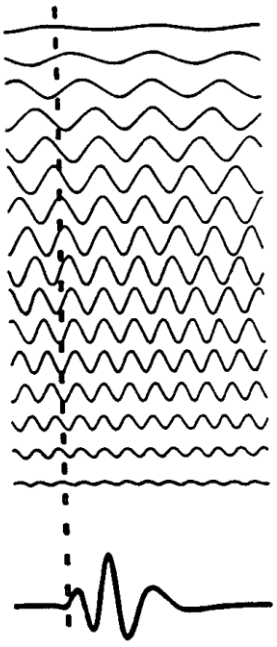

Fig. 4.2 The transient signal is formed by summing up the harmonic terms of Eq. (4.3), a discretized version of Eq.(4.1). The amplitudes of each harmonic term vary, being prescribed by the amplitude spectrum $|c_l|$. The shift of the phase of each harmonic term is given by the phase spectrum (reproduced from Lay and Wallace, 1995, Figure 5.B1.2, p. 177; with permission of Elsevier Science, USA).

4.2.3 Spectral analysis of stationary signals (noise)

As we have already said above, in the analysis of stationary noise we are normally not interested in the exact waveform or other details that do not convey useful information. In most cases, we only want to know "how strong" the noise is, or whether it will prevent us from detecting a specific earthquake signal. Since with frequency filters we may be able to sup-

press noise in one part of the spectrum and still preserve signals in another part, it is necessary to consider the spectral distribution rather than the total strength of both signals. There lies, however, a mathematical difficulty in this seemingly simple task: the formal measures of "strength" for transient and stationary signals are incompatible and cannot easily be compared. Mathematically speaking, transient signals have a finite energy and zero power (in the average over all times) while stationary signals have an infinite energy but a finite power. The same holds for the spectral densities. For a quantification of stationary noise, the concept of ***Power Spectral Density (PSD)*** is therefore appropriate while transient signals are more adequately described by their ***Energy Spectral Density (ESD).*** The relationship between the two densities is trivial; we must however go into some mathematical detail to explain how they are calculated and used. In some situations (such as for the comparison of earthquake signals with instrumental clip levels) neither the PSD nor the ESD are suitable measures, and we must use other criteria which will be the subject of section 4.4.

Generally, the spectral density $P(\omega)$ of some quantity Q is a function of frequency whose integral over a given frequency band (such as the passband of a specific seismograph) gives the total amount of Q in that band. When Q is the power of a signal, the physical dimension of P is power per bandwidth (per Hertz). However, not every quantity that has the physical dimension X per Hertz is a spectral density. For example, the Fourier transform $F(\omega)$ in eq. (4.2) has the dimension μm per Hz when the seismic signal $f(t)$ is measured in μm, but its absolute value $|F(\omega)|$ is not an "amplitude spectral density" even if this name has been used by some authors (including Aki and Richards in their well-known textbook, 1980). Integrating $|F(\omega)|$ over a bandwidth does, in general, NOT yield the amplitude of $f(t)$ in that bandwidth, as demonstrated in Fig. 4.6.

4.2.3.1 Energy and power densities of continuous signals

We can now explain how the Spectral Densities of Energy and Power are actually determined for a given signal. Mathematically we must distinguish between transient and stationary signals, and between continuous and sampled signals. Practically, of course, we always analyze signals of finite length that are, mathematically speaking, transient, and for digital processing the signals must be sampled. Still, most concepts behind data processing (such as using a sinewave to represent a single frequency) come from the realm of continuous signals, and we must therefore start from the Fourier Integral Transformation even if it is not a practical tool for digital processing.

The Fourier Integral Transformation as formulated in Eqs. (4.1) and (4.2) has the mathematical property (known as Rayleigh's or Parseval's theorem)

$$\int_{-\infty}^{\infty} f(t)^2\,dt = \int_{-\infty}^{\infty} \frac{|F(\omega)|^2}{2\pi}\,d\omega = \int_{-\infty}^{\infty} |F(2\pi\nu)|^2\,d\nu \tag{4.5}$$

On the left side, we have what in data processing is called the total energy of signal $\boldsymbol{f(t)}$ (this is not a physical energy but proportional to it). We have assumed that the energy is finite even if the signal may mathematically have an infinite length (for example, it may decay exponentially). The right side then represents the energy as an integral of $\boldsymbol{E = |F(2\pi\nu)|^2}$ over all fre-

quencies ν. Thus, according to the above definition, the integrand E is the Energy Spectral Density of the signal.

Note that negative frequencies must be included in the integration. For real signals, the ESD is a symmetric function, $E(-2\pi\nu) = E(2\pi\nu)$, so we can as well double it and integrate only over positive angular frequencies. This convention is normally used in engineering and other practical applications; the ESD is then given as twice the "mathematical" value. The same applies to the PSD in the next paragraph. It is important to clarify which convention is being used.

Power is energy per time. Normally we are not interested in the instantaneous power but in the average power over at least one cycle of the signal (if it is approximately periodic). The concept of power is mainly applied to stationary signals such as sinewaves or seismic noise whose average power is constant or varies slowly. A Fourier transform in a strict sense is not defined for such signals, but we can Fourier analyze the signal over any finite time interval of length T. When both sides of Eq. (4.5) are divided by T, the left side represents the average power, and $P = E/T = F(2\pi\nu)|^2/T$ on the right side is the Power Spectral Density for that interval.

4.2.3.2 Energy and power densities of sampled signals

We now consider a signal represented by M samples taken at equidistant intervals $\Delta t = T/M$ where T is the total duration of the signal. The power W of such a signal is defined as the average square of the samples:

$$W = M^{-1}\sum a_k^2 \tag{4.6}$$

Again, this is not a physical power, but the latter is proportional to W. The square root of W is the *effective* or *root-mean-square (rms) amplitude* a_{rms} of the signal. Now it is a property of the discrete Fourier transformation Eqs. (4.3) and (4.4) that

$$\sum a_k^2 = M^{-1}\sum |c_l|^2 \tag{4.7}$$

Like in the case of Eq. (4.5), the total power $W = M^{-1}\sum a_k^2 = M^{-2}\sum |c_l|^2$ is now expressed as a sum of contributions from different frequencies. Only discrete frequencies l/T are used in the transformation, but if we go back to the domain of continuous signals and consider the Fourier coefficients c_l as samples of a continuous function, then each coefficient stands for a frequency interval of width $1/T$ (this is sometimes called a "frequency bin"). The ratio of power over bandwidth at frequency l/T is therefore

$$P_l = M^{-2}\,T|c_l|^2 = M^{-1}\Delta t|c_l|^2 \tag{4.8}$$

The series P_l is the discrete equivalent of the PSD function. It offers a practical way to compute the PSD for stationary signals. For a graphical representation, the P_l series is often smoothed and

decimated because the original coefficients are normally positive random numbers. The suitably smoothed PSD approaches, at each frequency, a definite limit for $M \to \infty$ when the signal is stationary (this is essentially the definition of stationarity). For (supposedly) stationary signals like seismic background noise, calculating the PSD of a long but finite section is the only possible form of a spectral analysis. The PSD is not equivalent to a Fourier transform; the signal cannot be reconstructed from it with an inverse transformation because the phase information is lost. For finite sections of a stationary signal we can of course use the discrete Fourier transformation if we later need a backward transformation. The smoothed and decimated PSD is however normally more useful because it contains all essential information in a concentrated form, and eliminates arbitrary normalization factors. The discrete equivalent of the Energy Spectral Density is obtained as $E_l = T \cdot P_l$.

4.2.3.3 Obtaining the ESD or PSD by spectral analysis of the autocorrelation

An alternative way of determining the spectral density of energy or power is to calculate the Fourier transformation of its autocorrelation. An autocorrelation can be defined for stationary signals that have no Fourier transform; the signal is then essentially defined via its autocorrelation, and needs not be explicitly known. The autocorrelation of a stationary signal $f(t)$ is the expectation value of the product $f(t)\,f(t+\tau)$, often written as $\langle f(t)\,f(t+\tau)\rangle$. It is a function of the delay (or time lag) τ and normally decays rapidly for large time lags. So one can truncate it without committing a large error and then Fourier transform it. The method can as well be applied to finite sections of a signal. The properly normalized Fourier transform is the PSD of the signal. For details, see Havskov and Alguacil, 2002. Truncating the autocorrelation also has the desirable effect of smoothing the PSD. Nevertheless the method is now obsolete as a practical tool; it dates back to the time when the Fast Fourier Transformation was not available, and relatively short truncated series were more convenient to transform.

4.2.3.4 Testing PSD and ESD computation

Although the PSD and ESD of a given signal are in principle independent of the method of computation and of the normalization of the Fourier transform, there often remains an uncertainty whether a given formula or computer program delivers properly normalized values. The question is easy to settle. All that must be done is to analyze an arbitrary signal, calculate its power or energy in time domain, and check if the integral of the PSD or ESD over all (or over positive) frequencies reproduces it.

4.2.3.5 Changing between displacement, velocity, and acceleration

By differentiating under the integral in 4.1, we see that the time-derivative $\dot{f}(t)$ of a signal $f(t)$ has the Fourier transform $j\omega F(\omega)$. So if the signal was originally measured as a displacement and we need the Fourier transform of the velocity, we obtain it by multiplying the original Fourier transform by $j\omega = j \cdot 2\pi\nu$ where ν is the common frequency. The Fourier transform of the acceleration is $-\omega^2 F(\omega)$. We can of course also go back from acceleration or velocity to displacement by dividing by the appropriate factor. The ESD and PSD are positive quadratic functions of the Fourier amplitudes, so differentiating the signal brings a factor ω^2, integration a factor ω^{-2}, etc. A PSD of velocity can thus easily be converted into that of displacement or acceleration. It has become a standard to measure seismic noise as a PSD of acceleration, that is,

in $(m/s^2)^2$ per Hz or m^2s^{-3}. We note again that "power" in this context is not the physical power in watts but simply the mean square amplitude of ground acceleration.

4.2.3.6 Representing PSDs in decibels

As in acoustics, the power ratio $r = (a_2/a_1)^2$ between two signals of amplitude a_1 and a_2 is often expressed in Decibels (dB). This is a logarithmic measure that expresses a ratio as a difference of logarithms. The difference in dB is $10 \log_{10}[(a_2/a_1)^2] = 20 \log_{10}[(a_2/a_1)]$. When expressing the power spectral density P_a of acceleration relative to the metric unit 1 $(m/s^2)^2$/Hz, we get

$$\mathbf{P_a}\,[\mathrm{dB}] = 10 \log_{10} [P_a / 1\ (m/s^2)^2/\mathrm{Hz}] \tag{4.9}$$

For the rest of this paragraph, we must caution the reader that **numerical values of physically incommensurable quantities will be compared**. Equations (4.10) and (4.11) and the following two text lines do not imply that the decibel units on both sides of the equal sign mean the same. They only look the same because the incommensurable reference levels were omitted. The decibel scale in Fig. 4.3 is likewise questionable; the figure should in principle have three decibel scales with different legends.

By substituting the period T = 1/f (in s) for the frequency f in (4.6) and (4.7) , we get:

$$\mathbf{P_v}[\mathrm{dB}] = \mathbf{P_a}[\mathrm{dB}] + 20 \log (T/2\pi) \tag{4.10}$$

and

$$\mathbf{P_d}[\mathrm{dB}] = \mathbf{P_a}[\mathrm{dB}] + 40 \log_{10} (T/2\pi) = \mathbf{P_v}[\mathrm{dB}] + 20 \log (T/2\pi) \tag{4.11}$$

Consequently, for the period $T = 2\pi = 6.28$ s $\mathbf{P_a = P_v = P_d}$ (only the numbers are equal!) Also, $(\mathbf{P_d - P_a}) = 2 \times (\mathbf{P_v - P_a})$ = constant for any given period, negative for $T < 2\pi$ s and positive for $T > 2\pi$ s (Fig. 4.3).

4.2.4 Cross-correlation and coherence

The ***cross-correlation*** of two stationary signals $f(t)$ and $g(t)$ at the time lag τ is defined as the expectation value (practically, mean value) of the product $f(t)\, g(t+\tau)$. Properly normalized, it is a measure of the similarity between the two signals and is called their ***coherence*** (consult a textbook on data processing for details). Like the Power Spectral Density, it can be calculated via the Fourier transformation and specified as a function of frequency, in which case the name ***coherence spectrum*** is more adequate (but not always used). Each signal is fully coherent with itself (the coherence equals 1); independent random signals are incoherent (their coherence equals zero) although strictly this is only true in the limit of an infinite duration and after removing the mean. More interesting is the case that signals are partially coherent. One can then conclude that with some (frequency-dependent) fraction of the power, a common signal is hidden in them, for example a seismic signal masked by instrumental noise of the sensors.

Seismic signals depend not only on time but also on the location where they are recorded. It is therefore meaningful to ask whether the signal recorded at one location is coherent with the same

signal recorded at another location. This aspect of coherence is usually expressed as a "coherence length" over which the recorded signals have a specified coherence. The coherence length is only a fraction of a wavelength for omnidirectional noise (noise propagating in all directions) but can be much longer when noise originates in a limited source area and propagates essentially in one direction (Fig. 4.22). In a plane wave, the coherence length is theoretically infinite.

4.2.5 The uncertainty principle of the Fourier Transformation

The time signal $f(t)$ and its Fourier transform $F(\omega)$ according to eq. (4.2) are related to each other through many rules that can be found in the textbooks (a few textbooks are named at the beginning of section 5.2). One such relationship, the uncertainty principle, is important for the following discussions. It states that an impulsive signal (one whose energy is concentrated in a short interval of time) must have a large bandwidth; a signal with a small bandwidth cannot be concentrated in time, or have a sharp onset. For any signal, the product of its width (uncertainty, variance) in time and its bandwidth (in terms of angular frequency) cannot be smaller than ½. Only a Gaussian pulse (one with the envelope $\exp(-\alpha t^2)$) gives the minimum value. Many figures in this chapter, starting from Fig. 4.6, are illustrations of the uncertainty principle. In quantum mechanics, the same mathematical relationship has the consequence that the position and momentum of a particle cannot be known at the same time; if the particle is sharply localized, then its momentum is uncertain and vice versa.

4.3 A first look at seismic and instrumental noise

4.3.1 Global models for the PSD of seismic noise

Fig. 4.3 is a summary of noise levels observed in a worldwide network of seismic stations (Peterson 1993). The graph shows the upper and lower envelopes (solid lines) of a large collection of curves representing the PSD of ground acceleration. The "engineering" convention is used, that is, the PSD has to be integrated over positive frequencies only. The envelopes are commonly referred to as the New High Noise Model (NHNM) and New Low Noise Model (NLNM). For periods which define the corners of the NLNM and NHNM polygons, Tables 4.1 and 4.2 give the displacement, velocity and acceleration power densities both in their respective kinematic units and in dB. A slightly different model was worked out by Berger et al. (2004) and is known as the GSN low-noise model. Fig. 4.3 also shows the lower envelopes for the PSDs of displacement and velocity. Displacements vary enormously between the short-period and the long-period end of the seismic spectrum. For the NLNM alone the variation is 260 dB (equivalent to 13 orders of magnitude in the signal amplitude) in the period range of seismological interest. The variation is reduced to about 130 dB for velocity and to 50 dB for acceleration. Understandably the PSD of acceleration is preferred for graphic representations. The noise peak of ocean microseisms around 5 s period (see 4.3.1) stands out most clearly here, as does the minimum near 0.04 Hz, termed "a window for earthquakes" by Savino et al. (1972). The height of the microseismic peak exhibits a strong seasonal variation. Another important minimum in the vertical-component seismic noise exists around 3 mHz which is important for free oscillation observations. The physical reasons for its existence have been discussed by Zürn and Wielandt (2007).

The ocean microseisms separate the two traditional domains of short-period ($T < 2$-3 s) and long-period seismology ($T > 10$s). Broadband recordings spanning over this peak were rare after WWII, especially in the western world after the introduction of the US World-Wide Standard

Seismograph Network (WWSSN). But even nowadays, with digital broadband-velocity recording being the standard almost everywhere, it is usually necessary to filter data into the two bands above or below this peak to clearly detect seismic phase arrivals above the noise.

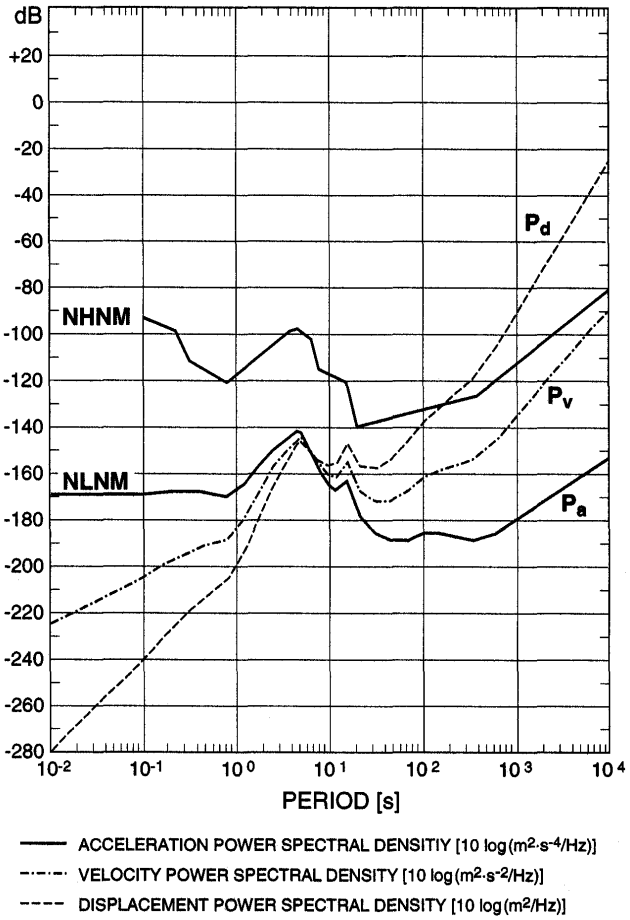

Fig. 4.3 Envelope curves of acceleration noise power spectral density $\mathbf{P_a}$ (in units of dB related to 1 $(m/s^2)^2/Hz$) as a function of noise period (according to Peterson, 1993). They define the new global high (NHNM) and low noise models (NLNM) which are currently the accepted standard curves for generally expected limits of seismic noise. Exceptional noise may exceed these limits. For the NLNM the related curves calculated for the displacement and velocity power spectral density $\mathbf{P_d}$ and $\mathbf{P_v}$ in units of dB with respect to 1 $(m/s)^2/Hz$ and 1 m^2/Hz are given as well (reproduced from Journal of Seismology, 2, 1998, "Conversion and comparability of data presentations on seismic background noise", P. Bormann, p. 39, Fig. 2; © Kluwer Academic Publishers, with permission of Kluwer Academic Publishers).

It is often desirable to plot many PSD curves into one graph – for example, PSDs from all stations of a large network at the same time, or from many hourly or daily records of a single station. In that case, certain areas of a graph like Fig. 4.3 may become completely black, and it may be impossible to distinguish or label individual curves. A better way is then not to plot individual PSD curves but to represent the ***probability density function or PDF*** of the ensemble of PSD curves. (The PDF is unrelated to the .pdf format for electronic documents.) The PDF measures the relative density of PSD values (how many of the observed values lie in a small area of the graph) and is encoded with a color scale (Figure 4.4). PDF software is part of software packages like PQLX (http://earthquake.usgs.gov/ research/software/pqlx.php;

USGS Open-File Report 10-1292) or SEISCOMP3 (http://www.seiscomp3.org/). In interactive versions, the user can click into the plot area and obtain a listing of those seismic records that have PSDs with the selected combination of frequency and PSD level. This can help to identify the cause of elevated noise levels, such as traffic, weather, or technical problems.

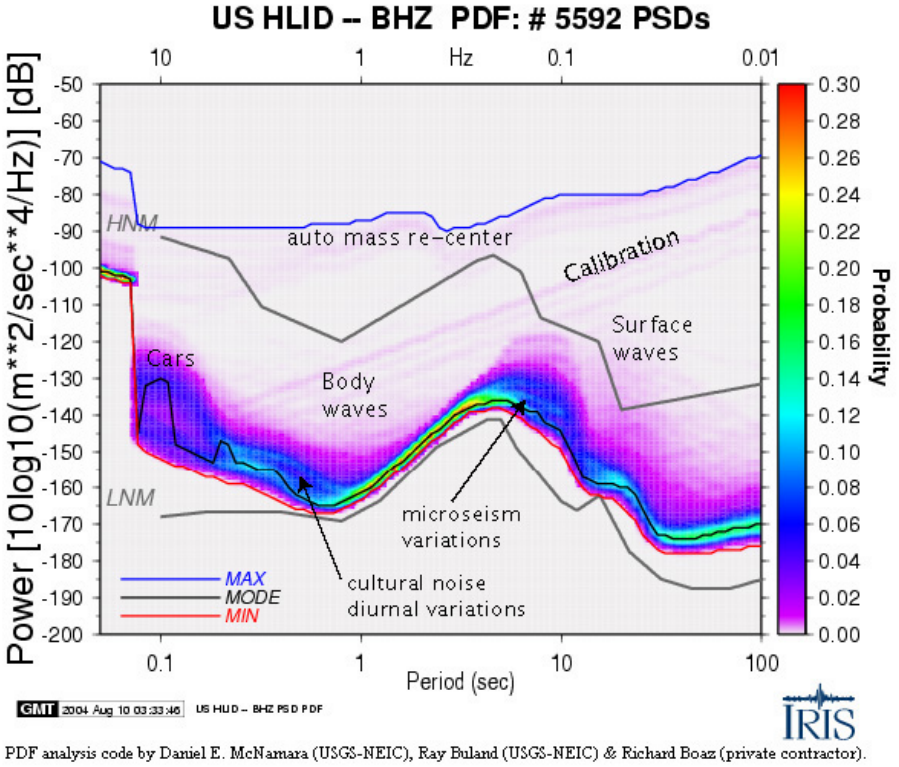

Fig. 4.4 An example for color-coding the density (in the drawing plane) of curves of Power Spectral Density vs. period: a PDF diagram. IRIS DMC, Seattle.

Table 4.1 Noise power spectral densities at selected periods and in different units which define the new global low-noise model (NLNM) as given by Peterson (1993). Peterson published values for $\mathbf{P_a}$ [dB] only. The respective numbers for ground acceleration (P_a), velocity ($\mathbf{P_v}$ and P_v) and displacement ($\mathbf{P_d}$ and P_d) have been calculated using Eqs. (4.4) to (4.8). Between the listed periods the values are to be linearly interpolated in a PSD-logT diagram.

T [s]	P_a [m^2s^{-4}/Hz]	$\mathbf{P_a}$ [dB]	P_v [m^2s^{-2}/Hz]	$\mathbf{P_v}$ [dB]	P_d [m^2/Hz]	$\mathbf{P_d}$ [dB]
0.10	1.6×10^{-17}	- 168.0	4.1×10^{-21}	- 203.9	1.0×10^{-24}	- 239.9
0.17	2.1×10^{-17}	- 166.7	1.6×10^{-20}	- 198.1	1.1×10^{-23}	- 229.4
0.40	2.1×10^{-17}	- 166.7	8.7×10^{-20}	- 190.6	3.5×10^{-22}	- 214.6
0.80	1.2×10^{-17}	- 169.2	1.9×10^{-19}	- 187.1	3.2×10^{-21}	- 214.5
1.24	4.3×10^{-17}	- 163.7	1.7×10^{-18}	- 177.8	6.5×10^{-20}	- 191.9
2.40	1.4×10^{-15}	- 148.6	2.0×10^{-16}	- 157.0	3.0×10^{-17}	- 165.3
4.30	7.8×10^{-15}	- 141.1	3.6×10^{-15}	- 144.4	1.7×10^{-15}	- 147.7
5.00	7.8×10^{-15}	- 141.1	4.9×10^{-15}	- 143.1	3.1×10^{-15}	- 145.1
6.00	1.3×10^{-15}	- 149.0	1.1×10^{-15}	- 149.4	1.0×10^{-15}	- 149.8
10.00	4.2×10^{-17}	- 163.8	1.0×10^{-16}	- 159.7	2.7×10^{-16}	- 155.7
12.00	2.4×10^{-17}	- 166.2	8.7×10^{-17}	- 160.6	3.2×10^{-16}	- 155.0
15.60	6.2×10^{-17}	- 162.1	3.8×10^{-16}	- 154.2	2.3×10^{-15}	- 146.3
21.90	1.8×10^{-18}	- 177.5	2.2×10^{-17}	- 166.7	2.6×10^{-16}	- 155.8
31.60	3.2×10^{-19}	- 185.0	7.9×10^{-18}	- 171.0	2.0×10^{-16}	- 156.9

45.00	1.8×10^{-19}	- 187.5	9.1×10^{-18}	- 170.4	4.7×10^{-16}	- 153.3
70.00	1.8×10^{-19}	- 187.5	2.2×10^{-17}	- 166.6	2.8×10^{-15}	- 145.6
101.00	3.2×10^{-19}	- 185.0	9.7×10^{-17}	- 160.9	2.1×10^{-14}	- 136.8
154.00	3.2×10^{-19}	- 185.0	1.8×10^{-16}	- 157.2	1.1×10^{-13}	- 129.4
328.00	1.8×10^{-19}	- 187.5	4.9×10^{-16}	- 153.1	1.3×10^{-12}	- 118.7
600.00	3.5×10^{-19}	- 184.4	3.2×10^{-15}	- 144.8	3.0×10^{-11}	- 105.2
10^4	6.5×10^{-16}	- 151.9	3.5×10^{-14}	- 87.9	4.1×10^{-3}	- 23.8
10^5	4.9×10^{-11}	- 103.1	1.2×10^{-2}	- 19.1	2.6×10^{6}	+ 65.0

Table 4.2 Noise power spectral densities at selected periods and in different units which define the new global high-noise model (NHNM) as given by Peterson (1993). Peterson published values for $\mathbf{P_a}$ [dB] only. The respective numbers for ground acceleration (P_a), velocity ($\mathbf{P_v}$ and P_v) and displacement ($\mathbf{P_d}$ and P_d) have been calculated using Eqs. (4.4) to (4.8). Between the listed periods the values are to be linearly interpolated in a PSD-logT diagram.

T [s]	P_a [m^2s^{-4}/Hz]	$\mathbf{P_a}$ [dB]	P_v [m^2s^{-2}/Hz]	$\mathbf{P_v}$ [dB]	P_d [m^2/Hz]	$\mathbf{P_d}$ [dB]
0.10	7.1×10^{-10}	- 91.5	1.8×10^{-13}	- 127.5	4.5×10^{-17}	- 163.4
0.22	1.8×10^{-10}	- 97.4	2.2×10^{-13}	- 126.5	2.7×10^{-16}	- 155.6
0.32	8.9×10^{-12}	- 110.5	2.3×10^{-14}	- 136.4	6.6×10^{-17}	- 162.2
0.80	1.0×10^{-12}	- 120.0	1.6×10^{-14}	- 137.9	2.6×10^{-16}	- 155.8
3.80	1.6×10^{-10}	- 98.0	5.8×10^{-11}	- 102.4	2.1×10^{-11}	- 106.7
4.60	2.2×10^{-10}	- 96.5	1.2×10^{-10}	- 99.2	6.4×10^{-11}	- 101.9
6.30	7.9×10^{-11}	- 101.0	8.0×10^{-11}	- 101.0	7.9×10^{-11}	- 101.0
7.90	4.5×10^{-12}	- 113.5	7.1×10^{-12}	- 111.5	1.4×10^{-11}	- 109.5
15.40	1.0×10^{-12}	- 120.0	6.0×10^{-12}	- 112.2	3.6×10^{-11}	- 104.4
20.00	1.4×10^{-14}	- 138.5	1.4×10^{-13}	- 128.4	1.4×10^{-12}	- 118.4
354.80	2.5×10^{-13}	- 126.0	8.0×10^{-10}	- 91.0	2.6×10^{-6}	- 55.9
10^4	9.7×10^{-9}	- 80.1	2.5×10^{-2}	- 16.1	6.2×10^{4}	+ 47.9
10^5	1.4×10^{-5}	- 48.5	3.6×10^{3}	+ 35.5	9.0×10^{11}	+ 119.6

4.3.2 Instrumental self-noise

Instrumental self-noise was no problem with classical seismographs of relatively low magnification and with large masses. According to Wielandt (see Chapter 5, section 5.5) the Brownian (thermal) motion of the seismic mass is a limiting factor only when the mass is very small (less than a few grams). Presently manufactured observatory-grade seismometers have sufficient mass to make the Brownian noise negligible against noise from other sources. However, all modern seismographs use semiconductor amplifiers. They produce, like other active (power-dissipating) electronic components, continuous electronic noise. Its origin is manyfold but ultimately related to the quantization of the electric charge. Electromagnetic transducers, such as those used in geophones, also produce thermal electronic noise (resistor noise, Johnson noise). The contributions from semiconductor noise and resistor noise are often comparable, and together limit the sensitivity, i.e., the achievable resolution, of the system. In sections 5.5.6 and 5.5.7 Wielandt discusses self-noise of short-period electromagnetic seismographs and of modern broadband force-balance seismometers.

It is not possible to distinguish between ground noise and instrumental self-noise in the signal recorded from a single instrument. To identify the presence of instrumental noise one can run two or more instruments close to each other on the same pier (so-called ***Huddle test***). After

correction for the transfer function of these instruments the ground noise will appear in their records as being coherent. Consequently, the difference signal between the various instruments will represent the incoherent part produced by the instruments themselves. However, it remains the question which of the instruments contributes at what degree to the difference signal? In order to distinguish between the contributions from these seismometers Sleeman et al. (2006) proposed a Huddle test with three seismometers. The power spectral density of self-noise of seismometer 1 then is

$$N_1(f) = P_1(f)\,[1 - (C_{12}(f) \cdot C_{13}(f))/C_{32}(f)] \tag{4.12}$$

where f = frequency, $P_1(f)$ = power spectral density of the output of seismometer 1, and $C_{kl}(f)$ = coherence spectrum for seismometers k and l.

Besides their more or less stationary self-noise, seismometers occasionally produce transient disturbances. They may originate in stressed mechanical parts, in slightly defective semiconductors, or in outgassing porous materials. The level of instrumental noise also depends on the installation. Only part of the instrumental noise is self-noise in a strict sense. Another part can be eliminated by careful shielding against environmental disturbances. For identifying and measuring instrumental noise see Chapter 5, sections 5.5.6 and 5.5.7. Figure 4.5 shows typical levels of self-noise for short-period and broadband seismometers.

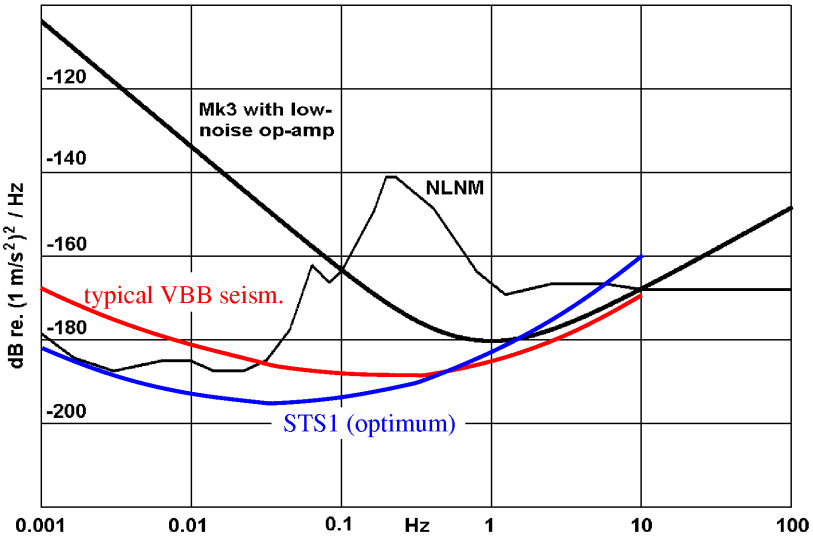

Fig. 4.5 Typical self-noise of different seismometer types in comparison with the NLNM (thin black curve). Black: a short-period, passive Sensonics Mk3 seismometer with a low-noise preamplifier (predicted; compare the theoretical curves for different circuits in section 5.5.6 of Chapter 5). The resolution can be improved by using a larger seismic mass as in the Geotech GS-13 or some historical electromagnetic seismometers. Red: typical performance of well-installed VBB seismometers (such as STS2, Trillium 240, Guralp CMG-3T, or Reftek 151-120). Blue: at very low seismic frequencies, the STS1 (originally designed in 1975) is still the most sensitive broadband seismometer when properly installed. The STS1 is the primary sensor of the Global Seismic Network (GSN).

4.4 Comparing spectra of transient and stationary signals

4.4.1 Bandwidth and amplitude

For the purpose of the following discussion, we must subdivide the signal categories "transient" and "stationary" further: the transient signals into impulsive and oscillatory ones, the stationary signals into random signals (noise) and monochromatic sinewaves. A typical seismogram, especially a dispersed train of surface waves, are in the "oscillatory" category. Impulsive seismic signals are rare in nature but at least theoretically, the seismic signal near the focus of an earthquake should be impulsive. Ambient seismic noise is often a superposition of all types, the "random" components being due to a large number of independent sources (traffic, wind, waves in the ocean), "transient" components being caused by identifiable sources such as passing cars, and nearly monochromatic components originating from machinery such as sawmills and pumps.

When the PSD of a stationary signal is constant over the bandwidth of a seismograph or a filter and we reduce the filter bandwidth, then the signal power is proportional to the bandwidth because it is the integral of a constant power density over the bandwidth. The rms amplitude of the signal, which is the square root of the power, must therefore be proportional to the square root of the bandwidth. This explains why a "spectral amplitude density" cannot be generally defined; such a definition would imply that the amplitude is generally proportional to the bandwidth, which it is not. It may nevertheless be so in special cases. The peak amplitude of an impulsive signal can be proportional to the bandwidth when the width of the pulse is inverse to its bandwidth so that the total energy does not increase as the square of the peak amplitude. On the other hand, the peak amplitude of a sweep signal (a sinewave with decreasing or increasing

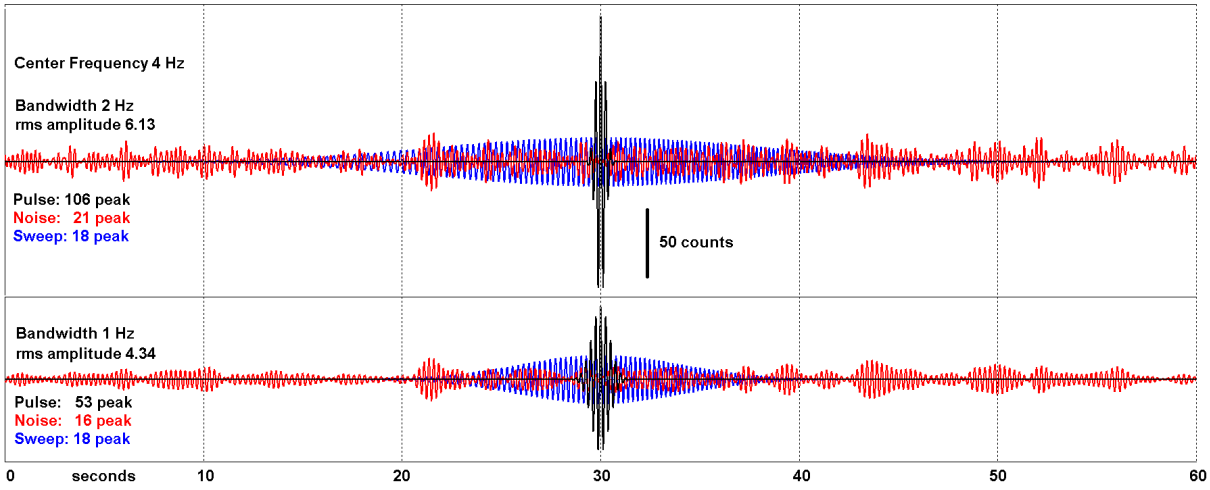

Fig. 4.6 Each trace shows three signals with identical amplitude spectra but different phase spectra. All traces were obtained by band-pass filtration of a signal with a constant Power Spectral Density with a Gaussian filter whose center frequency was 4 Hz and total 1/e-bandwidth 2 Hz (top), resp. 1 Hz (bottom). The phase was chosen so that the complex spectrum represented an impulsive signal (a ***wavelet***, black), random noise (red), and a sweep (blue). The Gaussian wavelet is the shortest pulse that can be obtained in the given bandwidth. As discussed above, its peak amplitude is proportional to the bandwidth, that of the sweep is (almost) constant, and that of the noise is roughly proportional to the square root of the bandwidth. When the bandwidth is reduced, the pulse becomes broader, the noise smoother, and the sweep shorter.

frequency) may be nearly independent of the filter bandwidth. In this case the width of the signal in time decreases with the bandwidth, and again the total energy is proportional to the bandwidth. Fig. 4.6 illustrates the effect of bandwidth on the peak amplitude of different signal types. Consequences for the evaluation of seismograms are discussed in section 4.5.

4.4.2 The dynamic range of a seismograph

The ***usable dynamic range*** of a seismograph is in principle defined as the range of amplitudes between the smallest and the largest recordable signal. The ability to record small seismic signals is limited by ambient seismic noise, self-noise of the sensor and the digitizer, and non-seismic environmental noise to which the sensor responds. With this definition the smallest recordable signal does not only depend on technical properties of the instrument but also on seismic noise and other local conditions. For large signals a limit is reached when signals are clipped or otherwise unacceptably distorted. This limit is called the operating range of the instrument.

This definition of the dynamic range may seem clear and obvious, but it is not. The problem is that both noise and clip levels are frequency-dependent, and we must compare them in different frequency bands. However, as we have just seen, narrowing the bandwidth can change the amplitude ratios when the signals are not of the same type. The dynamic range not only depends on frequency but also on the bandwidth. We cannot define it as a function of frequency alone. This becomes clear when we investigate the detectability of a pure sinewave in the presence of random noise. An early discussion of this topic with a view to quantization noise was published by Zürn (1974).

Theoretically, no matter how small the amplitude of a sinewave is, it can always be extracted from random noise provided that we can observe the signals over an unlimited time. We can reduce the amplitude of the noise below any given level by reducing the bandwidth while the amplitude of the sinewave remains the same – we must however wait for the response of the filter to the sinewave to reach a steady state. So the dynamic range of a sensor for sinusoidal signals is theoretically infinite. A meaningful definition of the dynamic range must refer to a seismologically useful finite bandwidth in which all signal amplitudes are compared, for example, a bandwidth of one octave or one-half octave around each frequency. The bandwidth should be small enough so that distinguishable signals (such as primary and secondary microseisms, see paragraph 4.6.1) can be resolved on the frequency scale, but large enough to preserve their amplitude. (Some remarks on this topic are also found in paragraph 4.5.2.) Equivalently, considering the uncertainty principle of the Fourier transformation, one could as well specify a realistic time of observation, which cannot be smaller than a few cycles of the signal. This involves some arbitrariness and therefore it is necessary to explain what "dynamic range" exactly means in a specific case. Evans et al. (2010) suggest a particular choice that could be used as a standard.

In contrast to classical analog recordings on paper, which had a dynamic range of some 40-50 dB only, modern digital data loggers with a 24 bit ADC (Analog-to-Digital Converter; see Chapter 6) allow digital recordings with a dynamic range of $6 \times 24 = 144$ dB. This allows to cover a rather wide range of signal amplitudes and still to resolve seismic noise at the NLNM level (see Fig. 4.7). Covering a range of 144 dB in analog form would correspond to an amplitude range between 1 mm and 16 km!

4.4.3 Representing clip levels, signals, and noise in the same diagram

Once we have decided to represent seismic or instrumental noise by its amplitude in a small but seismologically useful bandwidth, we can at least approximately represent clip levels, typical amplitudes of seismic signals, and noise levels in the same diagram. Figure 4.7 is an example. In this case the author of the figure has chosen to annotate the vertical axis with "equivalent earth peak acceleration", which is perfect to describe clip levels, adequate to describe expected amplitudes of earthquake signals, and a bit awkward for noise because no simple relationship exists between its peak and rms amplitudes. Under certain assumptions, however, an "average peak amplitude" of the noise can be defined, which has been done here. The assumed bandwidth is 1/3 octave.

Alternatively, one might express all signals as rms amplitudes. This would be perfect for stationary noise, a bit inconvenient for clip levels (because the rms amplitude must be multiplied with $\sqrt{2}$ to obtain the peak amplitude of a sinewave), and awkward for seismic signals because their rms amplitude depends on the averaging time. It makes no sense to average the energy present in, say, one-half octave over the whole length of the seismogram since that energy is usually concentrated in a much shorter interval. One would rather determine the rms amplitude from the largest few cycles at each frequency. Despite the inherent arbitrariness, this kind of diagram has proved very useful for a graphical representation of seismograph performance.

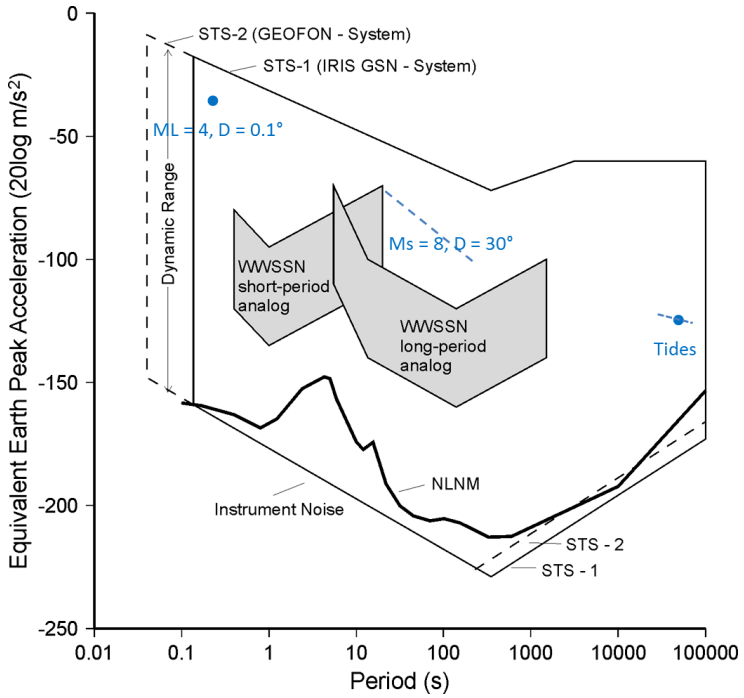

Fig. 4.7 A representation of the bandwidth and dynamic range of conventional analog (WWSSN short- and long-period) and digital broadband seismographs (STS1/VBB and STS2 with good shielding; see DS 5.1 and IS 5.4). The depicted lower bound is determined by the instrumental self-noise. The scale is in decibels (dB) relative to 1 m/s^2. Noise is measured in a constant relative bandwidth of 1/3 octave and represented by "average peak" amplitudes equal to 1.253 times the RMS amplitude. NLMN is the global New Low Noise Model according to Peterson (1993). Modified version of Fig. 7.48 in Chapter 7. Amplitudes of typical signals according to J. M. Steim (in blue).

4.4.4 Approximate conversion of power densities into recording amplitudes

According to Aki and Richards (1980) the *maximum* amplitude of a wavelet ***f(t)*** near ***t*** = 0 can be *roughly approximated* by the product of what they call "amplitude spectral density" and the bandwidth of the wavelet, i.e.,

$$f(t)_{t=0} = |F(\omega)| \; 2\,(f_u - f_l) \tag{4.13}$$

with f_u and f_l being the upper and lower corner frequencies of the band-passed signal. (Remember that such an approximation is only possible for signals whose energy is maximally concentrated in time.) Likewise, if the power spectral density of noise is defined according to Eq. (4.5) then we get for the *mean square amplitude* of noise in the time domain:

$$< f^2(t) > = 2P\,(f_u - f_l) \tag{4.14}$$

This is of course a simplified version of the general rule that the power spectral density (PSD) must be integrated over the passband of a filter to obtain the power (or *mean square amplitude*) at the output of the filter. The square root of this power is then the *root mean square* (RMS) or effective amplitude

$$a_{RMS} = [2P \times (f_u - f_l)]^{1/2} \tag{4.15}$$

If the power spectral density is defined according to the engineering approach (see 4.2.3.1) as $P_e = 2P$, then

$$a_{RMS} = [P_e \times (f_u - f_l)]^{1/2} \tag{4.16}$$

We note again that stationary signals must be characterized by their PSD, and **specifying seismic noise by its RMS amplitudes is meaningless without definition of the bandwidth.** The values given by the NLNM and NHNM in Fig. 4.3 and Tabs. 4.1 and 4.2, respectively, follow the engineering convention. For consistency, we will use this convention for the rest of this chapter.

For the reasons discussed in section 4.4, it is often necessary to represent the amplitude of noise (whether rms or average-peak) in a ***constant relative bandwidth*** over the whole frequency range. This means, the bandwidth B around each frequency f_0 is a fixed fraction or multiple of f_0. The lower and upper band limits, f_l and f_u, are chosen so that f_0 is the geometric mean of the two (so f_0 appears in the middle between f_l and f_u on a logarithmic frequency scale). When the bandwidth is n octaves or m decades (n and m normally being fractions, not integers), then the following relationships hold:

$$f_l = 2^{-n/2} f_0, \quad f_u = 2^{n/2} f_0 \,, \; B = (2^{n/2} - 2^{-n/2})\, f_0 \tag{4.17}$$

and (4.16) can be written as

$$a_{RMS} = [P_l \times (f_u - f_l)]^{1/2} = [P_e \times f_0 \times (2^{n/2} - 2^{-n/2})]^{1/2} \tag{4.18}$$

Octaves can be converted easily into decades and vice versa by using the relation

$$m = n \cdot \log_{10}(2) = \mathrm{n} \cdot 0.3010 \tag{4.19}$$

Aki and Richards (1980, vol.1, p. 498) converted PSD into ground motions by putting the bandwidth of the noise signal at half the considered (center) frequency, i.e., by assuming $f_u - f_l = 0.5\, f_o$. This corresponds to a relative bandwidth of roughly 2/3 octave. Using the definition of power on which Eq. (4.14) is based they obtained $a_{RMS} = (P \times f_o)^{1/2}$.

Table 4.3 Bandwidth B of typical octave and decade filters centered at f_0.

Octaves	***B***	**Decades**	***B***
1	$0.707\, f_0$	1	$2.846\, f_0$
2/3	$0.466\, f_0$	1/2	$1.215\, f_0$
1/2	$0.348\, f_0$	1/3	$0.786\, f_0$
1/3	$0.232\, f_0$	1/6	$0.386\, f_0$

Other authors (e.g., Fix, 1972; Melton, 1978) have used an integration bandwidth of 1/3 octave (a standard bandwidth in acoustics) for computing RMS amplitudes from PSD. Melton reasoned that this is nearly ±10% about the center period in width and thus close to the tolerance with which an analyst can measure the period on an analog seismogram. Therefore, using a 1/3 octave bandwidth seemed to him a reasonable convention for calculating RMS noise amplitudes from PSD. The differences, as compared to RMS values based on 1/4 or 1/2 octave bandwidths, are less than 20%. But 1/3 octave amplitudes will be only about 70% or 50% of the respective RMS amplitudes calculated for 2/3 or 4/3 octave bandwidth, respectively. Typical response curves of short-period narrowband analog seismographs for recording transient teleseismic body-wave onsets have bandwidths between about 1 and 2 octaves. For deriving spectral magnitudes, Duda and Kaiser (1989) filtered broadband records with one octave wide bandpasses in intervals of one octave distance with center periods of 0.25 s, 0.5 s, … 32 s, and 64 s; see Fig. 3.55 in Chapter 3). Fig. 4.8 represents the NLNM (compare Fig. 4.3) as rms amplitudes in a constant relative bandwidth of 1/6 decade.

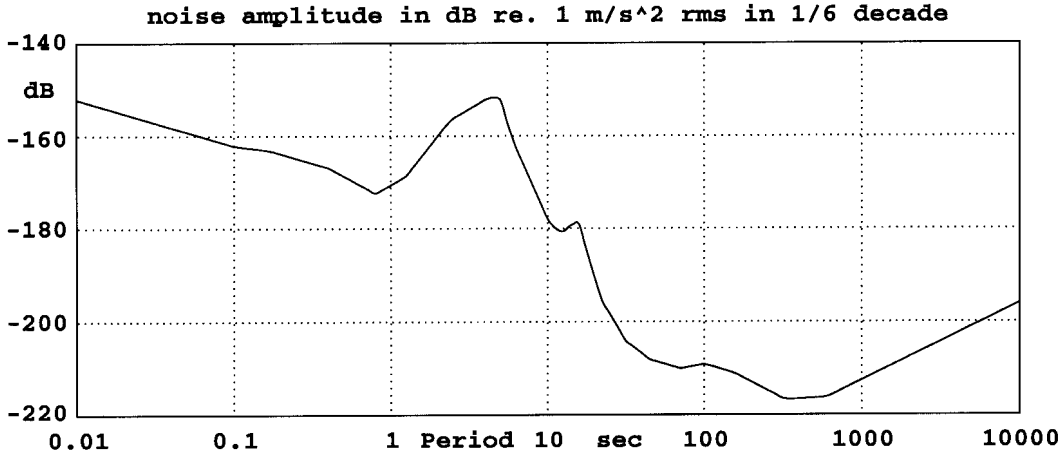

Fig. 4.8 The USGS New Low Noise Model, here expressed as RMS amplitudes of ground acceleration in a constant relative bandwidth of one-sixth decade, corresponding approximately to 1/2 octave (see Tab. 4.1). A bandwidth of 1/6 decade extends from 82.5% to 121% of the central frequency f_o. The corresponding values for 1/2 octave are 84% and 119%.

There is a 95% probability that the instantaneous amplitude of random noise with a Gaussian amplitude distribution will lie within a range of $\pm 2\boldsymbol{a}_{RMS}$. Peterson (1993) showed that both broadband and long-period noise amplitudes follow closely a Gaussian probability distribution. This is true for largely natural ambient noise, often not, however, for short-period and broadband noise in urban and industrialized areas, There the noise is often dominated by transient or periodic signals (see, e.g., Figs. 7.17, 7.19, and 7.21 in Chapter 7; also Groos and Ritter, 2009 and section 4.6.3). Yet, in case of a Gaussian probability distribution, the absolute peak amplitudes of the narrowband filtered signal envelopes should follow a Rayleigh distribution. In the case of an ideal Rayleigh distribution the theoretical *average peak amplitudes* (APA) are 1.253 a_{RMS}. From test samples of narrowband filtered VBB and LP noise records Peterson (1993) measured APA values between 1.194 and 1.275. Therefore, RMS amplitudes in 1/6-decade bandwidth correspond approximately to average peak amplitudes in 1/3 octave bandwidth. An example: According to Fig. 4.8 the minimum vertical ground noise between 10 and 20 s is at -180 dB relative to $1 m/s^2$. This corresponds to average peak amplitudes of $10^{-180/20}$ $m/s^2 = 1$ nm/s^2 in 1/3 octave bandwidth. Accordingly, the total average peak amplitude in this one octave band between 10 and 20 s is approximately $\sqrt{3}$ nm/s^2.

E. Wielandt offers an interactive program NOISECON which can be downloaded via the link from the NMSOP-2 front page to the listing ***Download programs and files***. It converts noise specifications into all kinds of standard and non-standard units and compares them to the USGS NLNM. EX 4.1 provides exercises by hand for calculating RBWs and transforming PSDs into $\boldsymbol{a}_{RMS}$ for various kinematic units and bandwidths. It is complemented also by several exercises combining eye-estimates and NOISECON applications for interpreting and converting noise spectra.

4.5 Seismograph response and waveform

4.5.1 Empirical case studies

While in recordings of type A with four-octave bandwidth, the first half cycle contains the largest amplitude, the maximum amplitude in records with 1/2 octave (type A´) and one octave bandwidth (type Tr) is reached only at the third half-swing. Also, the first motion amplitude in the one octave record Tr is strongly reduced as compared to that in record A with four octave bandwidth, despite having nearly the same peak magnification. Accordingly, we have to consider that in narrowband records of high magnification (as with WWSSN short-period seismographs; bandwidth about 1.5 octaves) the reduced first motion amplitudes might get lost in the presence of noise. Since reliable first motion polarity readings are crucial for the determination of fault plane solutions (see section 3.4 in Chapter 3) and discriminating earthquakes from explosions, narrowband recordings might result in an unacceptable loss of primary information.

Fig. 4.9 shows earthquake P-wave onsets recorded by short-period seismographs with 1-Hz seismometers but amplitude response curves of different bandwidth. The maximum amplitude of the P-wave onset in the – as compared to the filter in Fig. 4.11 - more narrowband Tr record is only about ½ of that in record A although seismographs have nearly the same peak magnification at 1 Hz for steady-state harmonic oscillations. And in record A´ the maximum amplitude is only twice as large, even though the A' instrument has four times larger peak amplification than instrument A.

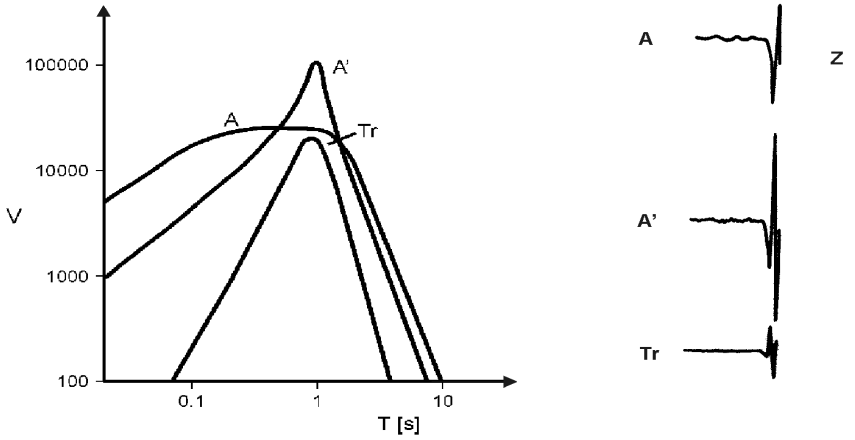

Fig. 4.9 Left: Displacement amplitude magnification curves of three traditional analog types of short-period seismographs used at seismic station MOX with 1/2 octave (type A´), one octave (Tr - trigger seismograph) and four octave bandwidth (type A), respectively; right: records with these seismographs of a P-wave onset of a deep earthquake at an epicentral distance of 72.3° and hypocentral depth of 544 km (copied from Bormann, 1973).

The following figures, 4.10 to 4.14, illustrate the difficulty of interpreting narrowband seismograms correctly with respect to polarities, amplitudes, and the presence and onset times of secondary arrivals.

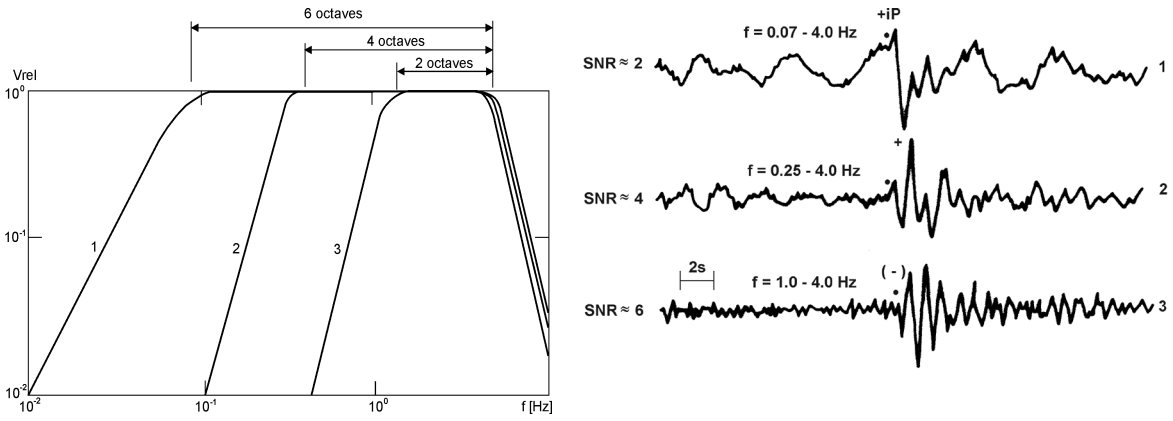

Fig. 4.10 A medium-period velocity-proportional digital broadband record (bandwidth almost 6 octaves between 0.07 – 4 Hz;) at station MOX of an underground nuclear explosion at the Nevada test site (upper record trace), and the same signal filtered with a 4-octave and 2-octave bandpass filter (middle and lower record trace). The positive first motion (to be expected from an explosion) is clearly seen in the BB record despite of the low SNR, but it is buried in the noise of the 2 octave record despite the general SNR improvement due to narrowband filtering. The different absolute amplitude levels in the three records have been normalized to the same peak amplitude.

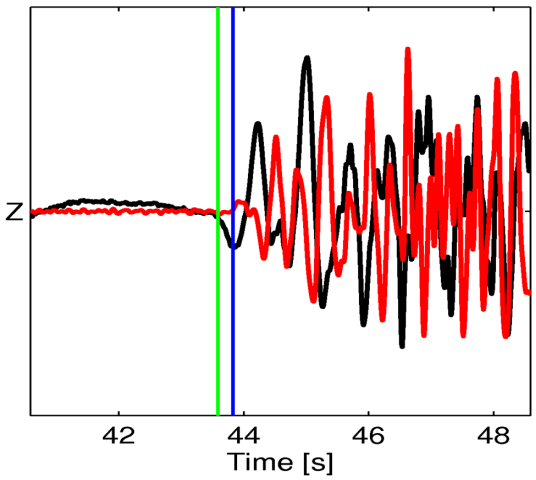

Fig. 4.11 Unfiltered (black) and filtered (red) local event waveform of a broadband record (Guralp CMG, 60s–50 Hz) using a 3rd order Butterworth bandpass filter (2-10 Hz). In the more narrow-band high-frequency filtered record the amplitude of the first oscillations is strongly reduced and the phase significantly shifted. The negative first motion, still distinct in the broadband record, is no longer recognizable (copy of Fig. 16.25 in Chapter 16 with permission of the authors Küperkoch et al., 2012)

This systematic underestimation of amplitudes of transient body-wave onsets of short duration in narrowband records - and thus of related magnitude estimates within the first few cycles as for many mb data (Chapter 3, section 3.2.5.2 and Fig. 3.46) - has been a matter of considerable debate between the American and Russian delegations in the early Geneva talks to achieve a Comprehensive Nuclear-Test-Ban Treaty (CTBT). In the Soviet Union standard seismographs with amplitude characteristics of type A (2 to 4 octaves) and broadband characteristics of type Kirnos with about 7 octaves bandwidth (Fig. 3.20 in Chapter 3 and Figure 1 in IS 3.7) were used to determine body-wave magnitudes, whereas American-designed WWSSN stations had a bandwidth of only about 1.5 octaves, and short-period P-wave amplitudes were measured within the first few cycles only for mb magnitude determinations (Engdal and Gunst, 1966). A consequence of these differences in magnitude determination was that the American delegation reported a much larger number of weak, unidentified seismic events per year than the Soviet delegation and therefore felt that they required hundreds of U.S. unmanned stations on Soviet territory as well as the possibility for on-site inspections. This blocked, amongst other reasons, the agreement on a comprehensive test-ban treaty for two decades. Today these problems are more of historical interest. Present days analysts may filter digital broadband data as desired. But it remains a problem to decide what filter is appropriate for solving best the given task. Therefore, analysts should be aware of both the reasons and possible size of filter effects. For assuring globally compatible magnitude data, however, the International Association of Seismology and Physics of the Earth's Interior (IASPEI, 2005 and 2013 and IS 3.3) has now agreed on some classical filter standards (such as Wood-Anderson, WWSSN-SP and WWSSN-LP) to be applied before measuring the amplitudes and periods for the most widely used types of magnitudes while other responses, such as the Kirnos-D displacement broadband, have proven to be best suited for teleseismic secondary phase recognition and onset time picking .

A narrower bandwidth causes a longer and more oscillating record of an impulsive onset. This makes it difficult to recognize, in narrowband records, secondary onsets following closely behind the first one, e.g., onset sequences due to a multiple earthquake rupture (Fig. 4.12), depth phases in the case of shallow earthquakes or branching/crossing of travel-time curves (see Chapter 2 and Fig. 4.13). But the identification and proper time picking of such closely spaced secondary arrivals may be crucial for a better understanding of complex rupture processes, for improved estimates of hypocenter depth or for studies of the fine structure of the Earth.

It is crucial, therefore, to record seismic signals with as large a bandwidth and with as high a linearity, resolution and dynamic range as possible, thus preserving the primary information with least distortion. Filtering should only be applied afterwards, as required for special purposes. With feedback-controlled broadband seismometers and digital data loggers with 24 bit resolution being common nowadays, this is no longer a problem (see Chapters 5 and 6). In Fig. 4.14 it is clearly recognizable that in the displacement-proportional broadband record of about 10 octaves bandwidth the P-wave onset looks rather simple (negative impulse with only slight positive over-swing of the second half-cycle). Its appearance resembles the expected source displacement pulse in the far field (see Fig. 2.4).

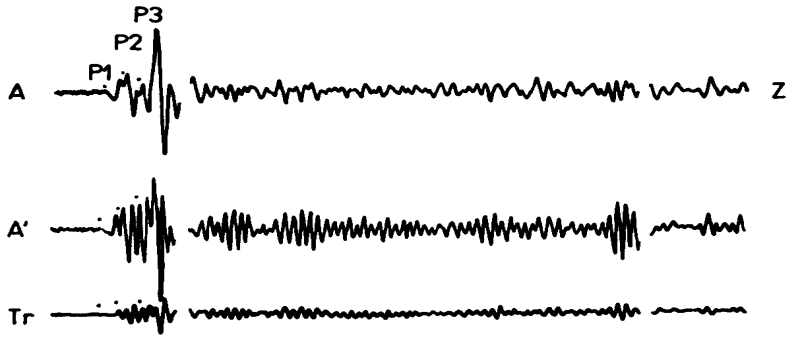

Fig. 4.12 Short-period records of station MOX according to Bormann (1973) of a multiple rupture event at Honshu (D = 88.0°) with different amplitude response characteristics according to Fig. 4.9 left.

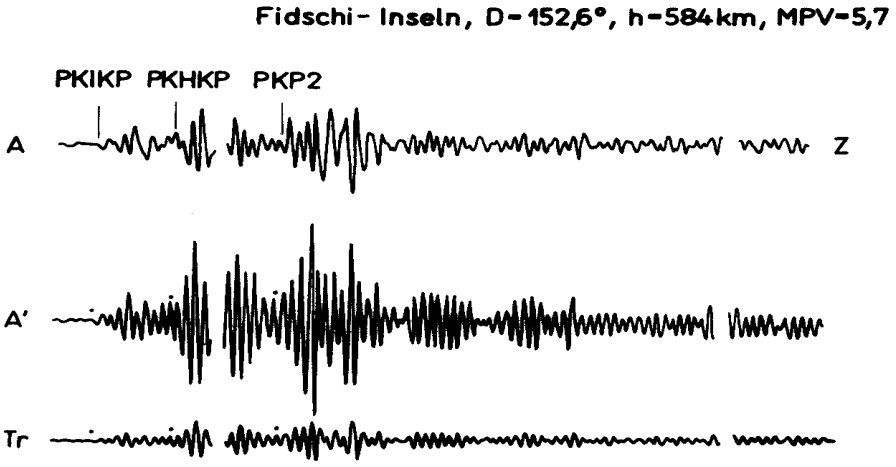

Fig. 4.13 Short-period records of station MOX according to Bormann (1973) of a sequence of core phases corresponding to the travel-time branches PKPdf (PKIKP), PKPbc (old PKHKP) and PKPab (PKP2) (see Chapter 11) with different amplitude response characteristics according to Fig. 4.9 left.

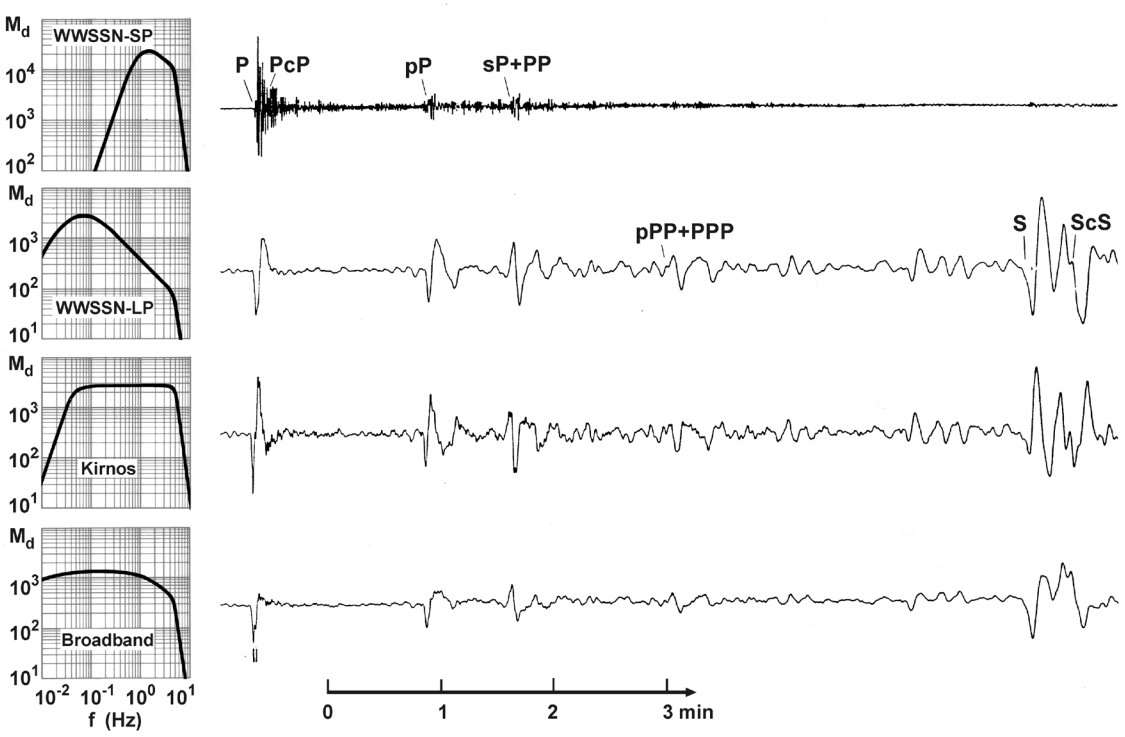

Fig. 4.14 Records of a deep earthquake (h = 570 km, D = 75°) at the Gräfenberg Observatory, Germany. They have been derived by filtering a velocity-proportional digital broadband record (passband between 0.05 and 5 Hz) according to the response curves of some traditional standard characteristics (WWSSN_SP and LP, Kirnos) while the bottom trace shows the result of computational restitution of the (nearly real) true ground displacement by extending the lower corner period To well beyond 100s (see text) (from Buttkus, 1986).

4.5.2 Theoretical considerations on signal distortion in seismic records

The basic theory of seismometry is outlined in Chapter 5. For a more comprehensive introduction to general filter theory and its applications in digital seismology (with exercises) see "Of Poles and Zeros: Fundamentals of Digital Seismology" by Scherbaum (3rd revised edition, 2007). The book is accompanied by a CD-ROM "Digital Seismology Tutor" by Schmidtke and Scherbaum, which is a very versatile tutorial tool for demonstrating signal analysis and synthesis. E. Wielandt also offers the program **filtdemo.** It can be downloaded via the link to *Download Programs & Files* on the NMSOP-2 front page or via Internet (http://www.geophys.uni-stuttgart.de/~erhard/downloads/ or http://www.software-for-seismometry.de/). Therefore, we will not dwell on it further, however, we will illustrate by way of example some of the essential effects of signal distortion by the transfer function of the seismograph. Signal distortion due to wave propagation effects in the Earth and ways how to eliminate at least some of them are discussed in Chapter 2.

As implied by Eq. (4.2), a Dirac (or needle) impulse (see Chapter 5, section 5.2.4) in the time domain is equivalent to a constant ("white") amplitude spectrum in the frequency domain. Thus, if the far-field seismic source pulse comes close to a needle impulse of very short duration (e.g., an explosion) we would need in fact a seismograph with (nearly) an infinite bandwidth in order to be able to reproduce this impulse-like transient signal. On the other hand, a

monochromatic harmonic signal corresponds to just one spectral line in the frequency spectrum, or, the other way around, if the input signal is a needle impulse with an infinite spectrum but the bandwidth of the seismograph is extremely narrow, then the output signal would not be a needle impulse but rather a slowly growing and decaying sinusoid. Fig. 4.15 depicts these extreme cases and Fig. 4.16 sketches seismographic recordings of an impulse sequence with qualitatively different response characteristics.

According to theoretical considerations by Seidl and Hellweg (1988), the seismometer period T_o has to be about 100 times larger than the duration τ_s of the source-time input function when the source signal shape and its "signal moment" (area under the impulse time curve) is to be reproduced with a relative error < 8 %. As a rule of thumb, these authors state that the relative error is less than about 10% if $T_o > 20\ \pi\ \tau_s$. This means that extreme long-period seismographs would be required to reproduce with sufficient accuracy the displacement impulse of strong seismic events.

By "signal restitution" (i.e., instrument response correction or "deconvolution") procedures (Seidl, 1980; Seidl and Stammler, 1984; Seidl and Hellweg, 1988; Ferber, 1989) the eigenperiod of long-period feedback seismometers such as STS1 (T_o = 360 s) and STS2 (T_o = 125 s) can be computationally extended - in the case of high signal-to-noise ratio - by a factor of about 3 to 10, and thus the very low-frequency content of the signals can be retrieved. Simulations of standard frequency responses from BB records are available in some of the software packages for signal pre-processing (e.g., PREPROC, Plešinger et al. 1996) or seismogram analysis (e.g., SEISAN, Havskov and Ottemöller, 1999 b, and Seismic Handler by K. Stammler; see ftp://ftp.geo.uib.no/pub/seismo/SOFTWARE/SEISAN/ and http://www.szgrf.bgr.de/sh-doc/index.html, respectively).

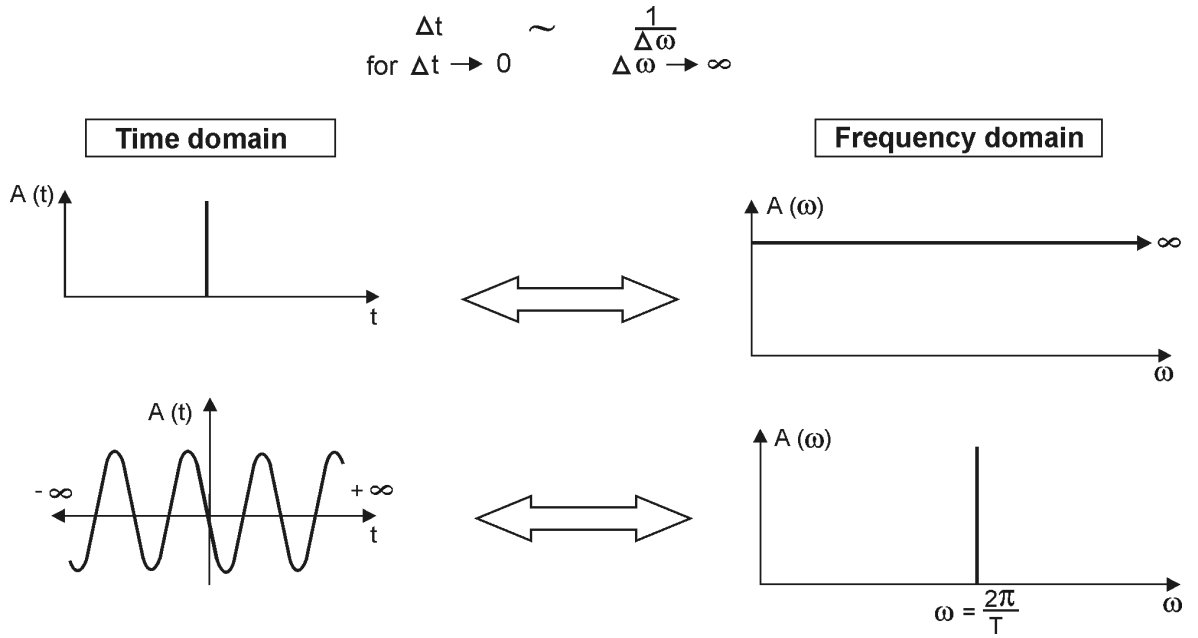

Fig. 4.15 Sketch of the equivalent representation of a needle impulse (above) and a stationary infinite monochromatic harmonic signal (below) in the time and frequency domain.

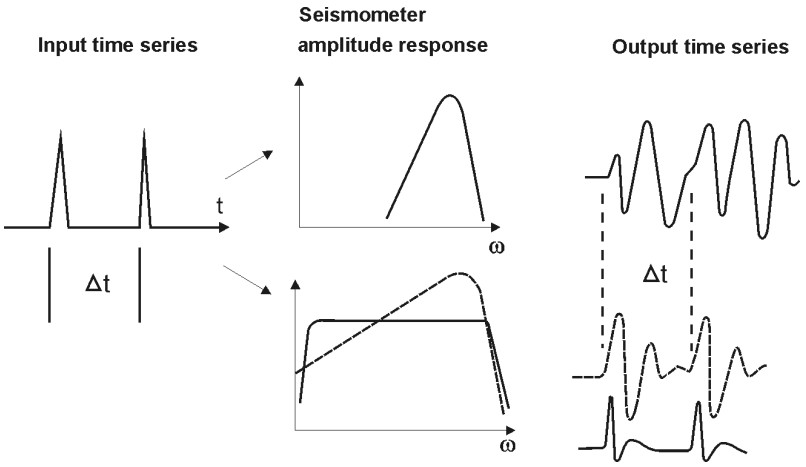

Fig. 4.16 Schematic illustration of the appearance of a sequence of seismic input impulses in record outputs of seismographs with narrow-band displacement response (uppermost trace) and broadband responses (lower traces: broken line – velocity response, full line – displacement response).

Fig. 4.17 shows the very different response of three standard seismograph systems of different damping and bandwidth to a synthetic ground displacement input according to the Brune model of earthquake shear dislocation. The response has been simulated by using the PITSA seismological analysis software of Scherbaum and Johnson (1992). For the amplitude response of the seismographs of type Wood-Anderson (WA), Kirnos, WWSSN long-period (LP) and WWSSN short-period (SP) see Fig. 3.20 in Chapter 3.

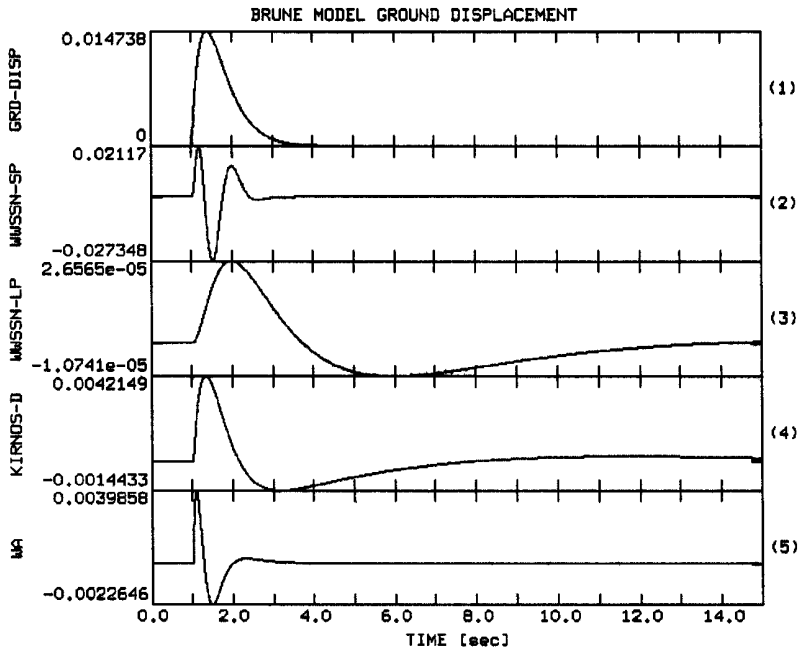

Fig. 4.17 Distortion of a synthetic ground displacement signal according to the Brune model of earthquake shear dislocation (top trace) by standard seismograph systems (for their response curves see Fig. 3.20 in Chapter 3) (from Scherbaum 2001, "Of Poles and Zeros", Fig. 10.2, p. 167; © Kluwer Academic Publishers, with permission of Kluwer Academic Publishers).

The strong distortion in narrowband recordings after transient onsets is due to their pronounced *transient response* (TR). It is due to the time required by the seismograph system to achieve the values of frequency-dependent magnification and phase shift determined by its amplitude- and phase-frequency characteristics for steady-state harmonic oscillations (see Chapter 5, Fig. 5.3 and Figure 1a and b in IS 5.2). In Fig. 4.17, the effect of phase-shift adaptation during the time of transient response is clearly seen, especially in the records of the WWSSN and Wood-Anderson short-period instruments. Accordingly, the period of the first half cycle appears to be much shorter than that of the second and third half cycle.

Fig. 4.18 compares the response of the same seismographs and of the SRO-LP seismograph with the unfiltered velocity broadband record of the STS2 (see DS 5.1) from an earthquake in the Russia-China border region. The differences in record appearance depending on the response characteristic of the seismograph and the time resolution of the record are striking.

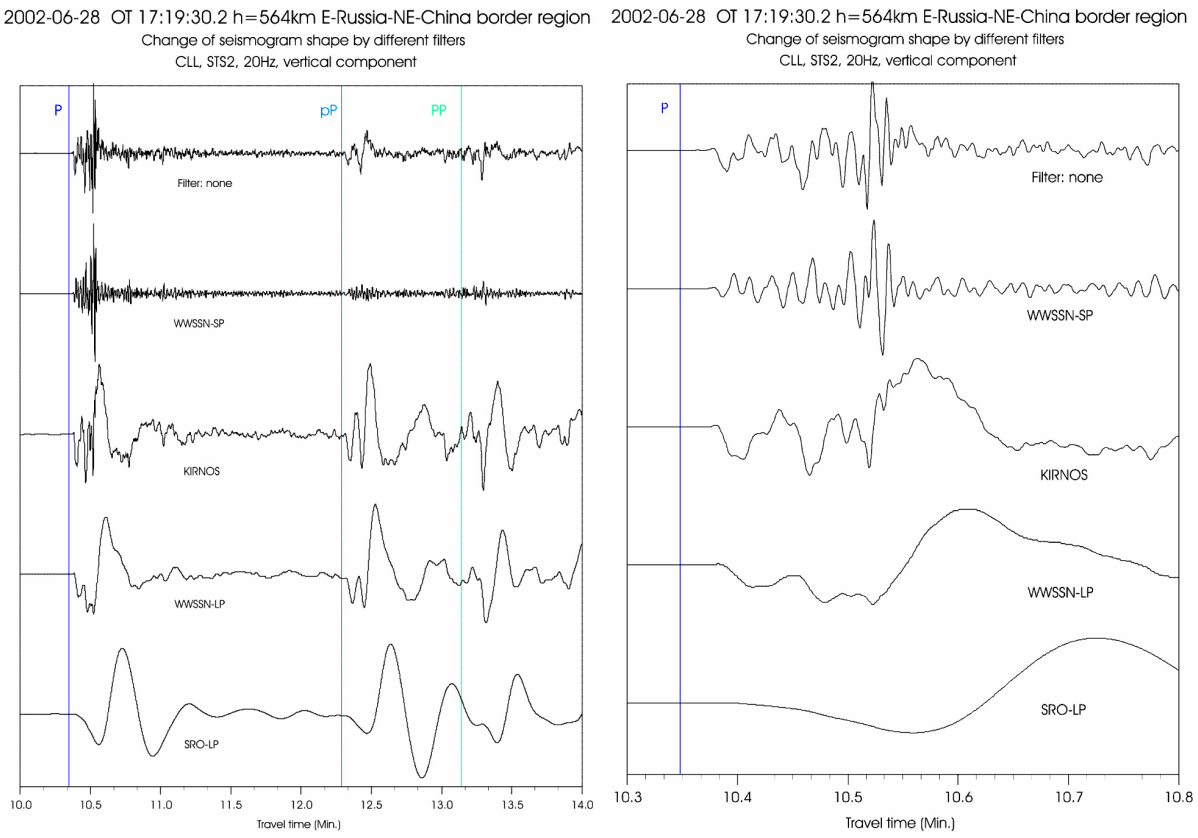

Fig. 4.18 Record segments from an earthquake at the Russia-China border of 4 min (left) and 30 s duration (right). Uppermost traces: unfiltered STS2 velocity broadband seismogram; other traces: filtered records which simulate the seismograms of standard recordings of type WWSSN-SP, Kirnos, WWSSN-LP and SRO-LP (courtesy of S. Wendt, 2002).

Fig. 4.19 gives an example from a simulation of seismometer response to a monochromatic harmonic ground motion w(t) of frequency 1 Hz as input. It has been compiled from two different snapshots of an interactive web site demonstration of the Technical University of Clausthal, Germany, which is no longer available. Trace a) has been recorded with a seismo-

meter of eigenperiod T_s = 1 Hz and damping D_s = 0.2 (i.e., resonance at 1 Hz!) while for trace b) T_s = 20 s and D_s = 0.707. In the first record the transient response takes about 3 s before the steady-state level of constant amplitudes corresponding to the amplitude response of the seismometer and the constant phase shift of about 110° have been reached (after the 6th half cycle). In record b) the transient response takes less than half a second and the seismometer mass follows the ground motion with practically no phase shift. Although the transient response of the 20 s long-period seismometer is much longer than that of the 1 s short-period seismometer, it is not excited here because the signal has very little energy at the eigenperiod.

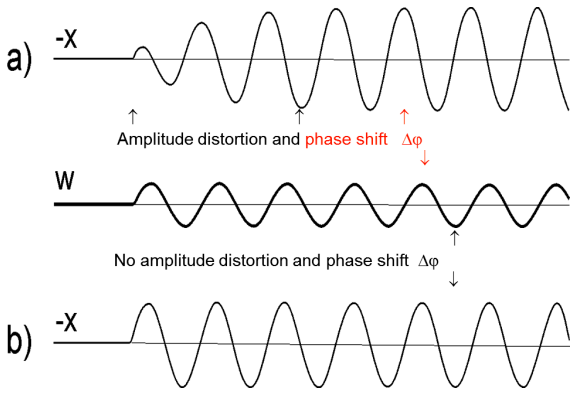

Fig. 4.19 Simulation of displacement signal output x(t) (= relative displacement of the seismometer mass) of a spring-mass pendulum seismometer responding to a monochromatic harmonic ground motion w(t) of period T = 1 s (thick line in the middle). a) Displacement output of a seismometer with low damping (Ds = 0.2) and eigenperiod T_s = 1 s (i.e., resonance); b) Displacement output of a long-period and normally damped seismometer (T_s = 20 s; D_s = 0.707). For discussion see text.

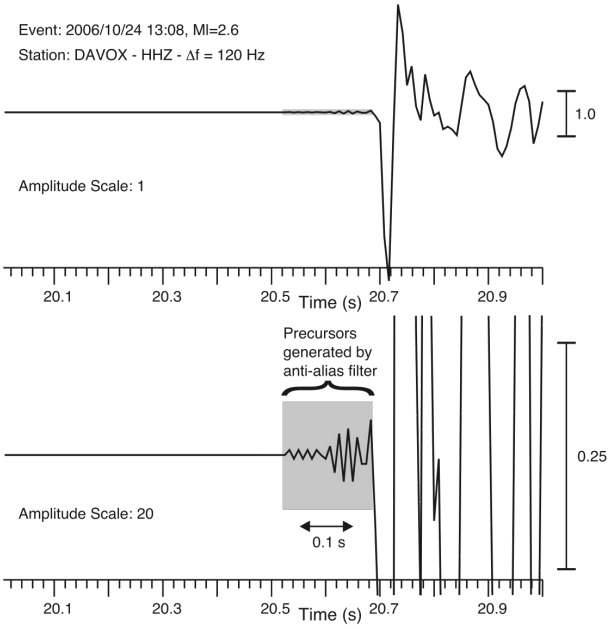

Fig. 4.20 Precursors caused by acausal anti-alias filtering observed on the broadband registration of a local earthquake near Davos, Switzerland (2006/10/24 13:08, Ml = 2.6). Sampling frequency is 120 Hz. The precursors become obvious when enlarging the amplitude scale (lower trace). (Copy of Figure 7 in IS 11.4; courtesy of Diehl et al., 2012)

Seismographs are real physical, i.e., causal filters. They respond to analog input signals with unavoidable phase shifts during the transient response time. Digital filters, however, can be designed in a way that they do not produce phase shifts (Scherbaum, 2007; NMSOP Chapter 6). Such systems implement acausal digital anti-alias filters with symmetrical zero-phase shift impulse responses. As a consequence, the onset of impulsive signals (also of signals with frequency close to the Nyquist frequency) may be obscured by artifact precursory oscillations and their true onset becomes difficult, if not impossible, to determine. Fig. 4.20 shows an example. As outlined in IS 11.4, this effect can in principle be minimized by an inverse filtering process, described e.g. in Scherbaum (2001 and 2007). However, this is a nontrivial procedure that requires knowledge of the original anti-alias filter coefficients. Especially for large and inhomogeneous data sets, compiling the correct information can be rather difficult or even impossible.

4.6 Characteristics and sources of seismic noise

4.6.1 Ocean microseisms

Most of the early 20th century seismographs by Wiechert, Mainka, Galizyn, Bosch-Omori, Milne-Shaw and others were medium-period broadband systems. The more sensitive ones with 100 to 500 times magnification were already able to record the ever-present ground motions with peak amplitudes around 6 s which constitute the background noise for any seismic measurement. They were termed microseisms. Such recordings were first reported by Algue in 1900. Wiechert (1904) proposed at the second international seismological conference that these microseisms are caused by ocean waves on coasts. Later it was found that one must discriminate between: a) the smaller primary ocean microseisms with periods between 10 and 20 s, typically around 14 ± 2 s and b) the secondary or *double frequency microseism* which is related to the main noise peak around 6 ± 2s (see Fig. 4.3, Fig. 4.4, and Fig. 4.5).

Primary ocean microseisms are generated only in shallow waters in coastal regions. Here the wave energy can be converted directly into seismic energy either through vertical pressure variations, or by the smashing surf on the shores, which have the same period as the water waves (T ≈ 10 to 16 s). Haubrich et al. (1963) compared the spectra of microseisms and of swell at the beaches and could demonstrate a close relationship between the two data sets. Energy is transferred between ocean waves and seismic waves through non-linear interaction of ocean waves and bathymetry (Hasselmann, 1963). Measurements from instruments in coastal regions show spectral peaks that track ocean wave frequencies incident at the coast, although this energy decays rapidly inland (Haubrich and McCamy, 1969). The peak is also called the single-frequency peak because it mimics swell frequencies. In the center of continents or of an ocean basin, the single-frequency peak is related to storm waves on remote coastlines (Cessaro, 1994). The relative stability in amplitude for continental sites around the globe suggests persistent, stable sources. Holcomb (1998) also reports on a persistent peak of unknown origin in the noise spectrum at 26 s period. The signals are largest during the southern winters and the amplitude of the peak is correlated between sites worldwide.

Contrary to the primary ocean microseisms, the secondary ocean microseisms could be explained by Longuet-Higgins (1950) and Hasselmann (1963) as being generated by the superposition of ocean waves of equal period traveling in opposite directions, thus generating standing gravity waves of half the period. These standing waves cause non-linear pressure

perturbations that propagate without attenuation to the ocean bottom and couple there into an elastic wave of much larger wavelength and higher phase velocity if the propagation directions are nearly opposite. The area of interference X may be off-shore where the forward propagating waves, generated by a low-pressure area L, superpose with the waves traveling back after being reflected from the coast (Fig. 4.21b). But it may also be in the deep ocean when the waves, excited earlier on the front side of the low-pressure zone, interfere later with the waves generated on the back-side of the propagating cyclone. Microseisms are mostly recorded with periods between 5 and 9 sec and are the result of energetic ocean waves between 10 and 18 sec period. Horizontal and vertical noise amplitudes of marine microseisms are similar. The particle motion is dominatingly of Rayleigh-wave type, i.e., elliptical polarization of the particle motion in the vertical propagation plane. But some energy is present also as body waves, and heterogeneous Earth structure couples some energy into Love waves.

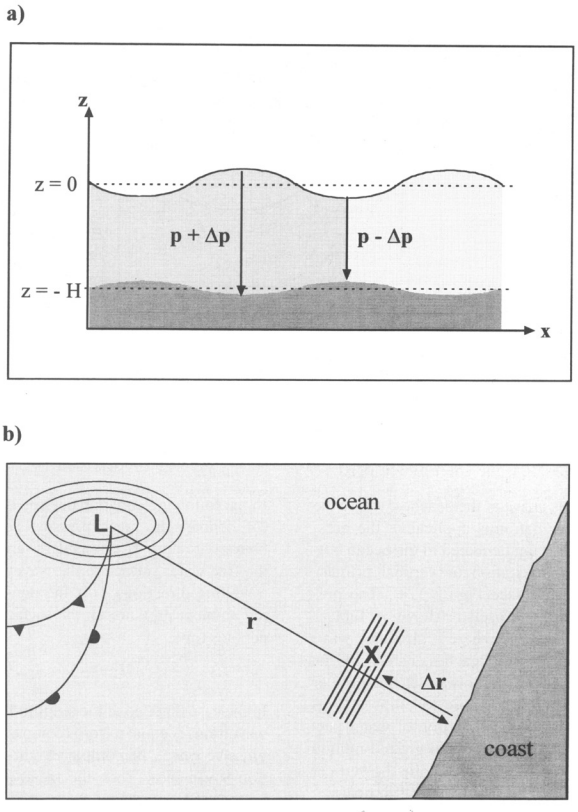

Fig. 4.21 Schemes for the generation of a) primary and b) secondary microseisms (for explanations see text). L – cyclone low-pressure area, X – area of interference where standing waves with half the period of ocean waves develop (reproduced from Journal of Seismology, 2, 1, 1998, "Ocean-generated microseismic noise located with the Gräfenberg array"; Friedrich, Krüger & Klinge, p. 62, Fig. 12; © Kluwer Academic Publishers, with permission of Kluwer Academic Publishers).

Medium-period ocean/sea microseisms experience low attenuation. They may therefore propagate hundreds of km inland. Since they are generated in relatively localized source areas, they have, when looked at from afar, despite the inherent randomness of the source process, a rather well developed coherent part, at least in the most energetic and prominent component. This allows one to locate the source areas and track their movement by means of seismic arrays (e.g., Cessaro, 1994; Friedrich et al., 1998; Fig. 4.22). This possibility has already been used decades ago by some countries, e.g., in India, for tracking approaching monsoons with

seismic networks under the auspices of the Indian Meteorological Survey, although Cessaro (1994) showed that the primary and secondary microseism source locations do not follow the storm trajectories directly. While near-shore areas may be the source of both primary and secondary microseisms, the pelagic sources of secondary microseisms meander within the synoptic region of peak storm wave activity.

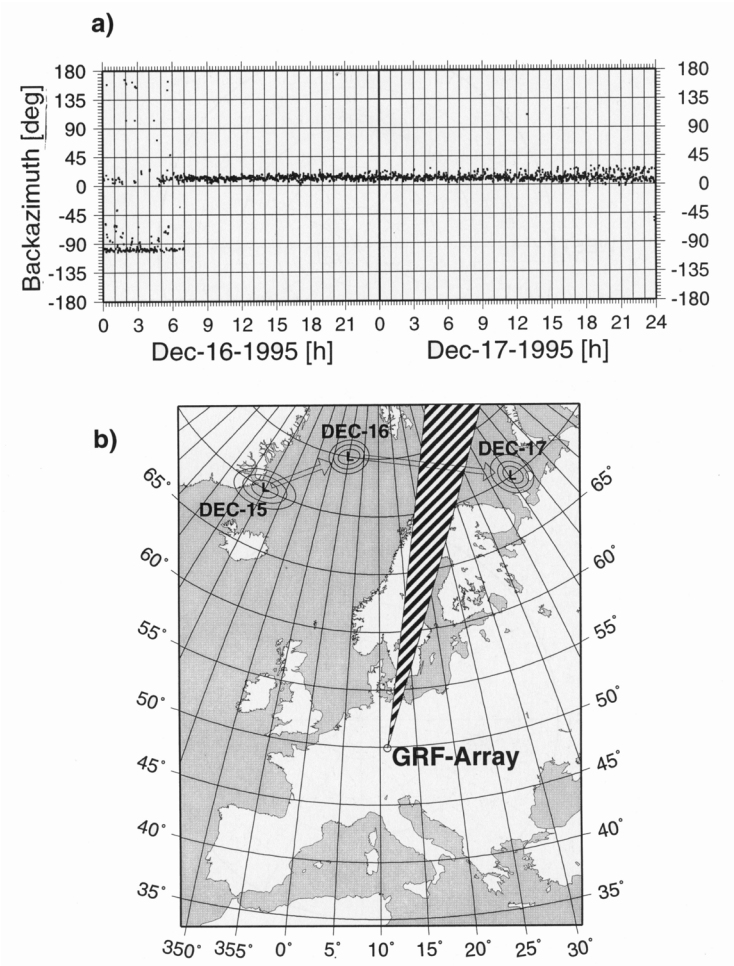

Fig. 4.22 An example of good spatial coherence of medium-period secondary ocean microseisms at a longer distance from the source area which, in this case, allows rather reliable determinations of the backazimuth of the source area by f-k analysis with seismic arrays (see Chapter 9). Figure a) above shows how the backazimuth determination changed from one day to the next, while b) shows the location of the two storm areas and the seismic array. Observations by at least two arrays permit localization and tracking of the noise-generating low-pressure areas (reproduced from Journal of Seismology, 2, 1, 1998, "Ocean-generated microseismic noise located with the Gräfenberg array"; Friedrich, Krüger & Klinge, p. 55, Fig. 7; © Kluwer Academic Publishers, with permission of Kluwer Academic Publishers).

Note that the noise peak of secondary microseisms has a shorter period when generated in shallower inland seas or lakes (T ≈ 2 to 4 s) instead of in deep oceans. Also, off-shore interference patterns largely depend on coastal geometries and the latter may allow the development of internal resonance phenomena in bays, fjords or channels (see Fig. 4.23) which affect the fine spectrum of microseisms. In fact, certain coastlines may be distinguished by unique "spectral fingerprints" of microseisms.

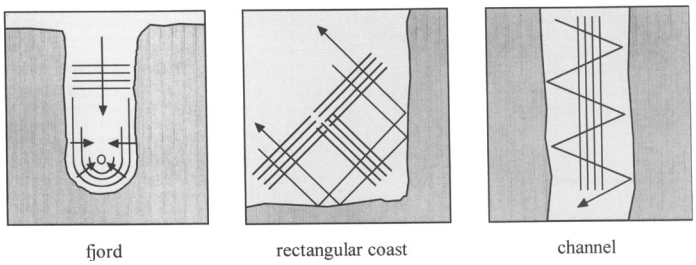

Fig. 4.23 Examples for coastline geometries that provide suitable interference conditions for the generation of secondary microseisms (reproduced from Journal of Seismology, 2, 1, 1998, "Ocean-generated microseismic noise located with the Gräfenberg array"; Friedrich, Krüger & Klinge, p. 63, Fig. 13; © Kluwer Academic Publishers, with permission of Kluwer Academic Publishers).

4.6.2 Noise at the seabottom

4.6.2.1 Broadband noise

The microseism mechanism dominates sea floor noise up to frequencies of a few hertz. At slightly higher frequencies (5-10Hz), short-period noise associated with breaking waves may become important (McCreery et al., 1993). While there is little difference in the microseism band between land and the sea floor at longer periods the major difference occurs at frequencies near 1 Hz. Almost always there is much more noise energy around 1 Hz on the ocean floor than on land, often by more than 40 dB (see subsection 4.6.2.2 on short-period ocean noise below). This huge difference has a profound effect on the relative detection thresholds for short-period teleseismic arrivals in these two different recording environments, which is usually much inferior on the ocean floor. For more details on regional/local differences see Webb (2002).

In recent years more and more ocean-bottom seismographs (OBS; see main section 7.5 in-Chapter 7 and Havskov and Alguacil) have been deployed in order to overcome the inhomogeneous distribution of land-based seismic stations. But permanent OBS installations are still rare. Generally, the noise level at the ocean bottom, even in deep seas, is higher than that on land (by about 10 to 30 dB) and increases with higher frequencies (e.g., Bradner and Dodds, 1964; Webb, 2002, and Fig. 7.85 in Chapter 7). It can be reduced by installing the OBS in boreholes (see Fig. 4.24). The analogues of wind and air pressure generated noise on the Earth surface are on the ocean floor the ocean currents. According to Webb (1988) they also set up a turbulent boundary layer with advecting pressure fluctuations. However, on the ocean floor the deformation signal decays already completely within a few meters depth below the sea floor because much lower velocities and hence much shorter wavelengths are associated with ocean currents than with wind.

On the ocean bottom, as on land, the secondary microseism noise peak between 0.1 and 1 Hz dominates. Background noise levels in this frequency range tend to be higher in the Pacific than in the Atlantic because of its larger size and its general weather conditions (see Fig. 4.25 below and Figure 2 in Webb, 2002). While short-period body-wave arrivals around 1 Hz have been clearly recorded during calm-weather periods by OBSs in the North Atlantic, even at teleseismic distances, they are recognizable in OBS records in the Pacific only for very large events at distances of less than a few tens of degrees. On the other hand, long-period P, S and

surface waves are consistently well recorded by OBSs in the noise minimum between about 0.03 and 0.08 Hz for magnitudes 6 ± 0.3 even at distances D > 100° (Blackman et al., 1995). However, because of the generally inferior recording conditions broadband seismic observations from the sea floor remain rare. The primary motivation for installing stations on the sea floor has been to improve the global ray path coverage for tomographic studies of the Earth and for regional studies of seismicity and structure. Yet, significant improvements in global detection thresholds will only be obtained near the sea-floor stations itself. For some significant results see section 7.5.3 of Chapter 7.

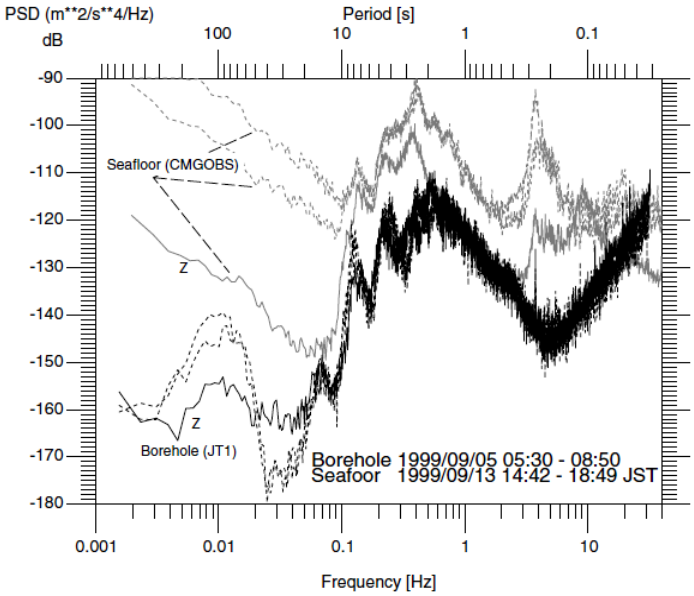

Fig. 4.24 Difference of typical noise power spectra in a borehole installation and a seafloor installation near the borehole of site JT1 (see Fig. 7.80 in Chapter 7). The seafloor observation is noisier than that in the borehole and the horizontal components are much noisier than the vertical (Z) components (after Araki et al., 2004; Figure copied from Fig. 7.71 in Chapter 7; with permission of M. Shinohara, 2013).

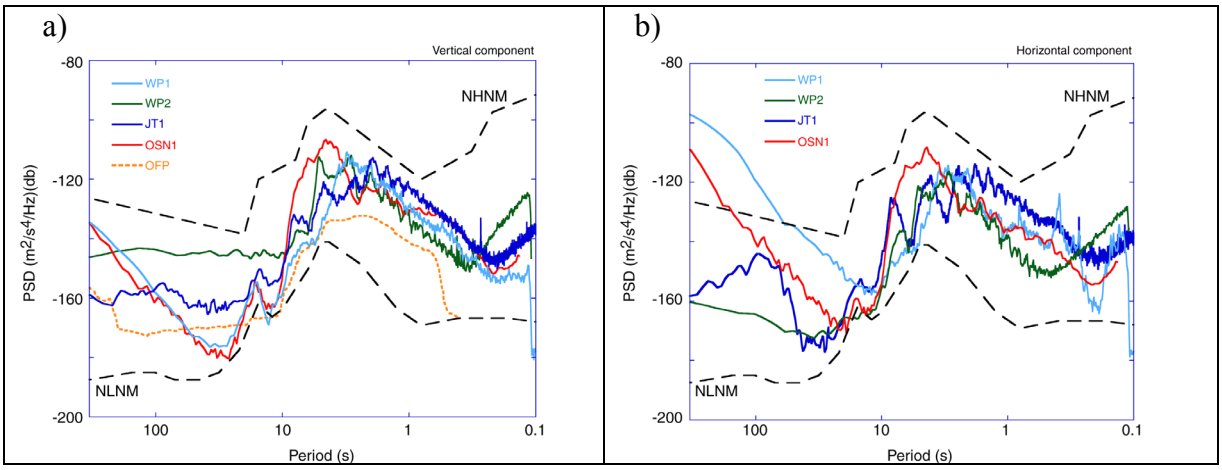

Fig. 4.25 Comparison of ambient seismic noises from seafloor borehole installations: a) for vertical component; b) for horizontal component. WP-1, WP-2 and JT-1 denote observatories in the western Pacific, OSN-1 an observatory off Hawaii (Stephen et al., 1999), and OFP an observatory in the North Atlantic Ocean (Montagner et al., 1994). NHNM and NLNM indicate the Peterson (1993) New High Noise Model and New Low Noise Model, respectively. (Figure copied from Fig. 7.72 in Chapter 7; with kind permission of M. Shinohara, 2013).

According to Webb (1998), horizontal component noise levels on sea-floor sensors can be as much as 60 dB higher than vertical component noise levels at periods near 100 s due to tilt (e.g., site WP1 in Fig. 4.25). Tilt noise will appear on vertical component records as well if the vertical component sensor is not very precisely oriented with the true plume line. Most vertical component records from the sea floor show evidence of tilt noise due to currents which can be rather strong and thus the records very noisy on shallow-water sites (Romanowicz et al., 1998). However, because of the short wavelengths associated with pressure fluctuations due to ocean-floor currents burial of the sensors just a few meters below the ground will already strongly reduce (up to about 60 dB) the long-period horizontal component noise levels (Webb, 1998). But incomplete burial allowing for convection of sea water in the borehole may deteriorate this positive effect (Beauduin and Montagner, 1996; Vernon et al., 1998). Webb and Crawford (1999) show that sea floor pressure data can be used to remove most of the infragravity wave deformation signal from vertical component OBS data in the band from 0.001 to 0.04 Hz. Improvements of 10-20 dB in SNR for long-period surface waves could thus be achieved at sea-floor stations in the Pacific. For more information about noise and signal recording conditions and installation requirements in an ocean bottom environment see main section 7.5 in Chapter 7 and Webb (2002).

4.6.2.2 Short-period noise (0.5-50 Hz)

Webb (2002) gives a rather detailed overview of the mechanisms which generate short-period noise on the sea floor and how this noise decays with depth below the sea floor. Here we summarize only some of the most interesting facts and give related references for further reading.

The sea floor in the band from 0.5 to 5Hz is almost invariably noisier than the typical land site because of microseisms generated by small-amplitude, high-frequency ocean waves that can be produced already by light winds. Such locally generated microseisms maintain for most of the time sea-floor noise levels some 40 dB above land sites. These noise levels "saturate" with little increase above a frequency-dependent saturation wind velocity, which is near 1 Hz about 5 m/s (McCreery et al., 1993). During long intervals of calm winds, however, these noise levels may fall by 20 dB or more (Webb, 1998; Wilcock et al., 1999). Because wind speeds exceed 5 m/s over most sites in the oceans for most of the time, the average sea-floor sites are usually rather noisy near 1 Hz. A notable exception is the Arctic Ocean during winter when the ice cap prevents the excitation of the ocean waves on the surface. Parts of the North Atlantic and Indian oceans can also experience long intervals of near calm conditions during the summer months and may provide quiet sites for detection of short-period body waves (Webb, 1998). In contrast, most sites in the Pacific seem to be noisy most of the time (McCreery et al., 1993).

Installing seismometers within sea-floor boreholes will not necessarily reduce this microseism noise level because the energy is coupled from ocean waves into acoustic waves and then into Rayleigh-wave modes below the sea bed which penetrate down to depths of several kilometres. This is beyond the present range of ocean drilling. However, at shallow depths some SNR improvement is expected because microseisms are scattered by bathymetry and topography at the sediment-basement interface producing short-wavelengths Stoneley shear modes. Their amplitudest decay below the sea floor rapidly with frequency and depth (Bradley et al.,

1997). But signal levels at depth are also smaller (because of changing impedance). Therefore the resulting improvement in signal-to-noise ratio is near zero at 0.2 Hz, but it increases to more than 10 dB at 5Hz. Correlation lengths for this type of ocean bottom noise at frequencies above 0.4 Hz, measured between elements of a small-aperture array of OBS, were between 100 and 200 m only (Schreiner and Dorman, 1990).

More high-frequency noise (5-50Hz) on the sea floor tends to be associated with man-made (cultural) sources. A good review of "low-frequency acoustic noise" (< 100Hz), e.g., radiated by marine mammals, can be found in Richardson et al. (1995). While noise frequencies between 5-10 Hz are dominatingly wind-generated and caused by wave breaking, most of the cultural ocean noise is more high-frequency and caused by ship traffic (cavitation of propellers and noise from vibration of machinery). Distinct lines associated with generators (50 or 60Hz) or with other machinery (motors, generators, thrusters and pumps, etc.) also make up much of the shipping noise, with noise levels peaking between 10 and 100 Hz. The lowest-frequency components are associated with the rotation of propellers. Large ships such as supertankers produce sharp spectral lines at frequencies of 7 Hz or lower but with many higher harmonics (Richardson et al., 1995). Areas near high-traffic ship routes can be 20-25 dB noisier than regions remote from shipping. Other sources of cultural noise observed on the ocean floor in the seismic band include active seismic sources (airguns) and offshore drilling (Richardson et al., 1995).

For some locations large whales are another natural noise source. Blue and fin whales produce very loud calls at frequencies as low as 16 Hz. They are easily seen locally on sea-floor seismometer records. In some special locations whale calls can be so frequent as to interfere with active source seismic experiments. Also the movement of ice in the polar regions may be a natural noise source in Arctic and Antarctic waters (Richardson et al., 1995).

Most favourable for high-frequency seismic observations is the transition band (5-10Hz), above the microseisms and below the typical shipping noise. It provides relatively quiet conditions that allow the detection of oceanic Pn and Sn phases (also known as Po and So) from moderate magnitude oceanic events to great distances (Butler et al., 1987).

4.6.3 Seismic noise on land

4.6.3.1 Long-period noise

Ground noise on land at very long period (0.2 to 50 mHz) is usually associated with atmospheric pressure fluctuations. At these very low frequencies, vertical component seismometers react to changes in gravity as the mass of the atmosphere above a site changes with atmospheric pressure. At higher frequencies, the ground deforms under the fluctuating pressures associated with turbulence in the boundary layer of the atmosphere (Murphy and Savino, 1975). If seismometers that are not fully sealed they may also experience apparent accelerations due to buoyancy effects on the seismometer mass, and pressure fluctuations may cause long-period horizontal component noise by distorting the case of the seismometer or the walls of the vault (Savino et al., 1972). Long-period seismometers are also sensitive to temperature changes. Therefore, careful installations aim at sealing the sensor from both pressure and temperature fluctuations (see IS 5.4). Zürn and Widmer (1995) showed that vertical component noise levels between 0.2 and 1.7 mHz can be reduced by more than 10 dB by subtracting

the scaled, locally recorded pressure signal from the vertical acceleration record, thereby improving the SNR for normal mode observations (see also Beauduin et al. 1996 and Fig. 4.26).

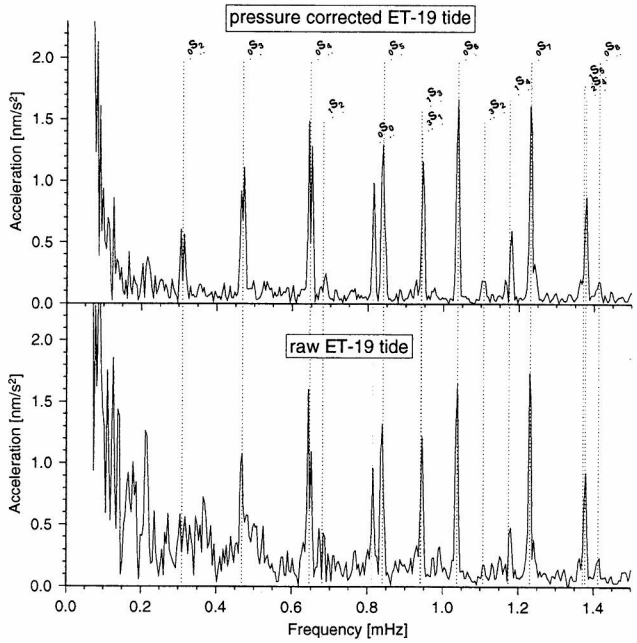

Fig. 4.26 Linear acceleration amplitude spectra of LaCoste-Romberg Earth tide gravimeter ET-19 records at the BFO observatory in SW Germany after the big Shikotan earthquake of October 4, 1994. Bottom: raw data; Top: barometric-pressure corrected data. Copy of Figure 1 in Zürn and Widmer (1995): On noise reduction in vertical seismic records below 2 mHz using barometric pressure. Geophys. Res. Lett, 22(24), 3537-3540; © American Geophysical Union.

Turbulence in the atmospheric boundary layer produces pressure fluctuations at the Earth's surface that cause significant deformation to depths of a few tens of meters below the surface. This noise source is a primary reason why broadband seismometers at permanent stations are often installed beneath the Earth's surface in shallow boreholes (see section 7.4.5 and Fig. 7.59 in Chapter 7). For instruments on the surface, short-wavelength atmospheric pressure fluctuations produce a large tilt signal that makes the horizontal components particularly noisy. Horizontal noise power may then become significantly larger than vertical noise power. Tilt couples gravity into the horizontal components but much less into the vertical component (see Chapter 5, section 5.3.3 and Figs. 5.8 and 5.9). The ratio increases with the period and may reach a factor of up to 300 (about 50 dB). Therefore a site can be considered as still favorable when the horizontal noise at 100 to 300 s is still within 20 dB above the vertical component noise power, as in Fig. 4.27. Horizontal component noise is mainly due to local tilt, which may also be caused by traffic and wind pressure. At very long periods, deformation of the ground, the seismometer vault, or the building due to insolation gradients (uneven heating by the sunshine) may become noticeable. Generally, recording sites poorly coupled to the ground or on poorly consolidated ground will tend to be noisy, both at long and short periods. Other reasons for increased long-period noise may be air circulation in the seismometer vault or underneath the sensor cover. Special care in seismometer installation and shielding is therefore required in order to reduce drifts and long-period environmental noise (see Chapters 5 and 7 as well as IS 5.4).

For more details also on the causes and phenomena of long-period noise see Webb (2002).

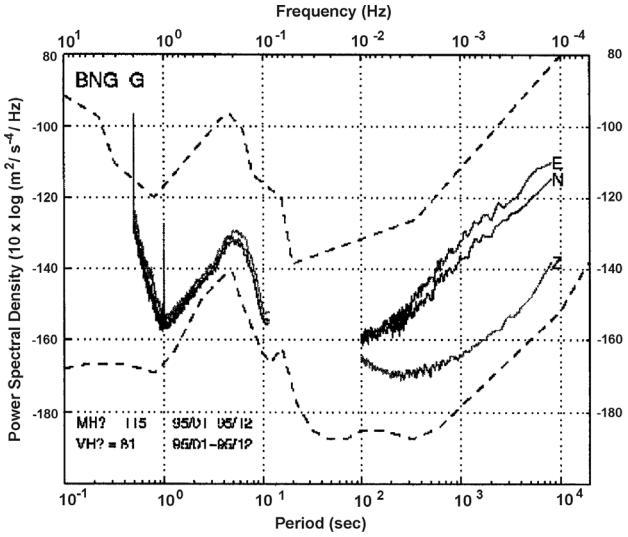

Fig. 4.27 Seismic noise at the station BNG (Bangui, Central Africa) as compared to the new global seismic noise model by Peterson (1963) (from the FDSN Station Book, http://www.fdsn.org/station_book/G/BNG/bng.g_allyr.gif). The upper and lower broken curves denote the NHNM and NLNM noise models according to Peterson (1993).

4.6.3.2 Short-period noise (0.5 to 50 Hz)

Short-period seismic noise may have natural causes such as wind (wind friction over rough terrain; trees and other vegetation or built-up objects swinging or vibrating in the wind), rushing waters (waterfalls or rapids in rivers and creeks) etc. Wind-generated noise is broadband, ranging from about 0.5 Hz up to about 15 to 60 Hz (Young et al., 1996). But the dominant sources of high-frequency noise are man-made (power plants, factories, rotating or hammering machinery, road and rail traffic, etc.; see sections 7.1 and 7.2 in Chapter 7.) and often referred to as *cultural noise*. Wind-generated noise couples mostly into surface-wave modes, cultural noise, however, couples at least partly into body waves that can propagate also to greater depth (Carter et al., 1991). Cultural noise is in principle avoidable, although it is often impractical to place seismic station sites at sufficient distances away from cities or highways. Some rules of thumb suggest that it may be necessary to site short-period recording stations as far as 25 km from power plants or rock-crushing machinery, 15 km from railways, 6 km from highways, and a kilometer or more from smaller roads. And with respect to moving waters it is recommended to place stations away from moving water between some 60 km for very large waterfalls and dams to 15 km for smaller rapids (see Willmore, 1979 and Tab. 7.5 in Chapter 7). However, noise travels further across competent rock than through alluvial filled valleys. Therefore, "safe" distances may be from 1/2 to 2/3 of the values above, depending on propagation path (Willmore, 1979).

Most of the short-period natural and man-made sources are distributed, stationary or moving. Their contributions, coming from various directions, superpose to a rather complex, more or less stationary random noise field. The particle motion of short-period noise is therefore more erratic than for long-period ocean noise. Nevertheless, polarization analysis, averaged over moving time-windows, sometimes reveals preferred azimuths of the main axis of horizontal

particle motion hinting at localized noise sources. Also the vertical component is clearly developed and averaged particle motion in 3-component records indicates fundamental Rayleigh-wave type polarization. A rather popular and cost-effective microzonation method is based on this assumption. It derives information about the fundamental resonant frequency of the soft-soil cover and estimates local site amplification of ground motion from the peak in the horizontal to vertical component spectral noise ratio (H/V *Nakamura method*; e.g., Nakamura, 1989; Bard, 1999; Parolai et al., 2001 and 2002; Chapter 14).

According to the above, every recording site has different noise characteristics depending on its distance from the ocean, industrial and settlement areas, major infrastructure facilities, the wind climate of the site and the depth of burial of the sensor. At some locations a seasonal cycle is evident due to variations in wind, or water flow in nearby rivers. E.g., according to Fyen (1990), spring runoff raises noise levels by up to 15 dB between 0.5 and 15 Hz at the NORESS array. In settlement and industrial areas a diurnal cycle may dominate due to variable human activity during the day.

High-frequency noise spectra on land during quiet intervals resemble each other at quieter sites. The rather featureless displacement power spectrum follows a power-law dependence in frequency, proportional to $\approx f^{-2}$ (see Fig. 4.28 and Bungum et al., 1985). This spectral appearance changes drastically due to the strong impact of cultural noise, especially in the frequency band between 1 and 10 Hz (see Fig. 4.31). Wind noise depends on the strength of the wind and the character of the site. Recorded noise power near 1 Hz in a surface vault may increase by 10-20 dB, as compared to records on calm days, when wind speed reaches about 5 m/s. According to Withers et al. (1996) short-period wind noise becomes detectable in records at surface sites far from cultural sources at wind velocities above about 3 m/s and at 4 m/s for subsurface sensors as well (see Fig. 4.29). The primary mechanism by which wind couples into high- frequency noise is probably by the direct action of the wind on trees, bushes, and other structures, although at lower frequency the pressure fluctuations associated with wind can directly drive motions of the ground.

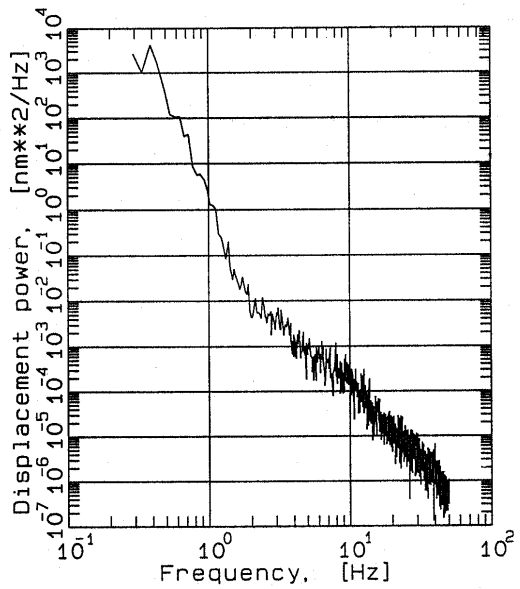

Fig. 4.28 Spectrum of displacement power spectral density calculated from 6 moving, 50% overlapping intervals of short-period noise records, 4096 samples long each, i.e., from a total record length of about 80 s at a rather quiet site in NW Iran.

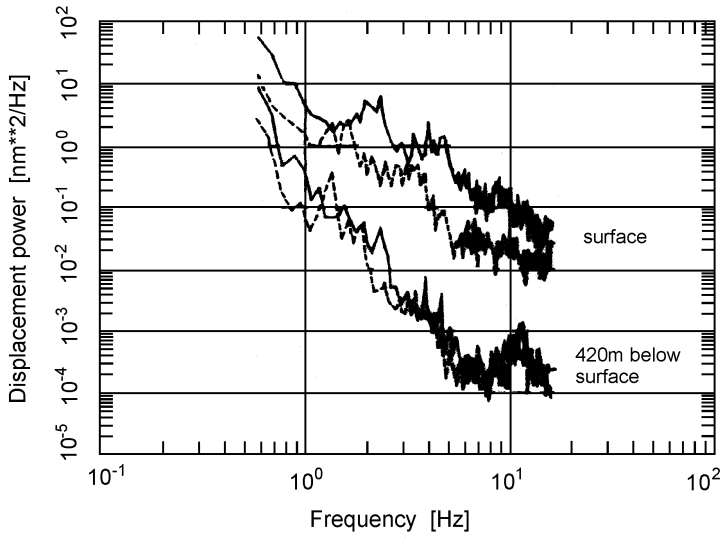

Fig. 4.29 Displacement power noise spectra measured at the surface (upper curves) and at 420 m below the surface in a disused salt mine at Morsleben, Germany (lower curves) on a very quiet day (hatched lines) and on a day with light wind on the surface (wind speed about 4 m/s; full lines).

Cultural noise varies greatly between sites (Fig. 4.34). Noise levels may differ also by 30 dB or even more within a day (e.g., Fig. 4.30 and Fyen, 1990), as well as from day to day. Therefore, it is common to present ensembles of spectra by per-centile ranking to allow discrimination between infrequent very loud sources and more typical background levels (e.g., Bungum et al., 1985). Industrial and traffic noise levels are usually lowest on weekends but increase during holidays because of higher traffic. Sources such as power plants, transformator stations etc. generate narrowband noise, producing energetic spectral lines at 50 or 60 Hz as well as related harmonics and sub-harmonics (e.g., at 30 Hz, 25 Hz, 12.5 Hz) depending on location (Fig. 4.31). The NORESS array data included lines at 6, 12, and 17 Hz due to reciprocating saws in a nearby sawmill (Fyen, 1990), and records at Moxa (MOX) station in Germany have been spoiled over decades by the a pronounced 2 Hz peak due to heavy steam engine driving a steel-press for rails at a distance of 16 km. It may be possible to remove some of such narrowband noise through application of digital or analog filters (see section 4.7). Other types of machinery, however, may also produce narrowband peaks in the noise spectra, but with time-variable frequencies as motor speed may vary. These noise sources are more difficult to remove.

Comparisons of noise spectra from surface vaults and subsurface installations in mines (Fig. 4.29) or boreholes (Fig. 4.32) have repeatedly shown significant improvements in SNR for high-frequency phases recorded at depths, sometimes even as shallow as a few meters (e.g., Aster and Shearer, 1991). The signal-to-noise ratio for high-frequency arrivals can be optimized by choosing sites with a lossy blanket of weathered near-surface material (Withers et al., 1996). Large reductions in noise level may also be seen in the first 5 m between the weathered rock of the surface and the more competent rock in the borehole. Wind noise, however, may couple into open boreholes. Therefore, covering open boreholes can reduce wind noise considerably.

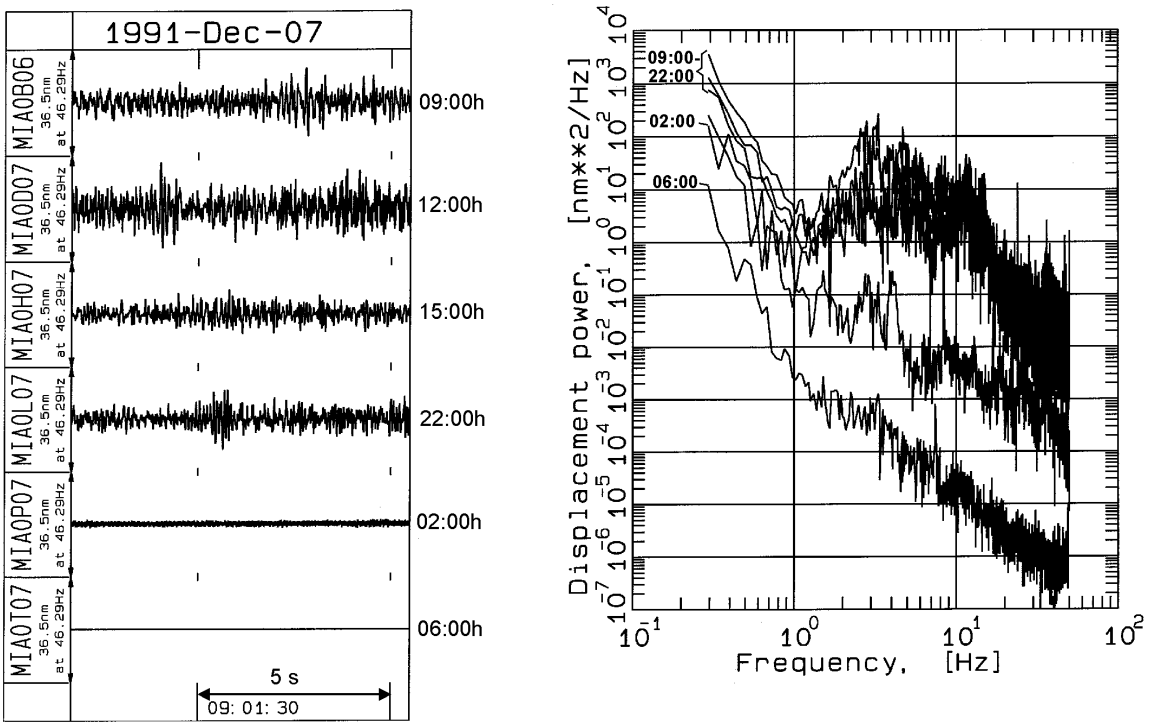

Fig. 4.30 Comparison of relatively quiet sections of vertical component noise records (left; without strong transients) and related power spectra (right) at a reference site in the district capital town of Miane in NW Iran. The measurements were made at different times of the day.

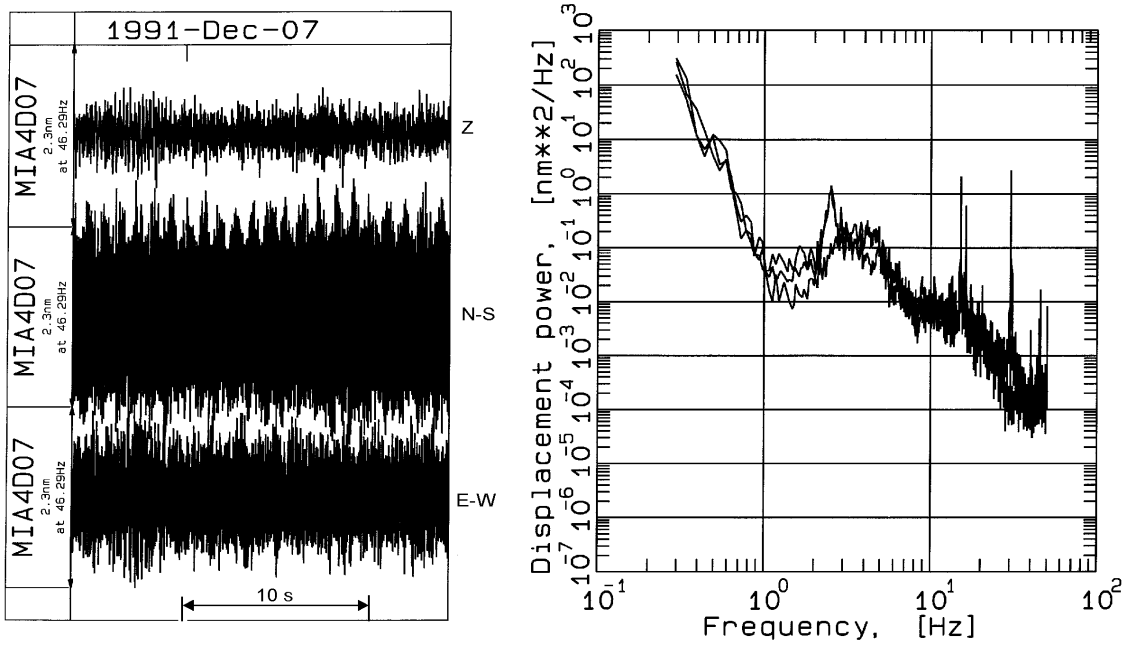

Fig. 4.31 Noise records and related power spectra near to a transformer house and power line. Note the monochromatic spectral lines around 13, 30 and 50-60 Hz, either induced by the AC current frequency and its lower harmonics and/or caused by the vibration of the transformer.

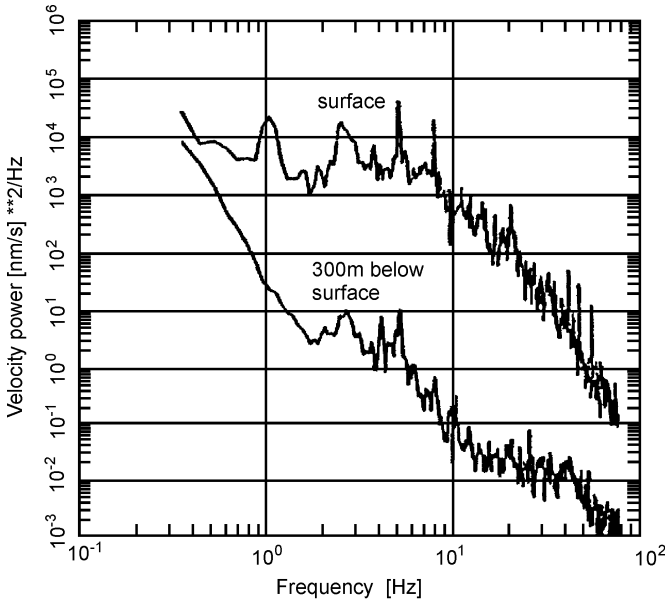

Fig. 4.32 Velocity power density spectra as obtained for noise records at the surface (top) and at 300 m depth in a borehole (below) near Gorleben, Germany (courtesy of M. Henger).

Most comparisons of borehole and vault noise levels show 10-30 dB lower noise levels in the boreholes, with most of the reduction in noise level occurring in the first 100 m (Young et al., 1996). Broadband spectral levels fall also with increasing borehole depth but narrow spectral lines due to cultural sources and or waveguide trapping may show less depth dependence (e.g., Galperin et al., 1978). This is also demonstrated by the very different noise decay with depth in typical 1-Hz records made in two deep boreholes in the US (Fig. 4.40). While in a borehole in Texas the noise amplitudes decreased steadily (up to a factor of 30) down to 3000 m depth below surface, they decreased in another borehole in Oklahoma down to about 2000 m only and then increased again towards larger depth. At this greater depth a layer with 22% lower P-wave velocity was found by means of borehole seismic measurements (noise traveling in a low-velocity layer?).

The surface-wave nature of seismic noise (including ocean noise) is the reason for the exponential decay of noise amplitudes with depth, which is not the case for body waves (Fig. 4.33). Since the penetration depth of surface waves increases with wavelength, high frequency noise attenuates more rapidly with depth. In case of Fig. 4.33 the noise power at 300 m depth in a borehole was reduced, as compared to the surface, by about 10 dB, at f = 0.5 Hz, 20 dB at 1 Hz and 35 dB at 10 Hz. Withers et al. (1996) found that for frequencies between 10 to 20 Hz, the SNR could be improved between 10 to 20 dB and for frequencies between 23 and 55 Hz as much as 20 to 40 dB by deploying a short-period sensor at only 43 m below the surface. But both noise reduction and signal behavior with depth depend also on local geological conditions (see 4.6.5). Because of the surface-wave character of short- and medium-period noise, the horizontal propagation velocity of seismic noise is frequency dependent. It is close to the shear-wave velocity in the uppermost crustal layers, which is about 2.5 to 3.5 km/s for outcropping hard rock and about 300 to 650 m/s for unconsolidated sedimentary cover. This is rather different from the apparent horizontal propagation velocity of P waves and all other steeply emerging teleseismic body-wave onsets.

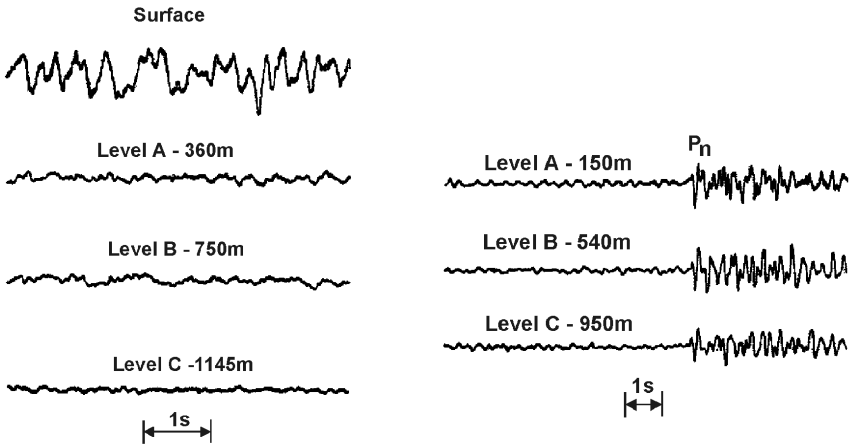

Fig. 4.33 Recording of short-period seismic noise (left) and signals (right) at the surface and at different depth levels of a borehole seismic array. Note the significantly larger Pn amplitude closer to the surface. It is due to the surface amplification effect which may reach a factor of two for vertical incident waves. (Figure copied from Bormann, 1966; modified from Broding et al., 1964).

Signals which have a similar waveform and polarization, so that they can interfere constructively, are termed coherent. This is usually the case for seismic signals generated and radiated by a common source process. The degree of coherence is defined by the ratio between the auto- and the cross-correlation of the time series (the cross-correlation is squared and divided by both autocorrelations, to render the result independent of the signal amplitudes). It may vary between 0 and 1. For seismic noise it shows distinct frequency dependence. Spatial coherence (paragraph 4.2.4) may be rather high for long-period ocean microseisms. Accordingly, the correlation radius, i.e., the longest distance between two seismographs for which the noise recorded in certain spectral ranges is still correlated, increases with the noise period. It may be several km for $f < 1$ Hz but drops to just a few tens of meters or even less for $f > 50$ Hz. For seismic noise, it is usually not larger than a few wavelengths.

Generally, noise levels increase with higher wind speeds. However, there is apparently no linear relationship between wind speed and the amplitude of wind generated noise. Wind noise increases dramatically at wind speeds greater than 3 to 4 m/s and may reach down to several hundred meters depth below the surface at wind speeds > 8 m/s (Young, 1996). But generally, the level and variability of wind noise is much higher at or near the surface and is reduced significantly with depth (Fig. 4.30). Moreover, while for wind speeds below 3 to 4 m/s, one may observe omnidirectional background noise with relatively large coherence length at frequencies below 15 Hz, the coherence length is strongly reduced at higher wind speeds with increased air turbulence and local wind pressure fluctuations (Withers et al., 1996).

Thus, differences in the frequency spectrum, horizontal wave-propagation velocity, degree of coherence and depth dependence between (short- and medium-period) seismic noise and seismic waves allows to improve the signal-to-noise-ratio (SNR) by installing seismic sensors either at reasonable depth below the surface or by way of data processing (see 4.7).

4.6.3.3 Seismic noise in urban environments

In urban, densely populated and industrialized environment both natural and cultural noise components may play a major role in a wide range of frequencies. Measuring and analyzing urban seismic noise (USN) requires broadband recordings and data analysis. Fig. 4.34 compares the noise power density spectrum measured at the former seismological station in the city of Hamburg, Germany, with the spectrum measured on a hard rock site in a quiet Spa village some 70 km apart.

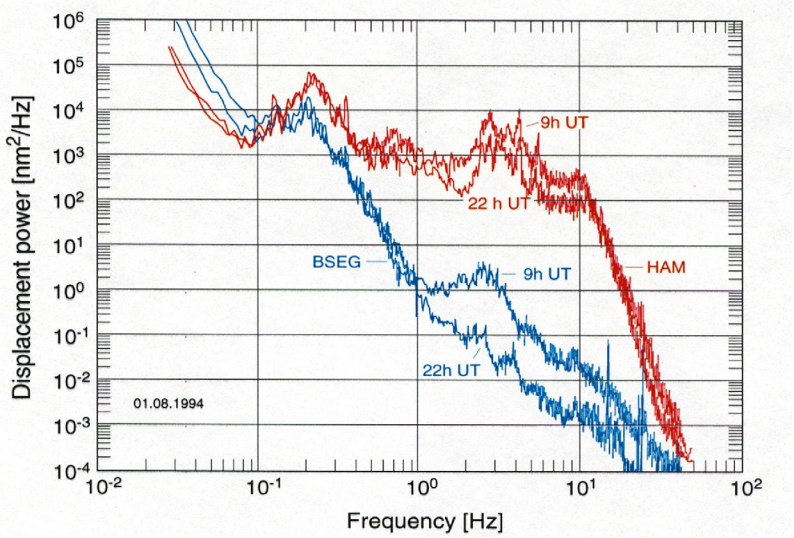

Fig. 4.34 Noise power spectra at HAM (upper two curves, red) and BSEG (lower two curves, blue) determined from vertical-component records on August 1, 1994, at daytime (around 10 a.m. local time) and nighttime (around 11 p.m. local time), respectively (color version of a figure by Bormann et al., 1997).

From Fig. 4.34 the following conclusions can be drawn: While in a remote quiet urban setting the seismic noise spectrum may decay at night almost monotonously towards higher frequencies the cultural noise activity may increase the daytime PSD for frequencies above 1 Hz by some 10 dB. In contrast, in a very busy industrialized city such as Hamburg, the seismic noise level may be 20 dB to 40 dB higher for frequencies of about 0.5 – 30 Hz and may be reduced during night time by some 2 dB to 10 dB only between 1 Hz and 10 Hz. In the metropolitan city of Berlin the "cultural noise" difference at frequencies exceeding 1 Hz between midday and midnight is nearly constant at 10 dB for all frequencies (see Fig. 7.31 in Chapter 7), but it may be larger at other towns with more pronounced diurnal variability of human and industrial activities.

Groos and Ritter (2009) stated that the generally high variability of USN does not allow to characterize a sample time series of USN comprehensively by single measures such as the standard deviation of a seismic noise series or the PSD at a given frequency. For the metropolitan city of Bucharest, Romania, they calculated long-term spectrograms of up to 28 days duration from broadband seismic recordings. The aim was to identify the frequency-dependent behavior of the time-variable processes that contribute to USN. Based on the spectral analysis of the data in eight frequency ranges between 8 mHz and 45 Hz they proposed a time-domain classification which allows to identify both Gaussian distributed seismic noise time series as well as time series that are dominated by transient or periodic signals due to traffic, rotating machinery etc. Groos and Ritter (2009) found that only 40% of the analyzed time series

are characterized by Gaussian distributed noise and that the most common deviations from a Gaussian distribution are due to large-amplitude transient signals (Fig. 4.35). And most astonishingly, they found significant variations of the statistical noise properties with daytime in the whole frequency range between 0.04 and 45 Hz, i.e., both below and above the microseismic noise peak. This result points to a broadband human influence on USN. The authors recommend to use such automatically derived information from broadband seismic data to select suitable time windows for H/V noise studies (see Chapter 14) or ambient noise tomography.

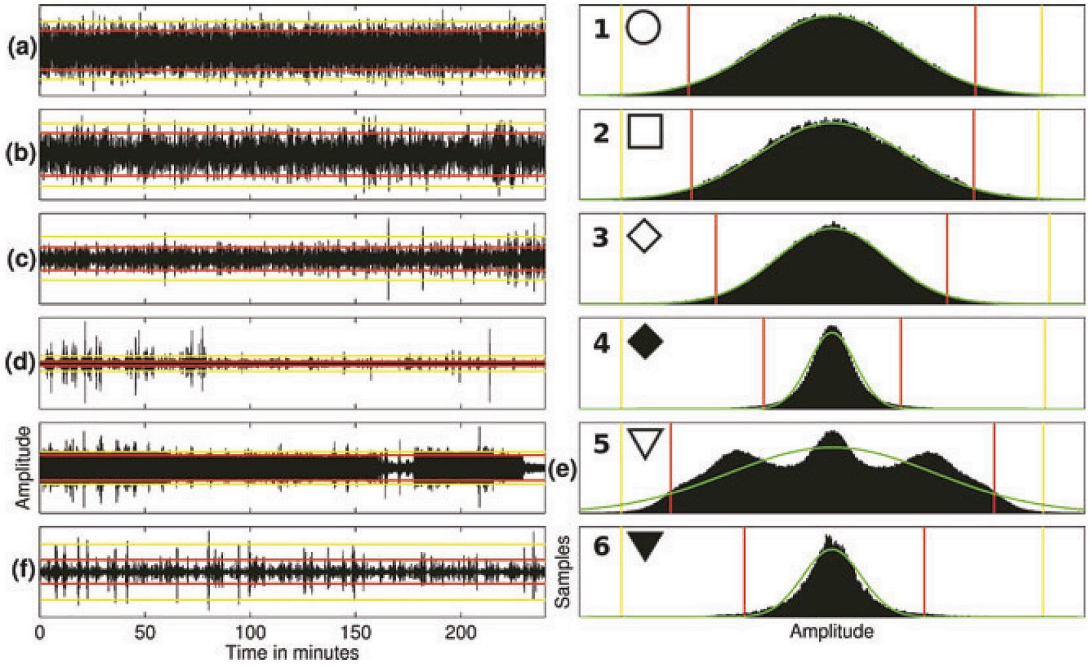

Fig. 4.35 Time series (left-hand panels) and their histograms with the Gaussian distributions (right-hand panels) of vertical-component USN recorded in Bucharest according to Groos and Ritter (2009). Estimated from the mean and the upper boundary of the 68% interval of the corresponding time series. The red and yellow lines in the right-hand panels delimit the 2-sigma and 3-sigma range of the Gaussian distributed time series. Note that the more the time series are dominated by short transient noise signals the more the real amplitude frequency distributions deviate from the respective Gaussian ones. The non-bell shaped multimodal distribution under (e) is due to time series dominated by sinusoidal signals of different dominating frequencies and the asymmetric distribution under (f) is due to the dominance of asymmetric signals in the time series. (Copy of Figure 5 on p. 1220 in Groos and Ritter (2009); © Geophys. J. Int.)

4.6.4 Signal and SNR variations due to local site conditions

Compared to hard rock sites, both noise and signals may be amplified on soft soil cover. This signal amplification may partly or even fully outweigh the higher noise observed on such sites. Signal strength observed for a given event may vary strongly (up to a factor of about 10 to 30) within a given array or station network, even if its aperture is much smaller than the epicentral distance to the event (< 10-20%), so that differences in backazimuth and amplitude-distance relationship are negligible (Fig. 4.36).

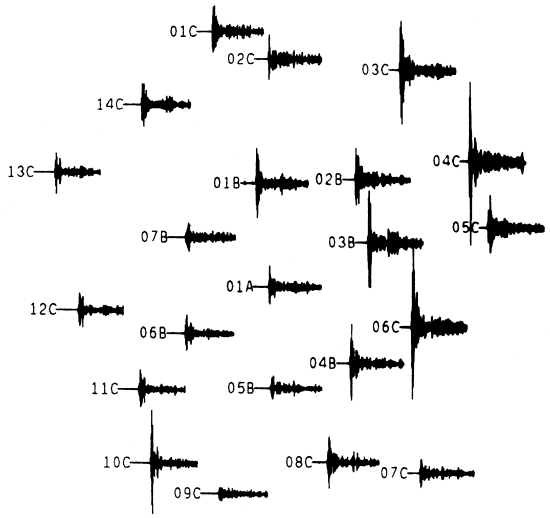

Fig. 4.36 Records of a Semipalatinsk event at stations of the NORSAR seismic array (diameter about 90 km). The event is about 37-38° away. Note the remarkable variations of signal amplitudes by a factor up to 10 (the standard deviation is about a factor of 2) (from Tronrud, 1983a).

Also, while one station of a network may record events rather weakly from a certain source area, the same station may do as well as other stations (or even better) for events from another region, azimuth or distance (e.g., station GWS in Fig. 4.37 left and right, respectively).

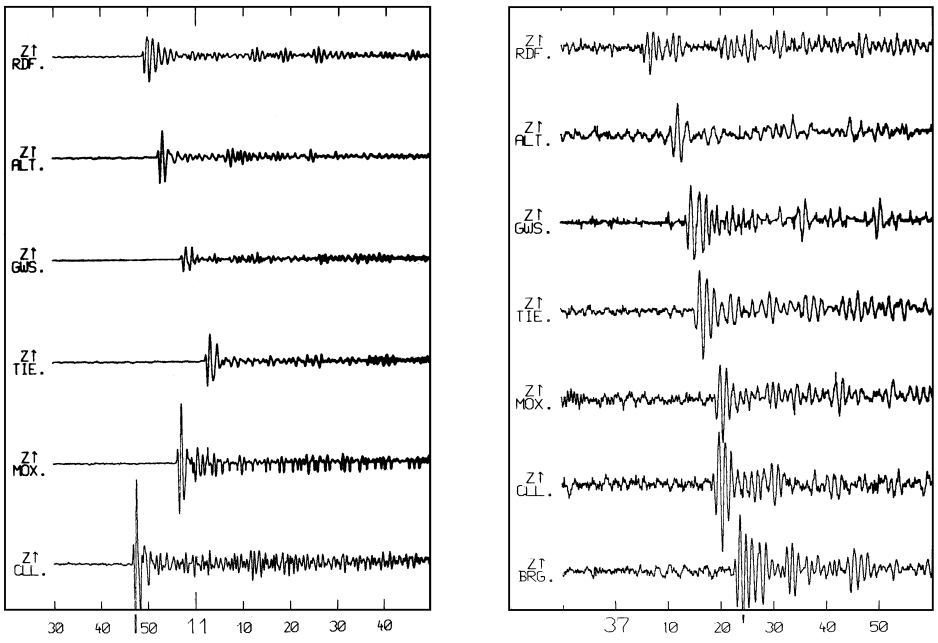

Fig. 4.37 Short-period records of underground nuclear explosions at the test sites of Semipalatinsk (left, D about 41° ± 1°) and Nevada (right; D about 81°± 1°) at stations of the former East German seismic network. Note the differences in signal amplitudes both amongst the stations for a given event and for the same station pairs, when comparing events in different backazimuth and distance. Also, at right, the compressive first motion is lost at several stations in the presence of noise due to the narrowband one-octave recording. Small numbers on the x-axis are seconds, while big numbers are minutes.

Fig. 4.38 compares for regional and teleseismic events the short-period P-wave amplitude ratio (left) and SNR (right) of two stations of the German Regional Seismic Network (GRSN). In the same azimuth range, but at different epicentral distances, station BRG may record both > 3 times larger as well as > 3 times smaller amplitudes than station MOX. This corresponds to magnitude differences up to one unit! The SNR ratio BGR/MOX also varies by a factor of 3 and more, depending on azimuth and distance of events. Therefore, optimal site selection can not be made only on the basis of noise measurements. Also, the signal conditions at possible alternative sites should be compared.

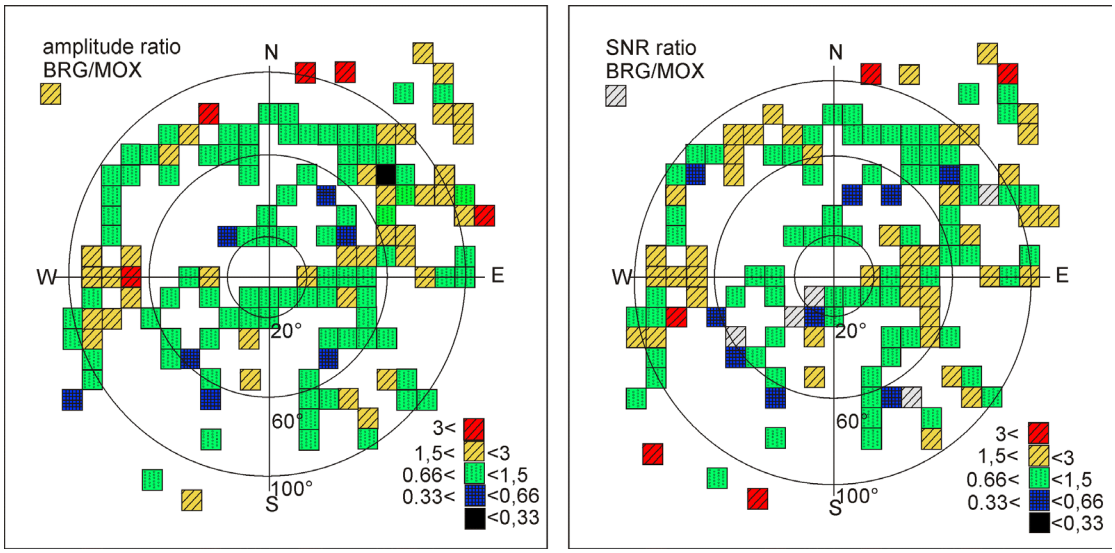

Fig. 4.38 Pattern of the relative short-period P-wave amplitudes at station BRG normalized to those of station MOX (170 km apart) in a distance-azimuth polar diagram (color version of Fig. 7 in Bormann et al., 1992).

However, differences in local signal conditions may become negligible in long-period recordings and thus play a lesser role in site selection for broadband networks and arrays. This is demonstrated with Fig. 4.39. Plotted are the low-pass (f_c = 0.1 Hz) filtered 3-component traces of an earthquake in Iran, recorded at the stations HAM and BSEG. According to Fig. 4.34 the short-period noise at BSEG was about 20 to 40 dB lower than at station HAM, yet, the long-period SNR in the Z-component of HAM is comparably good and even better in the horizontal component because the installation at BSEG reduces tilt noise. Thermal shielding and reduction of tilt noise have the highest priority in long-period and very broadband installations (see IS. 5.4).

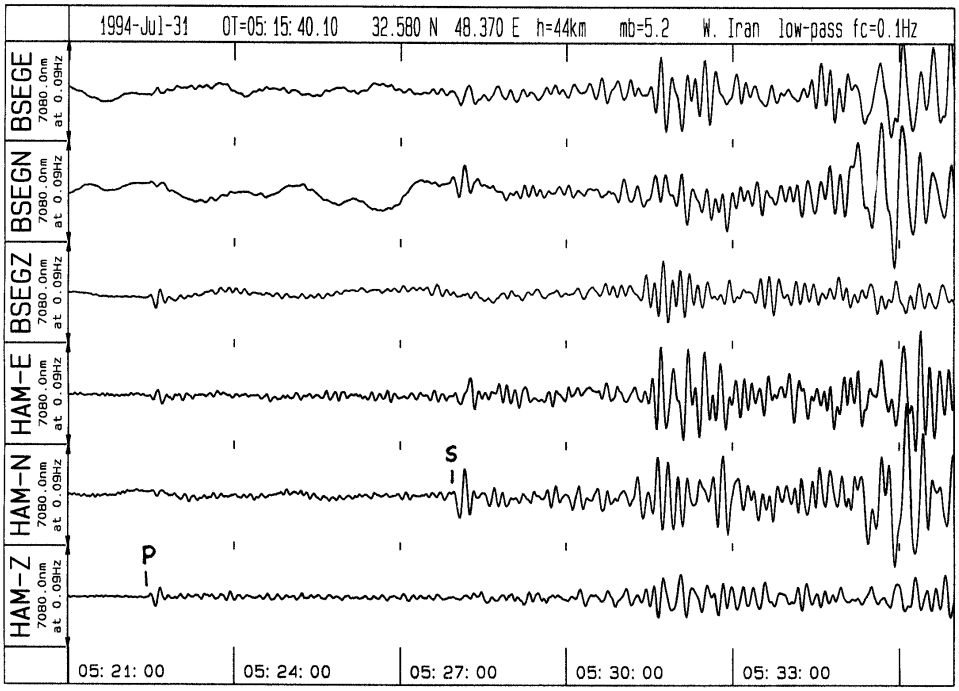

Fig. 4.39 Low-pass filtered (f_c = 0.1 Hz) long-period 3-component records at the seismic stations BSEG and HAM of the Iran earthquake. For the broadband noise spectra of these two station see Fig. 4.34. (Copy of Figure 20 from Bormann et al., 1997, J. Seismology; © Kluwer ?? Springer??).

4.6.5 Installations in subsurface mines, tunnels and boreholes

As shown in Fig. 4.29, Fig. 4.32 and Fig. 4.33, short-period seismic noise is strongly reduced with the depth in sensor installations in mines and boreholes. However, when installing seismometers at depth, one must also consider effects on the signal. Generally, amplitudes of seismic body waves recorded at the free surface are systematically increased by as much as a factor of two, depending on the angle of incidence and wavelength (see Exercise 3.4, Tab. 1). On the other hand, at a certain depth, destructive interference between incoming and surface-reflected waves may cause signal reduction. Therefore, because of the "free-surface effect", peculiarities of the local noise field and geological conditions, the SNR does not necessarily increase steadily with depth. Fig. 4.40 compares two case studies of short-period signal and noise measurements in two deep boreholes in the USA.

The ratio of the noise in the borehole and at the surface, S_B/S_{OF}, differs in the two boreholes. Its mean value drops in the Texas borehole to $1/10^{th}$ at about 1500 m depth and increases again to ½ of its surface value at 3000 m depth, while in the Oklahoma borehole it drops to about 1/3 at about 1000 m depth and then remains roughly constant thereafter. Accordingly, we have no SNR improvement (on average) in the Texas borehole down to about 1000 m depth, but then the SNR increases to a factor of about 15 at 3000 m depth. Contrary to this, the SNR increases by a factor of 3 in the Oklahoma borehole within the first 800 m, but then remains roughly constant (ranging between 1 and 5) up to 3000 m depth.

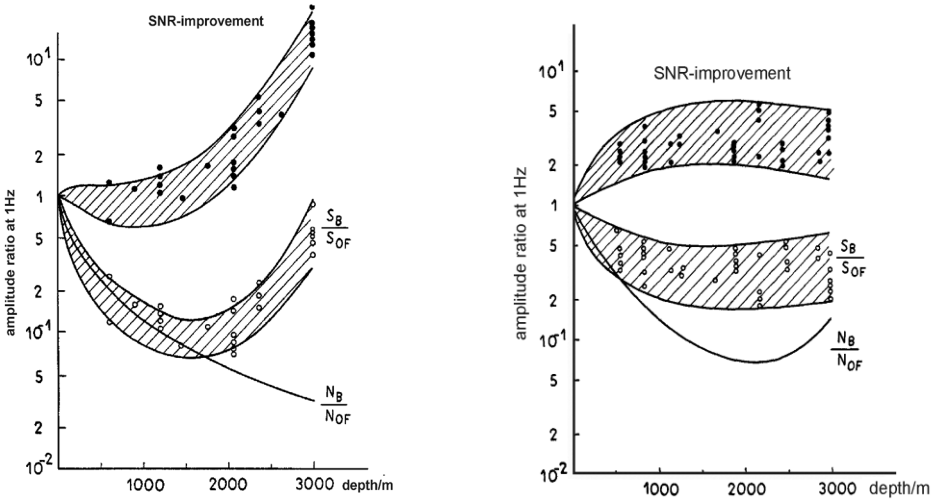

Fig. 4.40 Depth dependence of the signal-to-noise ratio (SNR). The top curve in both figures shows the improvement in SNR. The abbreviations are: SB/SOF: Ratio of signal in borehole and at the surface; NB/NOF: Ratio of noise in borehole and at the surface. SNR improvement in a borehole in Texas is shown left and in Oklahoma right. (Figure copied from Bormann, 1966; redrawn from Douze, 1964).

Thus there is no straight-forward and continuous SNR improvement with depth. It may depend also on local geological and installation conditions. Nevertheless, we can generally expect a significant SNR improvement within the first few hundred meters depth. This applies particularly to borehole installations of long-period and broadband sensors which benefit already a much shallower depth greatly from the very stable temperature conditions and strongly reduced tilt noise, also in hard rock tunnels. For more information about tunnel installations see section 7.4.3 in Chapter 7.

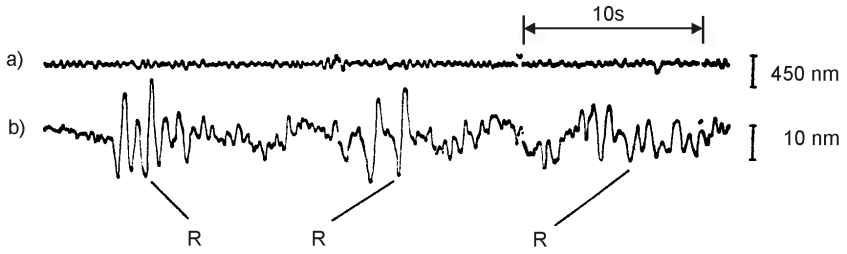

Fig. 4.41 Recording of a teleseismic event at D = 80° at a) the surface and b) at 3000 m depth in the Texas borehole (see Fig. 4.40 left). The SNR in record b) has improved by a factor of about 10. Note that signal arrivals in the borehole record are followed by surface reflections (R) about 3 s later (Figure copied from Bormann, 1966; redrawn from Douze, 1964).

In mines or boreholes a depth of 100 m is generally sufficient to achieve most of the practicable reduction by -20 to -30 dB of long-period noise with periods between 30 s and 1000 s) (see Fig. 7.59 in section 7.4.5 of Chapter 7). According to Murphy and Savino (1975) the effect of atmospheric pressure fluctuations on horizontal component noise is reduced by more than 90% at a depth of 150 m. In this context one should also be aware that in records of deep borehole installation the superposition of the first arriving waves with their respective surface reflection may cause irritating signal distortions although they can be filtered out by tuned signal processing (Fig. 4.41). However, for installations less than 200 m deep the travel-time difference between direct and reflected waves is (in consolidated rock) less than 0.1 s and

then usually negligible. Since the cost of drilling and installation increases greatly with depth, no deeper permanent seismic borehole installations have yet been made. In any event, the borehole should be drilled through the soil or weathered rock cover and penetrate well into the compacted underlying rock formations.

4.7 Improving the Signal-to-Noise Ratio by data processing

4.7.1 Frequency filtering

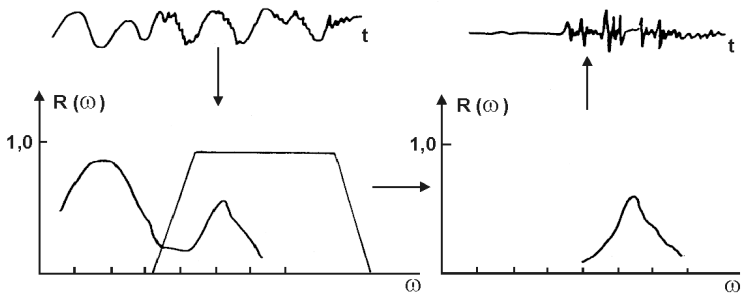

Fig. 4.42 Principle of FOURIER transform and bandpass filtering of a seismic record.

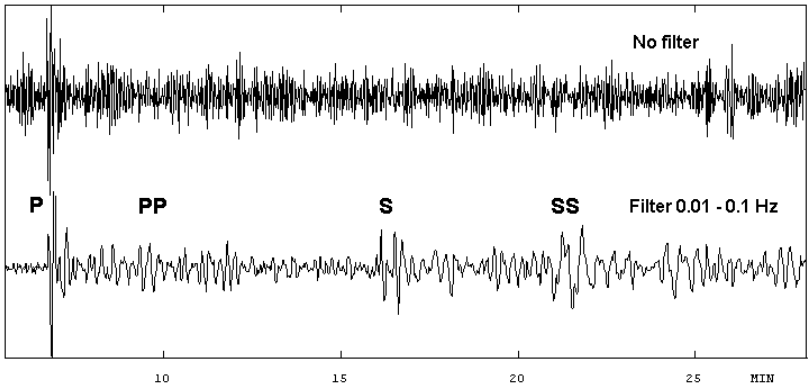

Fig. 4.43 Recording of a long-period trace at a broadband station. The LP trace has a flat velocity response from 360 s to 0.5 s. On the unfiltered trace (top), only the P-phase might be identified, while on the filtered trace (bottom), the signal-to-noise ratio is much improved and several later phases are clearly recognizable since the microseisms have been removed by filtering (courtesy of J. Havskov, 2001).

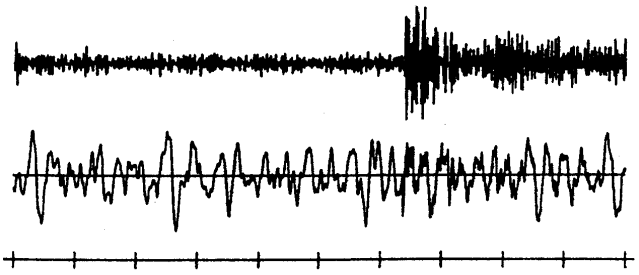

Fig. 4.44 Original (bottom) and frequency filtered record (top; f = 2.0 – 4.0 Hz) of an underground nuclear explosion at the Semipalatinsk test site, Eastern Kazakstan (D = 38°) at station 01A00 of the NORSAR array. Time marks in seconds (from Tronrud, 1983b).

When the frequency spectrum of the seismic signal of interest differs significantly from that of the superposed seismic noise, band-pass filtering can help to improve the signal-to-noise ratio (SNR). Fig. 4.42 illustrates the principle and Fig. 4.43 to Fig. 4.45 show examples.

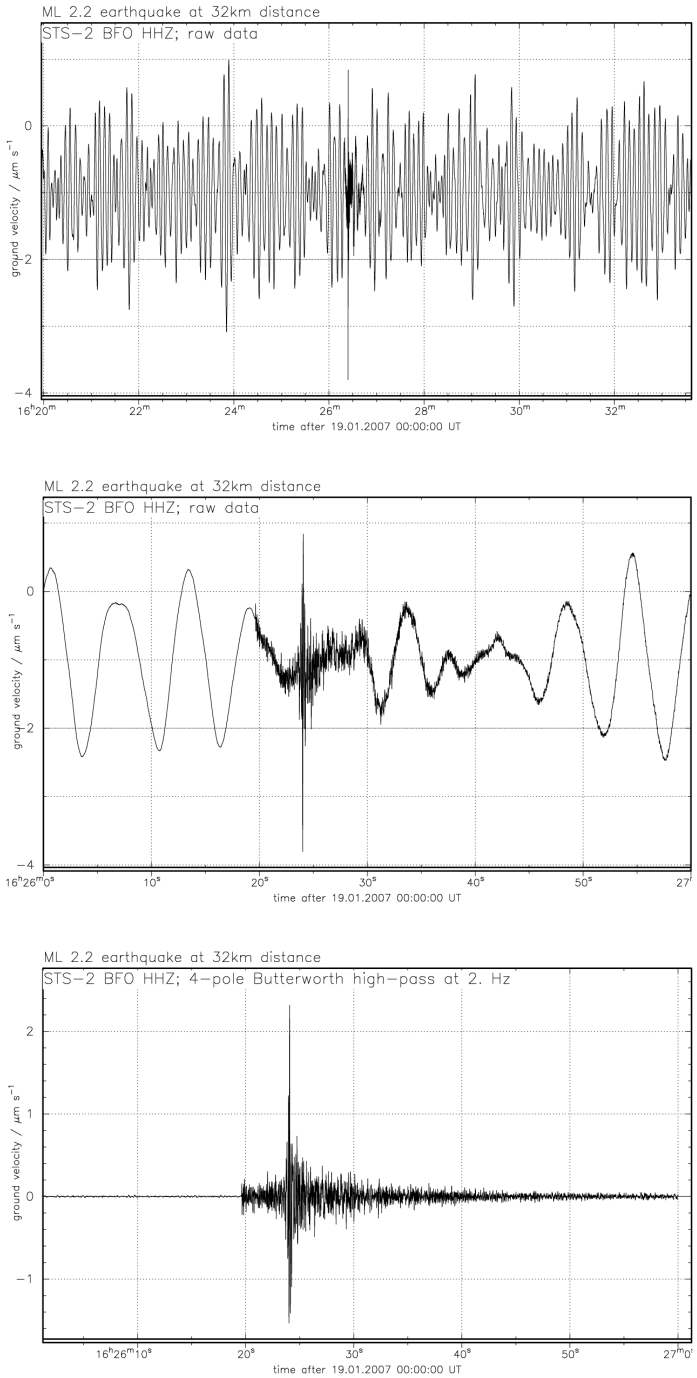

Fig. 4.45 Isolation of a local Ml = 2.2 earthquake that occurred 32 km away from the Black Forest Observatory (BF0), Germany, by frequeny filtering of the raw data of a velocity broadband STS-2 record. Top: 10 min record of raw data; Middle: stretched 1 min record of raw data; Bottom: elimination of the 6 s ocean microseisms by 2-Hz highpass filtering. (Plots by courtesy of Thomas Forbriger).

4.7.2 Velocity filtering and beamforming

Often the dominant signal frequencies may coincide with that of strong noise. Then frequency filtering does not improve the SNR. On the other hand, the horizontal propagation velocity of noise, being dominatingly surface waves of Rayleigh-wave type, is much lower than that of P waves and also lower than that of teleseismic S waves with a steep angle of incidence. This leads to frequency-wavenumber (f-k) filtering (see Chapter 9) as a way to improve SNR. To be able to determine the horizontal propagation direction and velocity of seismic signals by means of signal correlation, a group of seismic sensors must be deployed. If the aperture (diameter) of the sensor group is within the correlation radius of the signals it is called a seismic array (see Chapter 9); otherwise the group of sensors comprises a station network (see Chapter 8). Assuming that the noise within the array is random while the signal is coherent, even a simple direct summation of the n sensor outputs would already produce some modest SNR improvement. When the direction and velocity of travel of a signal through an array is known, one can compensate for the differences in arrival time at the individual sensors and then sum-up all the n record traces (beam forming). This increases the signal amplitude by a factor n while the random noise amplitudes increase in the beam trace only by $\sqrt{n}$, thus improving the SNR by $\sqrt{n}$. Fig. 4.46 compares the (normalized) individual records of 13 stations of the Gräfenberg array, Germany with the beam trace. A weak underground nuclear explosion at a distance of 143.6°, which is not recognizable in any of the single traces, is very evident in the beam trace.

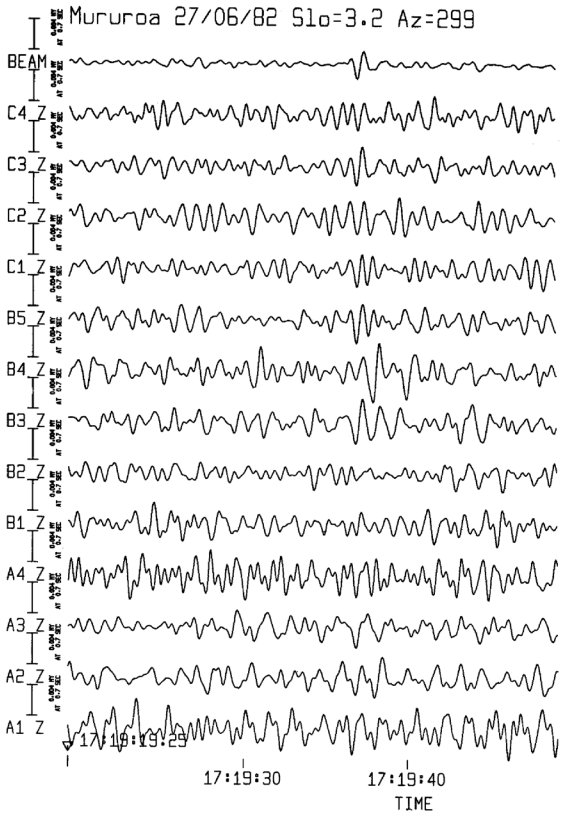

Fig. 4.46 Detection of a weak underground nuclear explosion in the 10 kt range at the Mururoa Atoll test site (D = 145°) by beam forming (top trace). No signal is recognizable in any of the 13 individual record traces from stations of the Gräfenberg array, Germany (below) (from Buttkus, 1986).

4.7.3 Noise prediction-error filtering

In near real time, it is possible to use a moving time-window to determine the characteristics of a given noise field by means of cross- and auto-correlation of array sensor outputs. This then allows the prediction of the expected random noise in a subsequent time interval. Subtracting the predicted noise time series from the actual record results in a much reduced noise level. Weak seismic signals, originally buried in the noise but not predicted by the noise "forecast" of the prediction-error filter (NPEF) may then stand out clearly. NPEFs have several advantages as compared to frequency filtering (compare with Fig. 4.47):

- No assumptions on the frequency spectrum of noise are required since actual noise properties are determined by the correlation of array sensor outputs;
- While frequency differences between signal and noise are lost in narrowband filtering, they are largely preserved in the case of the NPEF. This may aid signal identification and onset-time picking;
- Signal first-motion polarity is preserved in the NPEF whereas it is no longer certain after narrow-band or zero-phase band-pass filtering (see section 4.5).

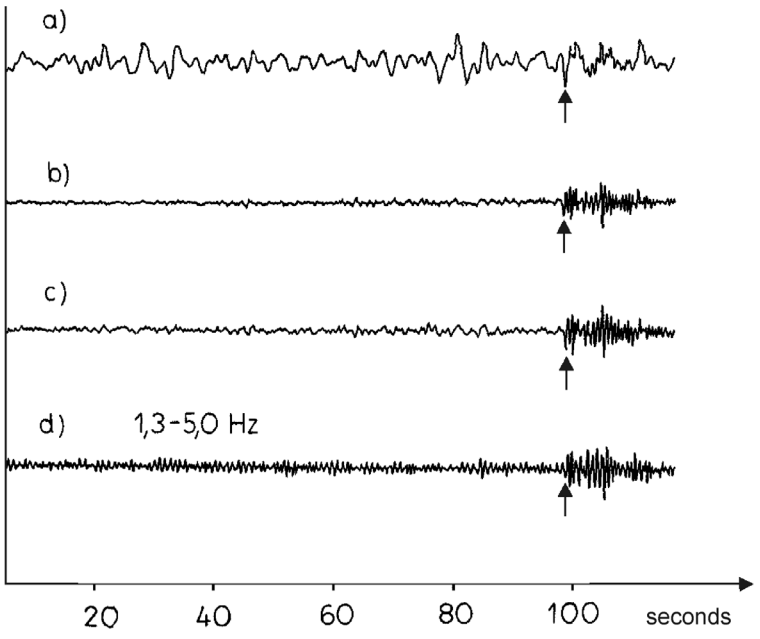

Fig. 4.47 Records of an underground nuclear explosion recorded at the Uinta Basin small aperture seismic array a) in the beam trace (sum of 10 seismometers), b) and c) after noise prediction error filtering with and without cross correlation (see 4.4.2) and d) after frequency band-pass filtering (1.3 – 5 Hz) (compiled by Bormann, 1966, from data published by Claerbout, 1964).

4.7.4 Noise polarization filtering

3-component recordings allow one to reconstruct the ground particle motion and to determine its polarization. Shimshoni and Smith (1964) investigated the cross product

$$M_j = \sum_{i=-n}^{n} H_{i+j} \cdot V_{i+j} \tag{4.20}$$

in the time interval $j - n$ to $j + n$ with H and V as the horizontal and vertical component recordings, respectively. M is a measure of the total signal strength as well as of the degree of linear wave polarization. Eq. (4.20) vanishes for Rayleigh, Love and SH waves. On the other hand, for linearly polarized P and SV waves, H and V are exactly in phase and the correlation function becomes +1 for P and –1 for SV waves. The longer the integration time, the better the suppression of randomly polarized noise with a high Rayleigh-wave component. The optimal window length for good noise suppression, while still allowing good onset time picking, must be found by trial and error. Fig. 4.48 gives an example. One great advantage of polarization filtering is that it is independent of differences in the frequency and velocity spectrum of signal and noise and thus can be applied in concert with other procedures for SNR improvement.

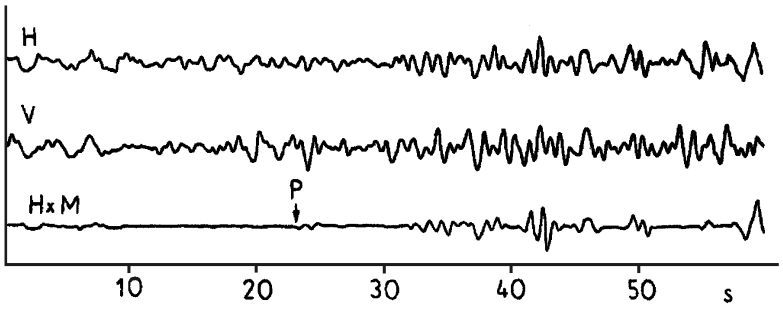

Fig. 4.48 Example of SNR improvement by polarization filtering according to Eq. (4.20) (bottom trace). H – horizontal component record, V – vertical component record (modified from Shimshoni and Smith, 1964).

4.8 Global detection thresholds

4.8.1 Detection thresholds for surface waves and long-period body waves

Webb (2002) discusses on the basis of data and diagram compilations by several authors the detection thresholds on land-based and ocean bottom station sites for seismic events in terms of their moment magnitudes. According to Fig. 4.49a the global noise levels are sufficiently low at most land-based sites to allow the detection of long-period seismic arrivals from large distant earthquakes. Many of the Earth normal modes can be detected at the quieter sites from the largest events as well. Signal- to-noise ratios are estimated by comparing the root mean square (rms) noise levels with model signal amplitudes in 1/3 octave bands. Signal levels are estimated for teleseismic distances of 30°. The solid lines relate to surface wave and body wave amplitudes. The broken lines, extending the surface wave curves, represent normal mode amplitudes. Surface wave spectra, however, vary greatly with source mechanism and depth. Accordingly, surface waves from shallow events are barely detectable near 0.04 Hz at most sites from events exceeding about Mw = 4.5, but the detection of lower-frequency surface waves and normal modes requires larger events. Body waves can be detected at most sites at frequencies below the microseism peak from events with Mw > 4.5. Smaller events can be detected at smaller distances.

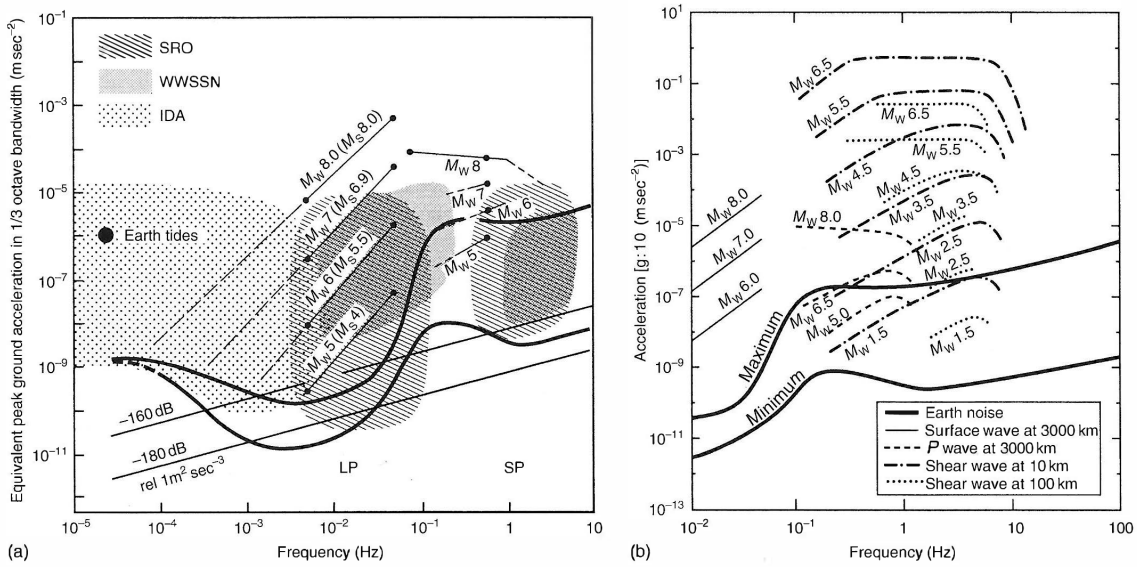

Fig. 4.49 (a) Amplitudes of seismic arrivals and vertical component noise levels in l/3 octave bands against the approximate new global low and high noise models (NLNM and NHNM; thick black lines) according to Peterson (1993), illustrate typical detection thresholds for surface waves and body waves for arrivals from teleseismic distances. The dynamic range of several global land-based networks is shown by differently shaded areas (from Agnew et al., 1986). (b) More short-period noise levels and amplitudes (in terms of moment magnitude levels) of seismic phases at regional and local distances. (Reproduced with permission from Heaton et al., 1989). Copied from Figure 3 in Webb (2002); © Academic Press, Amsterdam.

Spectra from stations on the sea floor suggests similar detection thresholds for surface waves near 25 s period and for long-period body waves as on land (Webb, 1998). The detection thresholds for pressure measurements for body waves and surface waves in the band from 0.05 to 0.1 Hz are also similar to vertical acceleration detection thresholds. However, horizontal component seismic data from the sea floor are invariably much noisier than vertical component data below 0.03 Hz because of tilt noise. This limits the detection of Love waves and SH body waves to periods shorter than about 25 sec. However, as discussed earlier, shallow burial of the sensor packages could make horizontal component noise levels more comparable with vertical component noise levels and improve detection thresholds greatly.

Vertical component noise levels below 0.03 Hz on the Pacific sea floor are larger than at most continental sites because of deformation under infragravity waves. This makes detection of long-period (>100 sec) surface waves and normal modes difficult at typical sea-floor stations. In the North Atlantic lower amplitudes of infragravity wave provide better SNR for surface-wave and normal mode observations, at least during the quiet summer months.

4.8.2 Detection thresholds for short-period body waves

Approximate detection thresholds for teleseismic (30°) and local short-period P waves for land- and sea-floor sites can be estimated from Fig. 4.49 above and Fig. 4.50 below.

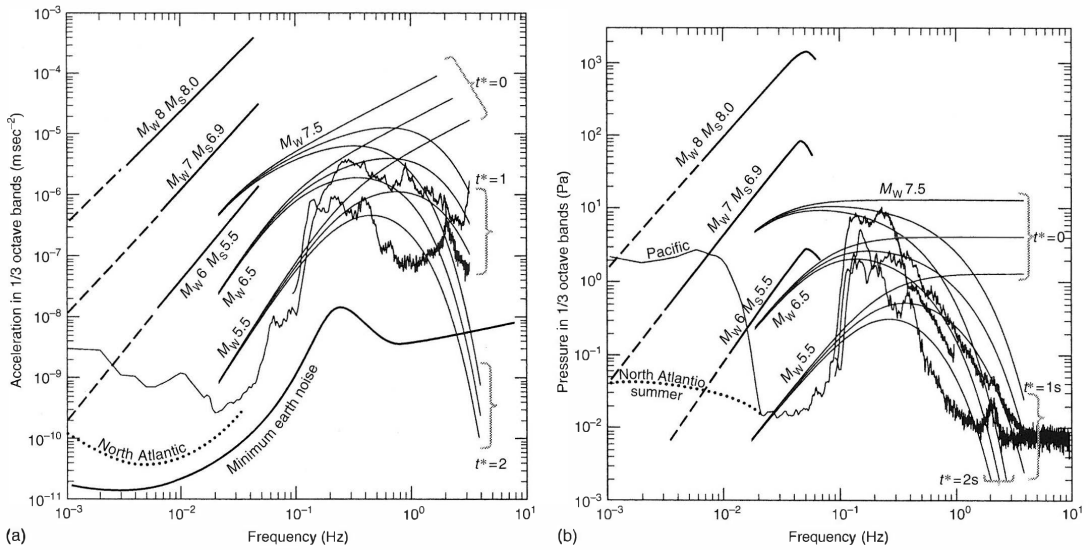

Fig. 4.50 Same as Figure 4.49 for sea-floor sites for (a) vertical acceleration, and (b) pressure with noise levels from an atypically quiet (calm wind) interval (left) and from a more typical noisy (windy) interval (right). Signal amplitudes are modeled for three different values of attenuation (t*). High noise levels near 1 Hz make it difficult to detect short-period teleseismic body wave phases. (Copied from Figure 4 in Webb, 2002; © Academic Press, Amsterdam)

The detection thresholds depend on distance and travel-path as well as wave-type related attenuation. The rapid decrease in microseism noise at frequencies larger than the frequency of the microseism peak means that small changes in the frequency content of seismic phases may be associated with large differences in detection thresholds. S-waves are more attenuated than P-waves (see section 2.5.4.2 and Fig. 2.79 in Chapter 2 as well as the compressional and shear Q tables and formula in DS 2.1). The dominating frequency content of shear waves may therefore be too low in frequency at teleseismic distances to be seen at all above the large amplitudes of the microseism peak. P waves, however, have at teleseismic distances still enough energy around 1 Hz to be seen on records at land sites but not at generally more noisy sea-floor sites. According to Fig. 4.49 the detection thresholds at most land sites for P waves from distant events (>30°) will be roughly magnitude Mw 4.0, with slightly lower values for the quieter sites and much higher detection thresholds for the noisier island sites. According to Webb (2002) this is in rough agreement with more careful estimates of detection thresholds for groups of stations. Recent estimates for global event detection thresholds using seismic arrays range from about Mw 3.5 for heavily instrumented areas such as Europe to greater than Mw 4.5 for remote regions of the world's oceans (e.g., Kvaerna and Ringdal, 1999). Fig. 4.49 suggests that all stations will detect S wave arrivals from events as small as about Mw 2.5 at close range (100km).

Efforts to detect small underground nuclear explosions have focused on detecting high-frequency Pn and Sn arrivals at regional distances over continental platforms. Pn is then detectable at frequencies up to 50 Hz at 500 km and at distances up to 1500 km at 10 Hz from magnitude Ml 3.0 events. Also high-frequency oceanic Pn and Sn waves can still be detected over great distances from moderate oceanic events (lower detection threshold mb ≈ 4.6) because at their higher frequency the ocean microseism noise is low (Butler et al., 1987). However, at most sea-floor sites the high noise levels near 1 Hz and high attenuation in the oceanic upper mantle allow to detect teleseismic P waves with periods around 1 s only with poor SNR

from events with Mw > 7 (Blackman et al., 1995). However, the lower noise levels within sea-floor boreholes may lower the detection thresholds for short-period teleseismic body waves from the Mw = 7.5, expected for noisy sea-floor sites with a saturated microseism spectrum, to about Mw 6.5 and detection limits for quiet sea-floor noise conditions should be below Mw 5.5. Orcutt and Jordan (1986), e.g., reported on detection thresholds from a sensor in a borehole in the western Pacific, which is at a site where light winds are expected more than 73% of the time, suggesting low noise levels near 1 Hz. The lower detection limits increased from about mb = 5.2 at a distance of 40° to about mb = 5.6 at 80°. This is consistent with the low-noise model of Fig. Fig. 4.50a, combined with a 10 dB SNR improvement due to the borehole installation, particularly if the observations are associated with deep earthquakes from the subduction zones of the western Pacific, with signals propagating along low-attenuation paths.

Wilcock et al. (1999) arrived at similar conclusions with respect to lower detection thresholds in an ocean environment. They investigated wind statistics over the world's ocean-floor ridges to look for regions where long intervals of calm winds are more common. In these quiet regions noise levels will often be 20 dB lower than at typical sites with wind-noise saturation, and thus their associated detection thresholds several magnitude units smaller. Figure 4.50a shows noise in l/3 octave bands from a site on the sea floor during a typical noisy period and Fig. 4.50 during one of the rare low-wind days from the MELT experiment. Teleseismic detection thresholds at the sea floor depend on attenuation below a site which is represented by the value of t* shown on the model curves for P-wave amplitude for earthquakes of magnitudes 5.5, 6.5, and 7.5. The microseism noise spectrum falls quickly with increasing frequency. Therefore detection thresholds for short-period teleseismic P waves are lower. The model curves for t* = 0 suggest that only the largest earthquakes (Mw > 7 .5) will be detected at typical noisy sea-floor sites near ridge crests (where attenuation is high). The detection threshold at sites on older oceanic crust, and for arrivals from deep earthquakes for which attenuation is less (t* = 1) are lower (Mw ≈ 6). Finally, at sea-floor sites that see long intervals with calm conditions overhead (see Fig. 4.50b) the detection threshold may fall as low as Mw = 5.5. The detection thresholds at local and regional distances for sites on the sea floor are even much lower because of the much higher frequency content of the wave arrivals as compared to that of the microseism peak. Local events with Mw between -1.5 and 20 have been detected during microearthquake studies on ridge crests.

Acknowledgments

The authors thank E. Bergman, J. Havskov and E. Hjortenberg for carefully reading the draft for the first edition and for their valuable suggestions which helped to improve the text and a few figures. Still these parts make for most of the revised and amended 2nd edition. The new section 4.2 and parts of sections 4.3 and 4.4 are based on lecture notes by E. Wielandt, who also contributed the new Figs. 4.4. 4.5 and 4.6. Thanks go also to two reviewers of the upgraded version of this Chapter for their valuable comments. Th. Forbriger made lecture notes on seismic noise available as well, provided Fig. 4.45 and recommended additional references. J. R. R. Ritter checked the correctness of section 4.3.3.6 on urban noise. Several topically well-fitting figures were reproduced, with proper acknowledgment and permission by the authors, from other related NMSOP-2 contributions, e.g., Fig. 4.11 from L. Küperkoch, Fig. 4.18 from S. Wendt, Fig. 4.20 from Th. Diehl, and Fig. 4.24 and Fig. 4.25 from M. Shinohara.

Recommended overview readings

Buttkus (2000)
Galperin et al. (1978)
Havskov and Alguacil (2002)
Kumar and Ahmed (2011)
Richardson et al. (1995)
Scherbaum (2007)
Tabulevich (1992)
Webb (1998, 2002)

References

Agnew, D. C., Berger, J., Farrell, W. E., Gilbert, J. F., Masters, G., and Miller, D. (1986). Project IDA: a decade in review. *EOS Trans. Am. Geophys. Union*, **67**(10), 203-212.

Aki, K., and Richards, P. G. (1980). *Quantitative seismology – theory and methods*, Volume II, Freeman and Company, ISBN 0-7167-1059-5(v. 2), 609-625.

Aki, K., and Richards, P. G. (2002). *Quantitative seismology*. 2nd ed., ISBN 0-935702-96-2, University Science Books, Sausalito, CA.,xvii + 700 pp.

Aki, K., and Richards, P. G. (2009). *Quantitative seismology*. 2nd ed., corr. Print., Sausalito, Calif., Univ. Science Books, 2009, XVIII + 700 pp., ISBN 978-1-891389-63-4 (see http://www.ldeo.columbia.edu/~richards/Aki_Richards.html).

Araki, E., Shinohara, M., Sacks, S., Linde, A., Kanazawa, T., Shiobara, H., Mikada, H., and K. Suyehiro (2004). Improvement of seismic observation in the ocean by use of seafloor boreholes. *Bull. Seism. Soc. Am.*, 94, 678-690.

Aster, R. C. and Shearer, P. M. (1991). High frequency seismograms recorded in the San Jacinto fault zone, Southern California, part 2. Attenuation and site effects. *Bull. Seismol. Soc. Am.*, **81**(4), 1081-1100.

Bard, P.-Y. (1999). Microtremor measurements: A tool for site effect estimation? In: Irikura, K., Kudo, K., Okada, H., and Sasatani, T. (Eds.) (1999). The effects of surface geology on seismic motion. Proc. *2nd International Symposium in Yokohama, Japan, 1-3 Dec. 1998, A. A. Balkema*, Rotterdam, ISBN 90 5809 030 2, 1251-1279.

Beauduin, R. and J.-P. Montagner (1996). Time evolution of broad- band seismic noise during the French pilot experiment OFM/ SISOBS. *Geophys. Res. Lett.*, **23**(21), 2995-2998.

Beauduin, R., Lognonné, P., Montagner, J. P., Cacho, S., Karczewski, J. F., and Morand, M. (1996). The effects of the atmospheric pressure changes on seismic signals or How to improve the quality of a station. *Bull. Seism. Soc. Am.*, **86**, 6, 1760-1769.

Berger, J., Davis, P., Ekström, G. (2004). Ambient Earth noise: A survey of the Global Seismographic Network. *J. Geophys. Res.*, **109**, B11307, doi: 10.1029/2004JB003408.

Blackman, E. K., Orcutt, J. A., and Forsyth, D. W. (1995). Recording teleseismic earthquakes using ocean-bottom seismographs at mid-ocean ridges. *Bull. Seism. Soc. Am.*, **85**, 6, 1648-1664.

Bormann, P. (1966). *Recording and interpretation of seismic events (principles, present state and tendencies of development)* (in German). Publ. Inst. Geodyn., Jena, Akademie Verlag, Berlin, 158 pp.

Bormann, P. (1973). Standardization and optimization of frequency-characteristics at Moxa station (GDR). Proceed. XII Assembly of ESC, Bukarest, *Technical and Economic Studies*, D-Series, **No. 10**, 133-145.

Bormann, P., Wylegally, K., and Klinge, K. (1997). Analysis of broadband seismic noise at the German Regional Seismic Network and search for improved alternative station sites. *J. Seism.*, **1**, 357-381.

Bormann, P. (1998). Conversion and comparability of data presentations on seismic background noise. *J. Seism*., **2**, 37-45.

Braddner, H., and Dodds, I. G. (1964). Comparative seismic noise on the ocean bottom and on land. *J.Geophys. Res*., **69**, 20, 4339-4348.

Bradley, C. R., and Stephen, R. A. (1996). Modeling of seafloor wave propagation and acoustic scattering in 3-D heterogeneous media. *J. Acoust. Soc. Am*., **100**(1), 225-236.

Bradley, C.R., Stephen, R. A., Dorman, L. M., and Orcutt, J. A. (1997). Very low frequency (0.2-10 Hz) seismoacoustic noise below the seafloor. *J. Geophys. Res*., **102**(B6), 11703-11718.

Broding, R. A., Bentley-Llewellyn, N. J., and Hearn, D. P. (1964). A study of three dimensional seismic detection system. *Geophysics*, **29**, 2, 221-249.

Brune, J. N., and Oliver, J. (1959). The seismic noise of the Earth´s surface. *Bull. Seism. Soc. Am.*, **49**, 349-353.

Bungum, H., Mykkeltveit, S., and Kvaerna, T. (1985). Seismic noise in Fennoscandia, with emphasis on high frequencies. *Bull. Seismal. Soc. Am.*, **75**, 1489-1513.

Butler, R., McCreery, C. S., Frazer, L. N., and Walker, D. A. (1987). High frequency seismic attenuation of oceanic P and S waves in the western Pacific. *J. Geophys. Res.*, **92**(B2), 1383-1396.

Buttkus, B. (Ed.) (1986). Ten years of the Gräfenberg array: defining the frontiers of broadband seismology. *Geologisches Jahrbuch* **E-35**, Hannover, 135 pp.

Buttkus, B. (2000). Spectral analysis and filter theory in applied geophysics. Springer Verlag, xv+667 pp., ISBN 3-540-62674-3.

Carter, J.A., N. Barstow, P.W. Pomeroy, E.P. Chael, and P.J. Leahy (1991). High frequency seismic noise as a function of depth. *Bull. Seismal. Soc. Am*., **81**(4), 1101-11 14.

Cessaro, R. K. (1994). Sources of primary and secondary microseisms. *Bull. Seism. Soc. Am*., **84,** 1, 142-148.

Diehl, T., Kissling, E., and Bormann, P. (2012). Tutorial for consistent phase picking at local to regional distances. In: Bormann, P. (Ed.). *New Manual of Seismological Observatory Practice (NMSOP-2)*, *IASPEI,* GFZ German Research Centre for Geosciences, Potsdam, 21 pp; doi: 10.2312/GFZ.NMSOP-2_IS_11.4; http://nmsop.gfz-potsdam.de,

Douze, E. J. (1964). Signal and noise in deep wells. *Geophysics*, **29**, 5, 721-732.

Duda, S. J., and Kaiser, D. (1989). Spectral magnitudes, magnitude spectra, and earthquake quantification: the stability issue of the corner period and of the maximum magnitude for a given earthquake. *Tectonophysics*, **166**, 205-219.

Engdahl, E. R., and Gunst, R. H. (1966). Use of a high speed computer for the preliminary determination of earthquake hypocenters. *Bull. Seism. Soc. Am.,* **56**, 325-336.

Evans, John R.; Followill, F.; Hutt, Charles R.; Kromer, R. P.; Nigbor, R. L.; Ringler, A. T.; Steim, J. M.; Wielandt, E. (2010). Method for calculating self-noise spectra and operating

ranges for seismographic inertial sensors and recorders. Seismological Research Letters, 81: 640 - 646

Fix, J. E. (1972). Ambient Earth motion in the period range from 0.1 to 2560 sec. *Bull. Seism. Soc. Am.*, **62**, 1753-1760.

Friedrich, A., Klinge, K., and Krüger, F. (1998). Ocean-generated microseismic noise located with the Gräfenberg array. *J. Seism.*, **2**, 47-64.

Fyen, J. (1990). Diurnal and seasonal variations in the microseismic noise observed at the NORESS array. *Phys. Earth Planet. Inter.*, **63**, 252-268.

Galperin, E.I., I.L. Nersesov, and R.M. Galperina (1978). *Borehole Seismology and the Study of the Seismic Regime of Large Industrial Centers*. D. Reidel, Dordrecht.

Groos, J. C., and Ritter, J. R. R. (2009). Time domain classification and quantification of seismic noise in an urban environment. *Geophys. J. Int.*, 179, 1213-1231; doi: 10.1111/j.1365-246X.2009.04343.x.

Hasselmann, K.A. (1963). A statistical analysis of the generation of microseisms. *Rev. Geophys.*, **1**, 177-209.

Haubrich, R. A., and McCamy, K. (1969). Microseisms coastal and pelagic sources. *Rev. Geophys. Space Phys.*, **7**, 539-571.

Haubrich, R. A., Munk, W. H., and Snodgrass, F. E. (1963). Comparative spectra of microseisms and swell. *Bull. Seism. Soc. Am.*, **53**, 27-37.

Havskov, J., and Alguacil, G. (2006). Instrumentation in earthquake seismology. *Springer*, Berlin, 2nd edition, 358 pp. plus CD.

Heaton, T.H., Anderson, D. L., Arabasz, W. J., et al. (1989). National Seismic System Science Plan. *USGC Survey Circular* **1031**, 1-42.

Holcomb, L. G. (1998). Spectral stucture in the Earth's microseismic background between 20 and 40 seconds. *Bull. Seismol. Soc. Am.*, **88**(3), 744-757.

IASPEI (2005). Summary of Magnitude Working Group recommendations on standard procedures for determining earthquake magnitudes from digital data.
http://www.iaspei.org/commissions/CSOI/summary_of_WG_recommendations_2005.pdf

IASPEI (2013). Summary of Magnitude Working Group recommendations on standard procedures for determining earthquake magnitudes from digital data.
http://www.iaspei.org/commissions/CSOI/Summary_WG_recommendations_20130327.pdf

Küperkoch, L., Meier, Th., and Diehl, T. (2012). Chapter 16: Automated event and phase detection. In: Bormann, P. (Ed.). *New Manual of Seismological Observatory Practice (NMSOP-2)*, *IASPEI,* GFZ German Research Centre for Geosciences, Potsdam, 52 pp; doi: 10.2312/GFZ.NMSOP-2_ch16; http://nmsop.gfz-potsdam.de,

Kulhanek, O. (2002). The structure and interpretation of seismograms. In: Lee, W. H. K., Kanamori, H., Jennings, P. C., and Kisslinger, C. (Eds.) (2002). International Handbook of Earthquake and Engineering Seismology, Part A. *Academic Press, Amsterdam*, 333-348.

Kumar, D., and Ahmed, I. (2011). Seismic noise. In: Harsh Gupta (ed.). *Encyclopedia of Solid Earth Geophysics,* Springer, Vol. 2, 1157-1161; doi: 10.1007/978-90-481-8702-7.

Kvaerna, T., and Ringdal, F. (1999). Seismic threshold monitoring for continuous assessment of global detection capability. *Bull. Seismal. Soc. Am.*, **89**(4), 949-959.

Lay, T., and Wallace, T. C. (1995). Modern global seismology. ISBN 0-12-732870-X, *Academic Press*, 521 pp.

Longuet-Higgins, M. S. (1950). A theory for the generation of microseisms. *Philos. Trans. R. Soc. Lond.*, **A 243**, 1-35.

McCreery, C.S., F.K. Duennebier, and G.H. Sutton (1993). Correlation of deep ocean noise (0.4-20 Hz) with wind, and the Holu spectrum - a worldwide constant. *J. Acoust. Soc. Am.*, **93**(5), 2639-2648.

Melton, B. S. (1978). The sensitivity and dynamic range of inertial seismographs. *Rev. Geophys. Space Phys.*, **14**, 393-116.

Montagner, J. P., Karczewski, J. F., Romanowicz, B., Bouaricha, S., Lognonné, P., Roult, G., Stutzmann, E., Thirot, J. L., Brion, J., Dole, B., Fouassier, D., Koenig, J.C., Savary, J., Loury, L., Dupond, J., Echardour, A., and Floc'h, H. (1994). The French pilot experiment OFM-SISMOBS: first scientific results on noise level and event detection. *Physics Earth Planet. Inter.*, 84, 321-336.

Murphy, A.J. and J.R. Savino (1975). A comprehensive study of long period (20-200 s) Earth noise at the high gain worldwide seismo- graph stations. *Bull. Seismol. Soc. Am.*, **65**, 1827-1862.

Nakamura, Y. (1989). A method for dynamic characteristics estimation of subsurface using microtremor on the ground surface. *Q. Rep. Railway Tech. Res. Inst*., **30**, 25-33.

Orcutt, J. A., and Jordan, T. H. (1986). Data from the Ngendei experiment in the southwest Pacific. In: *"The Vela Program,"* (Ed, A. Kerr), pp. 758-770. Def. Adv. Res. Proj. Agency, Washington, DC.

Parolai S., Bormann, P., and Milkereit, C. (2001b). Assessment of the natural frequency of the sedimentary cover in the Cologne area (Germany) using noise measurements. *J. Earthq. Engrg.*, **5,** 541-564.

Parolai S., Bormann, P., Milkereit, C. (2002). New relationships between V_s, thickness of sediments, and resonance frequency calculated by the H/V ratio of seismic noise for the Cologne area (Germany). *Bull. Seism. Soc. Am.*, **92**, 2521-2527.

Peterson, J. (1993). Observations and modeling of seismic background noise. *U.S. Geol. Survey Open-File Report* **93-322**, 95 pp.

Richardson, W. J, Greene, C. R., Malme, C. I., and Thomson, D. H. (1995). *Marine mammals and noise*. Academic Press, San Diego.

Romanowicz, B., D. Stakes, J.-P. Montagner, et al. (1998). MOISE: a pilot experiment toward long term seafloor geophysical obser- vatories. *Earth Planets Space*, **50**, 927-937.

Savino, J., McCamy, K., and Hade, G. (1972). Structures in Earth noise beyond twenty seconds - a window for earthquakes. *Bull. Seismal. Soc. Am.*, **62**(1), 141-176.

Scherbaum, F. (2007). *Of poles and zeros; Fundamentals of Digital Seismometry*. 3rd revised edition, Springer Verlag, Berlin und Heidelberg.

Schreiner, A. E., and Dorman, L. M. (1990). Coherence lengths of seafloor noise: effect of ocean bottom structure. *J. Acoust. Soc. Am.*, **88**(3), 1503-1514.

Sleeman, R., van Wettum, A., and Trampert, J. (2006). Three-channel correlation analysis: A new technique to measure instrumental noise of digitizers and seismoc sensors. *Bull. Seism. Soc. Am.*, **96**(1), 258–271.

Shimshoni, M., and Smith, S. W. (1964). Seismic signal enhancement with three-component detectors. *Geophysics*, **29**, 5, 664-671.

Stephen, R. A., Collins, J. A., and Peal, K. R. (1999). Seafloor seismic stations perform well in study. *Eos, Trans. Am. Geophys. Un.*, **80**, 592.

Tabulevich, V. (1992). Microseismic and infrasound waves. *Springer-Verlag Berlin*, 150 pp.

Tronrud, L. B. (Ed.)(1983). Semiannual Technical Summary 1 October 1982 – 31 March 1983. *NORSAR Scientific Report* No. 1-82/83, 72 pp.

Vernon, F. L. et al. (1998). Evaluation of teleseismic waveforms and detection thresholds from the OSN pilot experiment. *EOS Trans. Am. Geophys. Union*, **79**(45), 650.

Webb S. C. (1998). Broadband seismology and noise under the ocean. *Rev. Geophys.* **36,** 105–142.

Webb, S. C. (2002). Seismic noise on land and on the sea floor. In: Lee, W. H. K., Kanamori, H., Jennings, P. C., and Kisslinger, C. (Eds.) (2002). International Handbook of Earthquake and Engineering Seismology, Part A, *Academic Press, Amsterdam*, 305-318.

Webb, S.C., and Schultz, A. D. (1992). Very low frequency ambient noise at the seafloor under the Beaufort sea icecap. *J. Acoust. Soc. Am*., **91**(3), 1429-1439.

Webb, S. C., and Crawford, W. C. (1999). Long period seafloor seis- mology and deformation under ocean waves. *Bull. Seismal. Soc. Am*., **89**(6), 1535-1542.

Wiechert, E. (1904). Verhandlungen der zweiten internationalen Seismologischen Konferenz. *Beitr. Geophys*., Ergänzungsband II, 41-43.

Wilcock, W. S. D., Webb, S. C., and Bjarnason, I. Th. (1999). The effect of local wind on seismic noise near 1 Hz at the MELT site and on Iceland. *Bull. Seismal. Soc. Am*., **89**(6), 1543-1557.

Willmore, P. L. (Ed.) (1979). Manual of Seismological Observatory Practice. *World Data Center A for Solid Earth Geophysics*, Report **SE-20**, September 1979, Boulder, Colorado, 165 pp.

Withers, M. M., Aster, R. C., Young, Ch. J., and Chael, E. P. (1996). High-frequency analysis of seismic background noise as a function of wind speed and shallow depth. *Bull. Seism. Soc. Am.*, **86**, 5, 1507-1515.

Yanovskaya, T. G. (2012). Surface-wave tomography for upper mantle studies: methods and results. Keynote lecture at the *33rd General Assembly of the European Seismological Commission*, Moscow, 19-24 Aug. 2012.

Young, Ch. J., Chael, E. P., Withers, M. W., and Aster, R. C. (1996). A comparison of the high- frequency (>1Hz) surface and subsurface noise environment at three sites in the United States. *Bull. Seism. Soc. Am*., **86**, 5, 1516-1528.

Zürn, W. (1974). Detectability of small harmonic signals in digitized records. *J. Geophys. Res., Solid Earth and Planets,* **79**(29), 4433–4438.

Zürn, W., and Widmer, R. (1995). On noise reduction in vertical seismic records below 2 mHz using barometric pressure. *Geophys. Res. Lett*, **22**(24), 3537-3540.

Zürn, W., and Wielandt, E. (2007), On the minimum of vertical seismic noise near 3 mHz. *Geophys. J. Int.*, **168**, 647-658.